Statistical Metrology and Process Control of Quantum Devices

by

Michael P. Walsh

B.S. Physics and EECS, Massachusetts Institute of Technology (2013)
S.M. EECS, Massachusetts Institute of Technology (2015)

Submitted to the Department of Electrical Engineering and Computer Science
in partial fulfillment of the requirements for the degree of

Doctor of Philosophy

at the

MASSACHUSETTS INSTITUTE OF TECHNOLOGY

May 2020

Author .....
Department of Electrical Engineering and Computer Science
May 15, 2020

Certified by .....
Dirk R. Englund
Associate Professor of Electrical Engineering and Computer Science
Thesis Supervisor

Accepted by .....
Leslie A. Kolodziejski
Professor of Electrical Engineering and Computer Science
Chair, Department Committee on Graduate Students

Statistical Metrology and Process Control of Quantum Devices

by

Michael P. Walsh

Submitted to the Department of Electrical Engineering and Computer Science
on May 15, 2020, in partial fulfillment of the
requirements for the degree of
Doctor of Philosophy

Abstract

Quantum emitters, such as color centers (e.g., nitrogen-vacancy color centers in diamond), have a wide range of applications in quantum information processing, bioimaging, and quantum sensing. Such quantum emitters are typically addressed optically and store their quantum state as an electron spin that can subsequently be read out optically. For this process to work effectively, an efficient light-matter interaction must be achieved, which is difficult given the small interaction cross section of an atomic memory with the optical field.

In this thesis, I address three problems that relate to the engineering of a quantum device. The first problem centers on the fact that most quantum emitters are randomly positioned throughout their host lattice making it difficult to lithographically pattern structures intended to increase the light-matter interaction. While there is a non-zero chance that a small number of randomly aligned structures will coincide with randomly positioned emitters, when efforts to scale such a system are made the yield drops exponentially. The second problem has to do with scaling. As systems scale up to larger sets of interacting qubits, it becomes increasingly necessary to produce quantum emitters with narrow optical transitions and long spin coherence times. The third problem is related to the development of tools to manage experiments and data in a more robust, team-centric, and structured manner. The automation of systems to measure qubits and devices that enables improvement of each step in the design process will be crucial if efforts to scale devices beyond a handful of qubits are to be successful. Here, I will review the progress that I made in each of these areas.

Thesis Supervisor: Dirk R. Englund
Title: Associate Professor of Electrical Engineering and Computer Science

Acknowledgments

First and foremost, I would like to express sincere thanks to my thesis advisor, Dirk Englund, for giving me the opportunity to conduct research in his lab and for all of the guidance, motivation and inspiration he provided along the way. Dirk is always full of forward-thinking ideas and I hope to emulate those personal attributes going forward. More than any other one characteristic, I would like to acknowledge his willingness to continually explore innovative ideas relating to contemporary academic attitudes in our field. Much of the work presented in this thesis was enabled by his recognition that a robust, extensive computer-based infrastructure linking data acquisition and analyses and team members is key to future engineering efforts like those in the Quantum Photonics Lab. Additionally, I would like to express my gratitude to the other members of my thesis committee, Karl Berggren and Paola Cappellaro. I understand the costly nature of guiding students along their final dissertation journey, and I truly appreciate the support and sound advice offered by the members of my graduate committee all along the way.

The Quantum Photonics team that I have had the opportunity to work with has been nothing short of extraordinary. I will remember forever their endless willingness to lend a hand, both in and out of the lab, not to mention our relatively frequent trips to the "Muddy." They are fantastic colleagues and even greater friends.

I would like to give a special shout-out to my mentor, Tim Schröder, who helped me navigate entry into the lab and develop my own place on the team. Additionally, the contributions that I made couldn't have been possible without the help from our diamond fab team, Luozhou Li, Jiabao Zheng, Sara Mouradian, Noel Wan, and Kevin Chen. Lastly, let me mention a truly crucial member who helped bring the team together, Eric Bersin. Eric made significant contributions to the characterization of optical setups and measurements and will be the leading CommandCenter expert in the year(s) to come.

I would also like to thank Professor Ruonan Han who has been a valued collaborator, and taught me the design of cutting-edge CMOS technology. I will also always

remember Professor Luca Daniel, who gave me the opportunity to TA his 6.013 class on Electromagnetics and Applications numerous times. This opportunity provided me with an unexpected benefit, a solid foundation in microwave design for use in the control of qubits that influenced my research efforts reported in this thesis.

Numerous people work tirelessly behind the scenes to make it possible for individual team members to succeed. Even though I successfully avoided fab for the majority of time working on this degree, I really appreciate the essential contribution made by Mark Mondol's and Jim Daley's efforts to keep the NanoStructures Lab (NSL) up and running. It truly has been an honor to be a part of The Center for Integrated Quantum Materials (CIQM), a consortium bringing MIT, Harvard, Howard University, and the Boston Museum of Science together. CIQM enabled funding and the highest quality of collaboration and knowledge transfer, all accomplished within a community of scientists, engineers and friends. Many thanks to Robert Westervelt and Naomi Brave whose efforts to secure and maintain CIQM's position as a centerpiece in our field of study. I want to give a special thanks to the team at the Boston Museum of Science, so many of whom have become special friends. Carol Lynn Alpert, Megan Litwhiler, and Karine Thate have the remarkable ability to wade through the technical language so littered with jargon coming out of academia, and translate the message in consumable units for the community. The opportunity to work with the Museum staff not only enhanced my capacity to teach, but also to more effectively interact with colleagues in our own engineering community.

To my friends who have been so supportive from my high school days until now, I say thank you. By celebrating accomplishments with me on the good days, and easing my frustrations on those less upbeat occasions, their support has been nurturing. Especially, of course, my heart goes out to Jenna, who has had to endure endless conversations centered on my research, and, I am convinced, could have delivered my thesis defense with a real flair. She has been the best partner I could have ever hoped for and her unending support has made this experience more fulfilling than I suspect she will ever know.

Most importantly, thank you to my parents. It goes without saying that their love

and support has been a constant in my life, especially during occasionally challenging moments leading to this point in time. From the time they first learned of my dream to study at MIT, now over 15 years ago, they have provided me with all the opportunities necessary to accomplish the dream, and taught me how to navigate the complex space necessary to turn the dream into reality. I will always look up to my parents – they have no idea how much I'm still learning from them. Thank you.

Contents

List of Figures

1-3 **Summary of the NV Center in Diamond. a)** A substitutional nitrogen atom replaces a carbon atom in the diamond lattice. To complete the NV, one of the four neighboring carbons is removed, leaving behind a vacancy in the lattice. Because four different carbons can act as the vacancy, there are four orientations of the NV center in a diamond crystal. **b)** The defect can acquire an additional electron from the valence band, making it a negatively charged nitrogen-vacancy center (still abbreviated as NV). The ground state of an NV is a spin triplet, where the initial splitting between $|m_s = 0\rangle$ and $|m_s = \pm 1\rangle$ is due to a spin-spin interaction. The degeneracy of $|m_s = \pm 1\rangle$ can be lifted using a magnetic field via the Zeeman effect. Finally, these states' degeneracies are lifted due to the hyperfine coupling with the nitrogen's nuclear spin. Shown here is an example of an ^{15}N (the nitrogen of choice for implantation) which has a spin 1 nucleus. I only show the excited state that exhibits a $m_s = 0$ spin-like characteristic in the excited state manifold. The state will shift in energy with axial strain, and the degeneracy will be lifted with transverse strain into $|E_x\rangle$ and $|E_y\rangle$. **c)** Under 532 nm excitation, we can observe the photoluminescent (PL) spectrum from the NV center. The sharp transition at 637 nm is known as the zero-phonon line (ZPL) and is accompanied by a broad phonon sideband (PSB) extending out to approximately 800 nm. (Inset) With the help of a computer, a resonant laser is scanned across the ZPL and the light emitted into the PSB is collected to further resolve the $|E_x\rangle$ and $|E_y\rangle$ transitions, a process known as photoluminescence excitation (PLE). **d)** The ground state spectrum can be resolved by optically detected magnetic resonances (ODMR). Microwave energy is swept across the transitions from $|m_s = 0\rangle$ to any of the $|m_s = \pm 1\rangle$ states, and a dip in fluorescence is observed upon resonance with the microwave field. 47

2-5 **QR Locator Processing Validation.** An overview of the two main components to processing QR Locators is shown. **a)** The initial processing step is decoding/reading. This tool outlines every step and calculated value used to process the images along with four panels showing the raw image with a potential inversion (axis 2, or y axis in the example), a representation after refactoring to square pixels if they were not in the original image, the result of the application of a low-pass filter, and the binary mask used to locate the bounding box of the QR Locator. Each sector reproduces calculated positions for feature detection through decoding. Clicking on the decoded value of a bit brings up histograms of the internal distributions calculated from the original image. In this QR Locator design, there are more opportunities to sample the reference pixel values for a logical 0 bit. In this example, I have zoomed into a single QR Locator, but there were four total in the field of view. The inset with a blue border shows which pixels are sampled when interpreting the value of a bit. **b)** The optional next step is to take the information from the reader in **a)** and perform a point spread function (Gaussian) fit to all primary and secondary (smaller) bounding box markers. Again, I have zoomed into only one of the QR Locators. This one appears inverted, because the first step required a y-inversion to decode correctly. The results of each fit are stored and can be presented by clicking on the marker of interest. 60

List of Tables

Chapter 1

Introduction

Solid-state color centers provide an excellent platform for quantum information processing because of their potential for scalable designs, integrated fabrication and room-temperature communication (photonics). The central challenge in building quantum computers and long-range quantum networks is to distribute entanglement across multiple, individually-controllable, quantum memories. The nitrogen-vacancy color center (NV) in diamond has stood out among others due to its exceptionally long spin coherence time [12], optical addressability [137], neighboring nuclear spins [2], and optical coherence at low temperatures [172]. Because of these properties, it is the only solid-state color center that has been successfully entangled in a quantum network, and broken Bell's inequality [68]. Despite all of this success, to date, these experiments have been performed using NV centers that were formed naturally during diamond growth and using a solid immersion lens (SIL) to extract light.

To scale model systems in a technologically useful manner, we cannot rely on randomly-occurring natural systems, it will be necessary to engineer devices with NVs that can be controlled spatially. Specifically, to overcome the low rate of interaction between optical fields and solid-state defects, the engineering of cavity devices is essential. Not only will the cavities enhance the light-matter interaction through the Purcell effect [86, 147], they will enable high collection efficiency into a desired optical mode [102]. In Figure 1-1, a series of techniques representing the evolution of emitter-cavity technology is shown. The most significant advancement

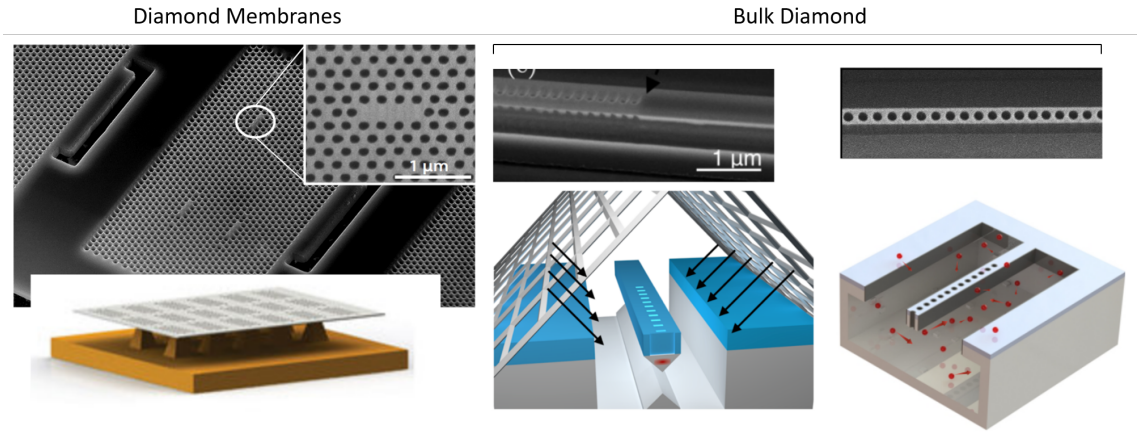

Figure 1-1: **Evolution of Solid-State Fabrication Techniques. (Left)** Earlier efforts to fabricate 2-dimensional cavities on diamond membranes [147] involved picking-and-placing each 200 nm thick membrane by hand onto a silicon chip that could be etched under the diamond. At the time, this was the most direct and straightforward strategy to prepare a cavity that was undercut (a necessary component for a high-Q cavity). The largest chip sizes were on the order of 100×100 µm^2. **(Center)** One of the first successful undercut techniques on bulk diamond (>500 µm thick) was the use of an angled metal cage to direct the etching ions at an angle that would result in a free-standing structure [16, 14, 30, 150]. **(Right)** A variation of the angled-etch method yielding a rectangular cross section, opened the door to the introduction of a two-dimensional technique [101, 182]. In what is perhaps the most notable historical advance associated with the evolution of fabrication techniques was the migration from membranes to bulk diamond systems that allowed expansion of the usable area to a 4×4 mm^2 chip scale.

occurred when a technique to undercut the diamond was developed using an angled-etching technique [16, 14, 30, 150]. This opened the door to take full advantage of the 4×4 mm^2 chip surface for device fabrication, in addition to improving NV optical properties [141].

The next significant challenge is to develop strategies designed to navigate a sample autonomously while collecting data on a large number of NVs. Under these conditions, the critical need to establish a statistical foundation to support design decisions can be achieved. In this thesis, I demonstrate the utility of this strategy by:

- Demonstrating the utility of an emitter-device alignment technique enabling fabrication of photonic devices registered to NVs.

- Characterizing many hundreds of sites to find candidates for multi-qubit regis-

ters.

- Correlating the NV's host nitrogen isotope with the optical linewidth of the emitter to understand the effect of implantation.

- Demonstrating the capability to characterize aligned devices.

An early quantum network is being developed here in the greater Boston area between MIT, MIT Lincoln Laboratory, and Harvard University. A schematic of this network can be seen in Figure 1-2. The operating principle of the network is to have a quantum memory coupled at each node that can facilitate the distribution of entanglement [68]. The entangled qubits can then be used as resource for quantum key distribution, distributed quantum computing, blind quantum computing, clock synchronization or general metrology.

Precisely which quantum memory will maximize performance in these systems is currently an open question. As discussed above, the NV center is a highly desirable candidate. A majority of the work in this thesis uses the NV defect to perform the relevant experiments. The geometry and energy structure of the defect center in diamond can be seen in Figure 1-3. The only principles of physics addressed here are those that are relevant in this thesis. Additional details will be elaborated when needed.

While the NV is among the most investigated and promising of defects for quantum memories, I will discuss a series of investigations surrounding use of the silicon-vacancy center in diamond in Chapter 3. The SiV holds great promise as the industry moves forward, primarily due to the smaller inhomogeneous distribution of its optical transition. This is partially due to an additional inversion symmetry that the NV lacks. There exist readily available ion sources for silicon that can be focused onto the diamond surface allowing for precise implantation location. Unfortunately, a source capable of focusing a nitrogen ion beam is unavailable for the case of the NV production. The largest drawback is that the SiV's spin properties require a great deal more engineering to be useful in quantum information (QI) applications [162].

I will explore novel registers, clusters of memories, by investigating multi-qubit

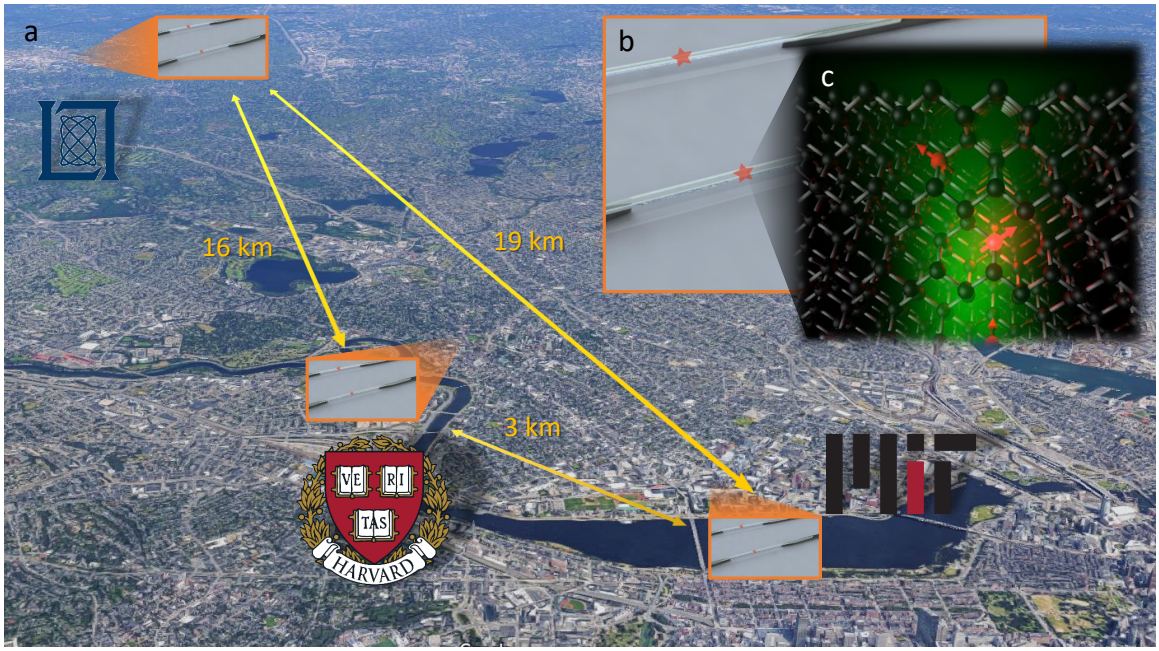

Figure 1-2: **Greater Boston Area Quantum Network Schematic. a)** A map of the greater Boston area indicating the nodes of a quantum network connected by optical fiber. This metropolitan-scale network will serve as the future testbed for quantum technologies described in this thesis. **b)** At each node of the network, a quantum node will be optically connected to the network to facilitate a quantum memory. Here, a schematic of a diamond nanowire with an NV center coupled to an optical backbone that can then be connected to the optical network is shown. **c)** A cartoon showing near-surface (not-to-scale) NV defects in the diamond lattice. An off-resonant green laser is exciting one of the NVs that, as a result, emits red fluorescence.

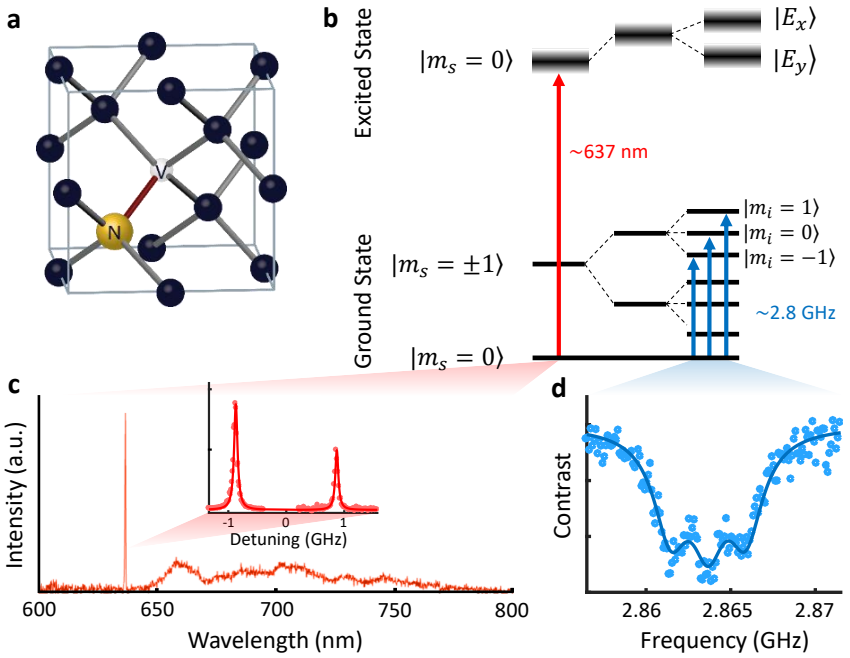

Figure 1-3: **Summary of the NV Center in Diamond.** **a)** A substitutional nitrogen atom replaces a carbon atom in the diamond lattice. To complete the NV, one of the four neighboring carbons is removed, leaving behind a vacancy in the lattice. Because four different carbons can act as the vacancy, there are four orientations of the NV center in a diamond crystal. **b)** The defect can acquire an additional electron from the valence band, making it a negatively charged nitrogen-vacancy center (still abbreviated as NV). The ground state of an NV is a spin triplet, where the initial splitting between $|m_s = 0\rangle$ and $|m_s = \pm 1\rangle$ is due to a spin-spin interaction. The degeneracy of $|m_s = \pm 1\rangle$ can be lifted using a magnetic field via the Zeeman effect. Finally, these states' degeneracies are lifted due to the hyperfine coupling with the nitrogen's nuclear spin. Shown here is an example of an ^{15}N (the nitrogen of choice for implantation) which has a spin 1 nucleus. I only show the excited state that exhibits a $m_s = 0$ spin-like characteristic in the excited state manifold. The state will shift in energy with axial strain, and the degeneracy will be lifted with transverse strain into $|E_x\rangle$ and $|E_y\rangle$. **c)** Under 532 nm excitation, we can observe the photoluminescent (PL) spectrum from the NV center. The sharp transition at 637 nm is known as the zero-phonon line (ZPL) and is accompanied by a broad phonon sideband (PSB) extending out to approximately 800 nm. (Inset) With the help of a computer, a resonant laser is scanned across the ZPL and the light emitted into the PSB is collected to further resolve the $|E_x\rangle$ and $|E_y\rangle$ transitions, a process known as photoluminescence excitation (PLE). **d)** The ground state spectrum can be resolved by optically detected magnetic resonances (ODMR). Microwave energy is swept across the transitions from $|m_s = 0\rangle$ to any of the $|m_s = \pm 1\rangle$ states, and a dip in fluorescence is observed upon resonance with the microwave field.

nodes. Specifically, I will discuss a technique we introduce to take advantage of the NV's large inhomogeneous distribution to localize three NV centers within a diffraction-limited spot. While not achieved in experiments thus far, in principle, if these NVs are sufficiently close to one another, they could coherently interact via their dipole moments. Nonetheless, I will consider the machinery necessary to read and write to these quantum memories in a non-destructive manner. This type of multi-qubit node provides one path toward an error-corrected logical qubit.

In the end, regardless of the qubit selected, I want to stress the view that the infrastructure presented in this thesis is designed to remain agnostic to the specific defect under consideration. It is intended to advance the engineering and process control of general solid-state quantum platforms. Towards this end, I present the application of the platform to NV centers in Chapters 5 and 6 by explicitly studying the NV implantation step and subsequent processing in a statistically rigorous manner.

Chapter 2

Laboratory Framework and Automation Infrastructure

There are many software packages that exist with the explicit goal of streamlining data management in a laboratory environment. The general category of this type of software is commonly referred to as "Laboratory Information Management" (LIM). Originally designed for sample management, there are data management and analyses applications designed for the biomedical field, as well. However, very few products are available to support more generic forms of research. The work outlined below represents an overview of an extended LIM infrastructure with a minor focus on microscopy and spectroscopy. The importance of this type of development, especially in relation to quantum computing, can be understood by considering the number of companies and startups turning to solutions based on this data management format. For example, Labber was founded in 2015, and in 2017, IBM's "Qiskit" and Rigetti's "pyquil" first committed to the development of their systems [96, 82].

In this chapter, I address the contents of two patents in addition to the detailed consideration of elements in the architecture. The first protects intellectual property surrounding the structure and purpose of autonomous microscopy [181]. The second deals with the implementation of an optical objective with an embedded microwave delivery system [180].

2.1 Database

One of the most important components associated with building an infrastructure for data-collection and data-driven design, is a well-designed data management back-end. File systems spread across multiple computers collecting data lack two key ingredients:

1. An organizational rigor that all users of the system must follow; in the data collection realm, all participants typically adhere to their own file-saving conventions.

2. Physical reliability to protect against hard-drive failure.

The first of these issues is remedied by implementing a MySQL database. A relational database (as is a MySQL database) is a set of tables with structured data that can reference other entries in the database. The structured data aspect of the design facilitates the compilation of data sets dependent on any subset of the tables and/or fields within the tables to establish correlations that otherwise may remain hidden in flatter data structures that do not obey a common schema (e.g., a file system).

The second issue can be easily fixed by ensuring that the database itself resides on RAID storage. This is accomplished by using a network-attached storage (NAS) Synology DiskStation. The two methods used to edit this database will be a web-interface front-end for users and an SSH API for the experimental front-end. Because all of these rely on an active network connection, it will be important to consider temporary offline buffering of data on experimental client computers.

The database schema, as shown in Figure 2-1, is designed to be extremely flexible while maintaining well-structured data tables. For example, the database does not specify a particular set of actions, rather a "meta-table" is specified that can store the necessary descriptions of action types dynamically. These actions are intended to reflect any and all sample manipulations, from clean-room processing to running experiments to sample shipment. Similarly, the types of data (*general*, *local*, and

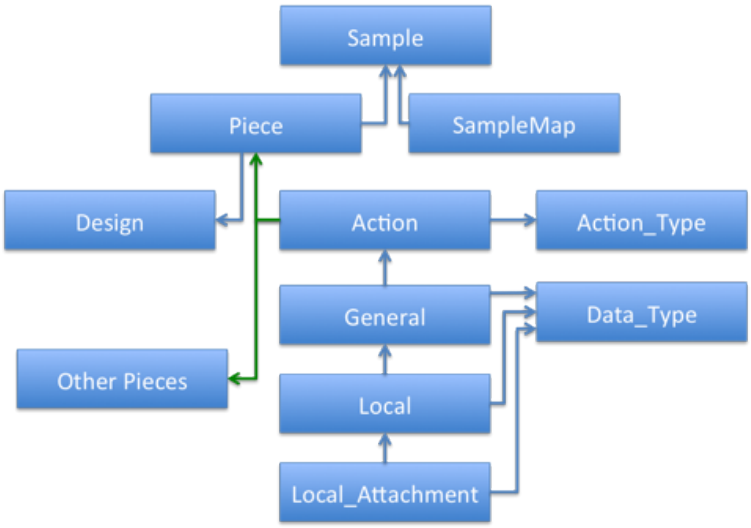

Figure 2-1: **Conceptual Representation of SQL Database Schema.** While it is an over-simplification, the important tables and ideas are captured. Blue arrows represent a ForeignKey and green arrows represent a ManyToMany relationship. In practice, there are additional tables providing the "reverse" relationship between objects in the database making backwards traversal over the relationships possible.

local_attachment) are all free to define any data type that may be required (e.g., wide-field images, spectra, T_1 and T_2 spin measurements). Confocal imaging of fluorescent emitters is a good example of data acquisition in the *general* category, while consideration of the spectrum at a point location on the confocal image would fit nicely into the *local* grouping. A representative example of a *local_attachment* form of data would be the results of a peak analysis of the spectrum.

The columns/fields in each table illustrated in Figure 2-1 is maintained by the MySQL engine itself which maintains consistency in the database. The columns identifying the custom action/data types are dynamically maintained by a python layer to preserve and verify the structure of incoming data.

Because these data are easily retrieved in various combinations and can be filtered by various conditions, you can imagine correlating any aspect of the engineering with any observable of interest.

2.2 Front-End

The modular experimental front-end (referred to as "CommandCenter") will be installed on all lab machines capable of acquiring data on color centers or devices. It is built around a modular architecture that facilitates the straightforward combination of relevant measurements while ensuring the integrity of each module (responsible for a single measurement) is well-maintained. Using this approach, a more complicated experimental design can be implemented without the need to manage the individual input and output of components, while being confident that all relevant data and metadata are saved correctly.

2.2.1 Architecture

A screenshot of the application can be seen in Figure 2-2a. The user can load modules from the various menus at the top of the application and operate them using their controls on the left side panel. All of these control containers can be adjusted in size by dragging their bottom edge, or minimized by clicking their top edge. The modules listed in the menus are displayed dynamically based on the contents and structure of the folders containing them on the filesystem. Once loaded, CommandCenter will render all controls specified by the module. These controls are known as "prefs" and are defined as properties of the module's MATLAB class. The prefs themselves are self-contained classes that are responsible for their user-interface's (UI) representation as well as subsequent data cleaning and validation. These are modeled after Django's implementation of Fields within models [59].

The rightmost menu item "Paths" plugs into another manager that is responsible for routing physical paths on the setup. For example, you may have a switch or flip mirror that can route the microscope to various measurement tools. Because imaging modules and experiments can both declare a path, the path manager allows aliases to be assigned in the case that two names are used for the same physical path. Likewise, if no paths are capable of automation, all paths can be an alias to a manual notification.

The two main panels on the right are designed to contain the images captured by an active imaging module, and data captured by a running experiment module. These panels can be rearranged with options under the "File" menu and their size can be adjusted by dragging the bar between them. The panel displaying the image provides user interface (UI) elements to help the user visually adjust the region of interest (ROI) of the imaging device and control where the stage is positioned relative to the ROI origin. This functionality is all self-contained in the "SmartImage" class.

CommandCenter can be segregated into two categories: *core code* and *user code*. The core code is primarily responsible for managing the user interface, organizing selected modules, logging, and managing unhandled exceptions. The user code, organized into modules, is the set of code that controls hardware and experimental flow. Figure 2-2b illustrates the code architecture at a high level, as well as an example of the flow through the full stack of modules in a model experiment in Figure 2-2c. A subset of the logs are sent to a centralized server. This allows authorized code administrators and developers to investigate usage patterns and recognize the most urgent errors to be addressed. The logs are accompanied by enough GitHub data to have an exact snapshot of the code being run when the logs are generated.

Modules are required to inherit certain core code classes that provide required functionality and templates allowing them to plug into their corresponding manager. The two base classes inherited by all modules are Base.Singleton and Base.Module. The singleton behavior enables classes to be instantiated only once but retrieved with separate calls. This is important for the instances representing physical hardware because that instance must maintain an accurate representation of the state of the hardware. If two instances existed, they could independently update the physical hardware without the other knowing. Base.Module brings together functionality to implement rendering the settings panels on the left for a particular module and makes certain that CommandCenter is aware of the module's existence.

In an effort to preserve equipment longevity and general safety, the application is equipped with an "inactivity" monitor. This is a 30 minute timer that is reset with every application interaction and paused during any module's method evaluation

(e.g. an experiment evaluating or image acquisition pauses the timer). When the timer times-out, CommandCenter executes a set of housekeeping routines and calls all loaded module's inactivity routines if defined (close shutters, power down equipment, reset voltages, etc.) and presents all actions taken to the user; under the assumption that modules properly return their actions as a string from the inactivity method.

Debugging within the CommandCenter environment can be accomplished using MATLAB's debug architecture. However, CommandCenter managers evaluate module code in a "sandboxed" environment to prevent the elevation of unexpected errors in user code to a level resulting in fatal crashes of the CommandCenter application. These sandboxes require code to enter and exit the sandboxed environment which necessitates additional restrictions with the debug tool. Exiting code evaluation without evaluating the appropriate sandbox exit block will result in getting stuck in the sandbox environment. As such, a safeguard against prematurely "quitting" debug mode is launched when CommandCenter is loaded. The best practice is to proceed through debugging with "continue" such that the sandbox exit sequence can take place regardless of an exception in the code.

2.2.2 Autonomous Navigation

Re-visiting sites on physical samples is a required feature of our data acquisition platform. There are a couple of techniques that can be used to make this possible, one of which will actually work under our constraints. First, extremely precise stages that can move to a target location with micron-scale accuracy and precision could be employed. To repeatedly revisit sites, the sample would also require positioning on the stage with the same accuracy and precision. This is an unreasonable expectation given our constraints. Not only do our samples change in size and shape, repeated visits to the same site in different setups is necessary, including setups that operate at cryogenic temperature. Cryogenic stages present an additional accuracy challenge when operating in a closed-loop mode over the full sample's position (mm-scale). This brings us to our second solution, patterning a coordinate system directly on the sample's surface. Under proper illumination, this coordinate system can be observed by

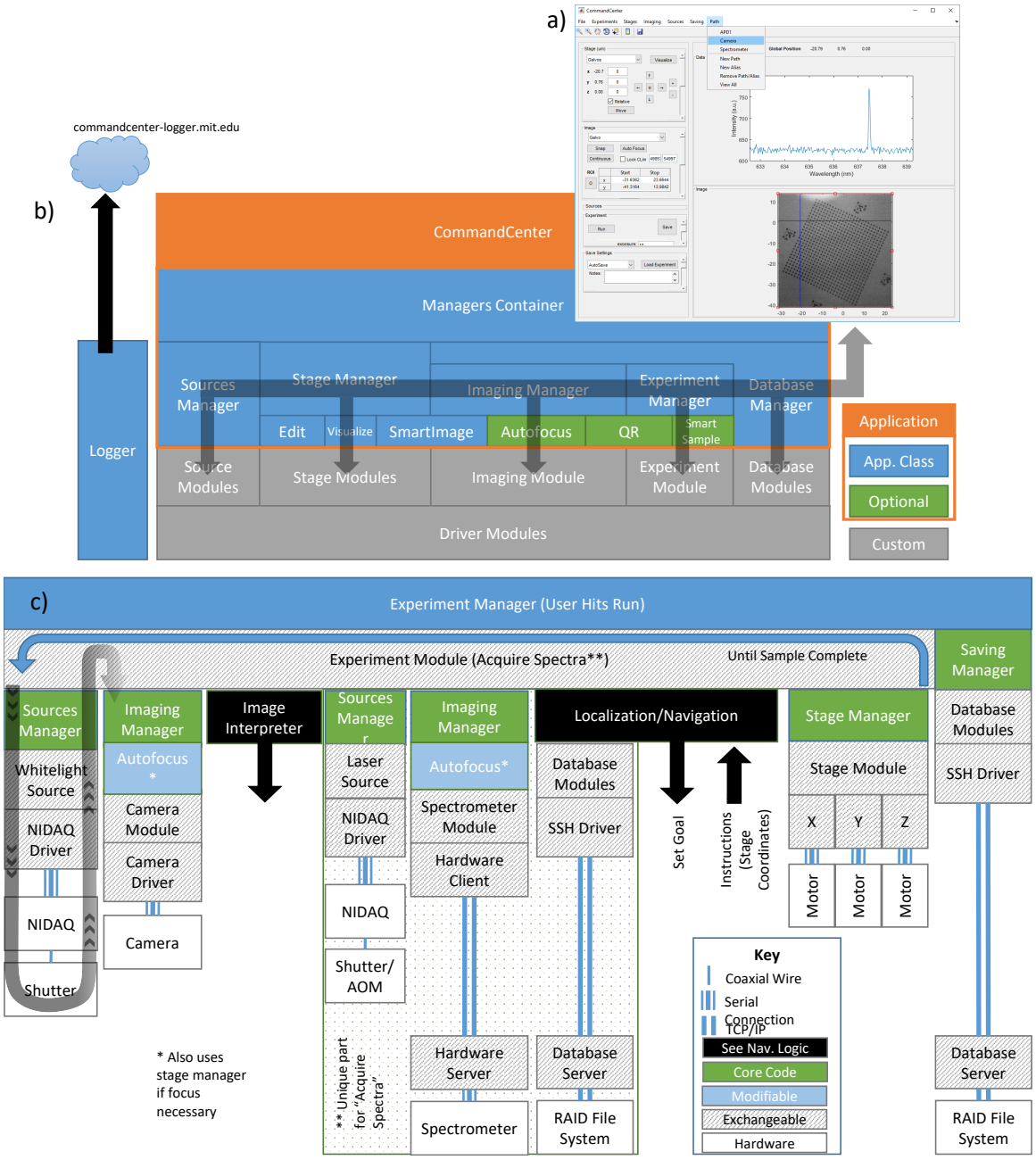

Figure 2-2: **Modular Front-End.** **a)** A screenshot of the UI. The menus across the top allow selection of modules which can then be controlled by UI elements in the left set of panels. **b)** The underlying block diagram outlining the architecture of the experimental front-end. All objects represented in blocks are instantiated as a MATLAB class. The primary purpose of the managers is to act as a broker between the UI and the loaded modules and prevent errors from propagating beyond a module. **c)** An example traversal of methods showing the full-stack representation from the high-level user interface down to the lowest level hardware components. The black arrow on the left shows how to traverse the figure's stack representation.

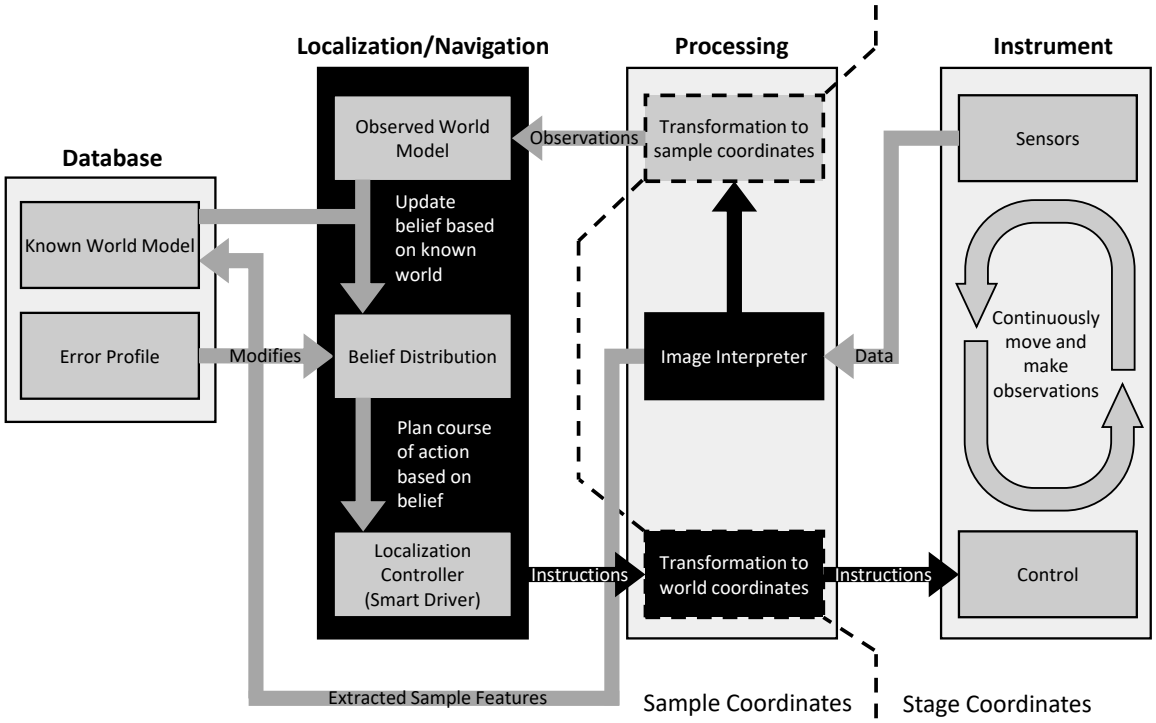

Figure 2-3: **Sample Navigation Logic.** The localization system takes observations from the instrument's sensors as input. Once interpreted and transformed into sample coordinates, data are used to update the observed world model. Finally, coupled with the known world model, the localization system generates a belief as to where the instrument may be located.

the microscope's camera allowing a computer to identify its location on the sample's surface.

A core plugin to CommandCenter is the autonomous navigation component. This component is given a target position on the sample and provides a series of instructions to navigate towards the target. The primary element of the system is a machine-vision enabled sensor to detect patterns on the sample to interpret an encoded position. Figure 2-3 displays a block diagram of how the information flows through the system to the relevant components. In this diagram, the database is stored locally in memory because there is no need for it to be permanent since the instrument can always relearn its location if necessary.

QR Locators

There are many techniques that can be used to create unique markers on the sample surface. Previous work that successfully demonstrated alignment of structures to prescreened sites have used relatively simple markers that are replicated across the chip [132]. While techniques like this can be employed in the case of manual demonstrations, the approach will not permit scaling-up to chip-level engineering. To successfully scale to that level, unique markers must be created. To this end, an alphanumeric labeling scheme has been used to label chip components by many groups. While an alphanumeric scheme is reasonable and effective in many if not most forms of human enterprise, the information processing load is greater in the computer realm, and, more important, by using a digital strategy a denser representation that a machine can easily read can be created. This strategy was first implemented in 1994 when DENSO WAVE released a 2-dimensional barcode, the Quick Response (QR) Code [37]. Here, I add our QR Locators to the ecosystem of 2-dimensional codes.

The physical markers used by the machine vision portion of the navigation plugin are custom-designed binary codes etched into the diamond surface. These markers have similar features to that of QR codes - a 2-dimensional array of bits. Figure 2-6 shows an example of the layout and design of these markers. The marker pictured uses 16 bits to encode the *location*, 4 bits to encode the *version*, 1 bit as a constant *pad*, and 3 bits as an error-detecting *checksum*. The version bits allow some flexibility in the encoding of the *location*, *checksum* and *pad* bits if updates are required. The *pad* is a constant bit that helps identify this as a marker, once the machine vision system locates the three corner circles of the marker.

The internal structure of a QR locator's bit was investigated to determine which design provided the most contrast in the optical microscope, the essential functional element of the system. Four different designs were considered, as depicted in Figure 2-4. The clearest and most trivial design was devoid of internal structure, consisting of a simple etched square. In the second family of designs, I took advantage of polarization effects from the reflected LED illumination. The final design consisted of a 3×3 grid

of pillars. Scanning electron micrographs (SEMs) of these four designs can be seen in Figure 2-4a.

Early marker development efforts produced decoding algorithms that read the final pillar design flawlessly, ruling out the need for a thorough study of polarization design. Figure 2-4b shows an example of the optical image associated with the horizontal striped design. Even in this image, you can begin to understand why the pillar-design is so effective. Rather than using interference or polarization effects which require extra care in preparing the optical path of the microscope, the easiest-to-implement and most robust design is to simply scatter as much light as possible within each bit. Two of the three framing circles in Figure 2-4a are designed to be asterisks and are based on the same logic underlying the bit's pillar-design to maximize the edges that will scatter incident light.

Clearly, an in-depth consideration of the design of markers is an important aspect of work presented in this thesis, and up-to-date information on the evolution of the design (including a completely new bit layout seeking to improve the information content to footprint ratio) will be available through CommandCenter's GitHub wiki [178].

Marker Detection Algorithm

The markers were designed with their specific application in mind. Unlike QR codes used universally, use of our markers are limited to imaging via optical microscopy from the top. Consequently, accounting for affine transformation resulting from a nondirect perspective is unnecessary. As such, our degrees of freedom include translation, scale, and rotation. QR readers that are used in standard mobile devices, and are available through OpenCV [39], expect the user to image the QR code "well" enough to allow their algorithm to detect the QR code [18]. The detection occurs when a row of pixels matches a certain signature present in all QR codes. In QR codes, this signature is produced with nested square features. As such, when imaging at some rotation, it is difficult to detect the signature because it is a function of the angle. In our application, detection and readout of markers at any rotation is necessary.

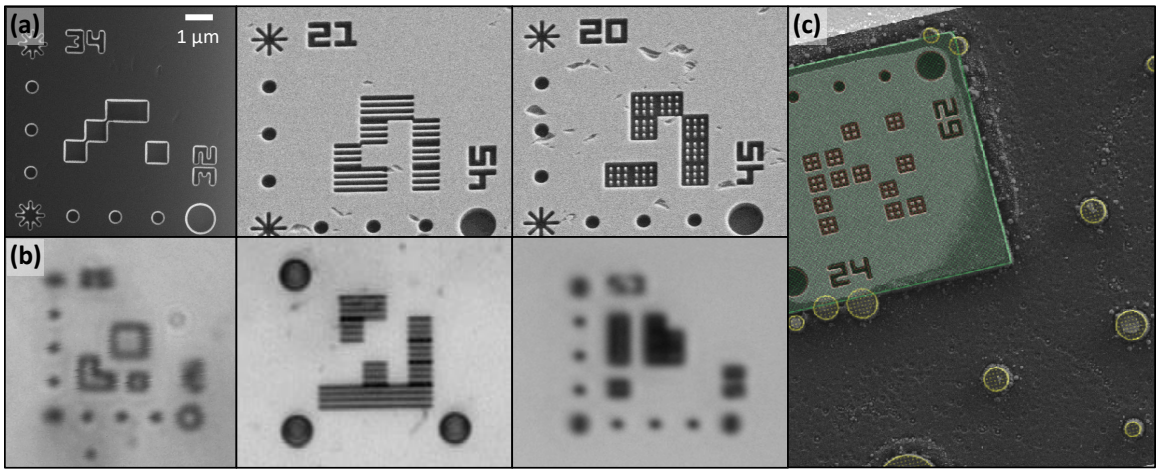

Figure 2-4: **Experimental Pixel Designs.** Row **(a)** A set of 3 SEMs depicting distinct internal bit designs for the QR marker. From left to right, the trivial design has no internal structure, resulting in a simple etched square. The next family of designs is inspired by linearly polarized illumination — a horizontal or vertical striped pattern is used to preferentially interact with the corresponding polarization (only the horizontal is shown). Finally, a set of pillars is tested to increase the length of light-scattering edges present on the marker's bits. Row **(b)** A set of images taken under the white light optical microscope. These are the images used for processing and decoding markers. The optical images correspond with the bit's family from the SEMs shown in **a**, but they are not precisely the same QR Locators. **(c)** An example of a second electron beam lithography (EBL) write overlaid with the QR Locator coordinate system using the *EBL markers* described in Figure 2-6. The green and red colors correspond to the designed QR Locator block. The yellow coloring corresponds to the locations of pillars for detected fluorescent sites registered to the QR Locator coordinate system corresponding to NVs.

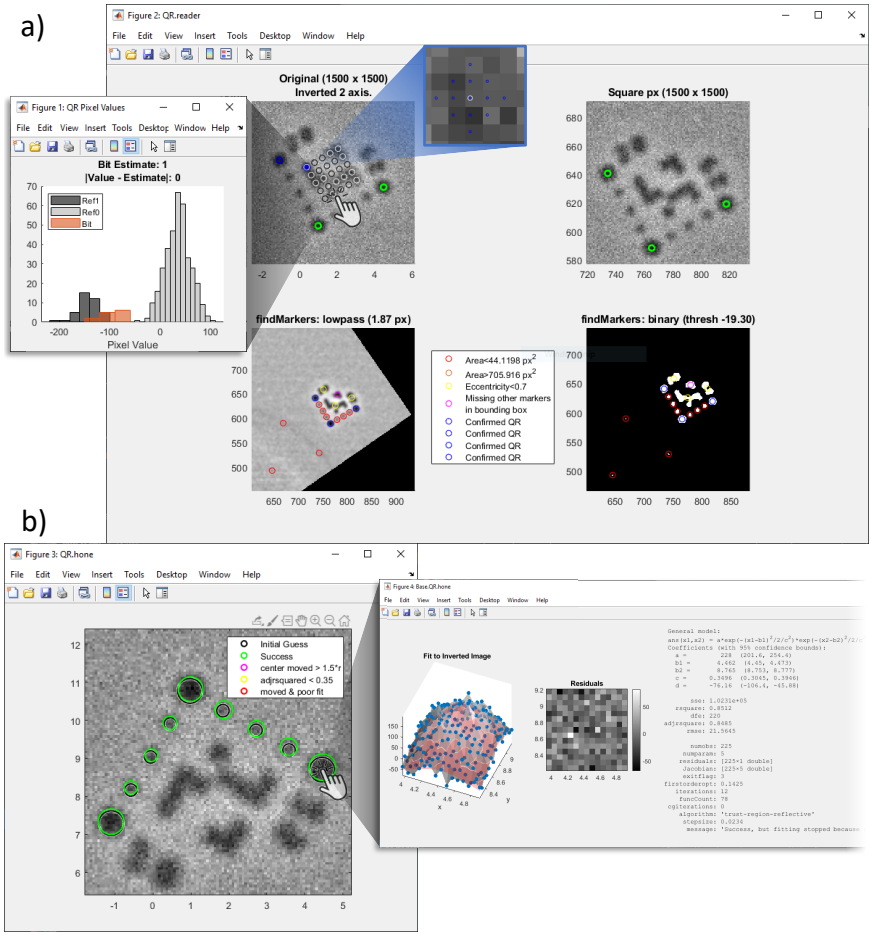

Figure 2-5: **QR Locator Processing Validation.** An overview of the two main components to processing QR Locators is shown. **a)** The initial processing step is decoding/reading. This tool outlines every step and calculated value used to process the images along with four panels showing the raw image with a potential inversion (axis 2, or y axis in the example), a representation after refactoring to square pixels if they were not in the original image, the result of the application of a low-pass filter, and the binary mask used to locate the bounding box of the QR Locator. Each sector reproduces calculated positions for feature detection through decoding. Clicking on the decoded value of a bit brings up histograms of the internal distributions calculated from the original image. In this QR Locator design, there are more opportunities to sample the reference pixel values for a logical 0 bit. In this example, I have zoomed into a single QR Locator, but there were four total in the field of view. The inset with a blue border shows which pixels are sampled when interpreting the value of a bit. **b)** The optional next step is to take the information from the reader in **a)** and perform a point spread function (Gaussian) fit to all primary and secondary (smaller) bounding box markers. Again, I have zoomed into only one of the QR Locators. This one appears inverted, because the first step required a y-inversion to decode correctly. The results of each fit are stored and can be presented by clicking on the marker of interest.

The signature of our QR locators consists of three bounding circles that "frame" the rest of the binary code, thus marking its position. Because of their circular character, they look the same from all angles, simplifying our search algorithm:

1. The image is low-pass filtered using the primary marker's radius/4 as the standard deviation of the Gaussian kernel.

2. The image is then translated into a binary image using a threshold. The threshold is calculated as the median of all pixel values in the image plus n standard deviations. The default is $n = 5$.

3. Contiguous regions are discovered and characterized by their eccentricity and area. Regions that fall within the valid thresholds of these parameters are candidates for the marker's signature.

4. A depth-first search is performed on these candidates. If a particular signature circle forms a right angle with two additional candidates, and falls within the correct dimension window, that marker is flagged as a potential origin for a marker.

5. With the origin of a marker known, continued efforts to read the binary values encoded in the marker are made. This is performed by first surveying regions of the code that are known to correspond to pixel values representing a logical 1 and a logical 0. The pixels comprising the 24 unknown bits can then be statically compared to these known distributions using p-tests. This form of sorting has the added benefit of providing us with a confidence for each pixel.

6. Once pixels have been classified, the binary code is checked for errors using the embedded checksum value. If the code passes this test, the candidate marker is confirmed to be an actual marker.

7. For each actual marker, I go back to perform a more accurate alignment to the code to increase precision. The simulated marker image is fit to the raw pixel

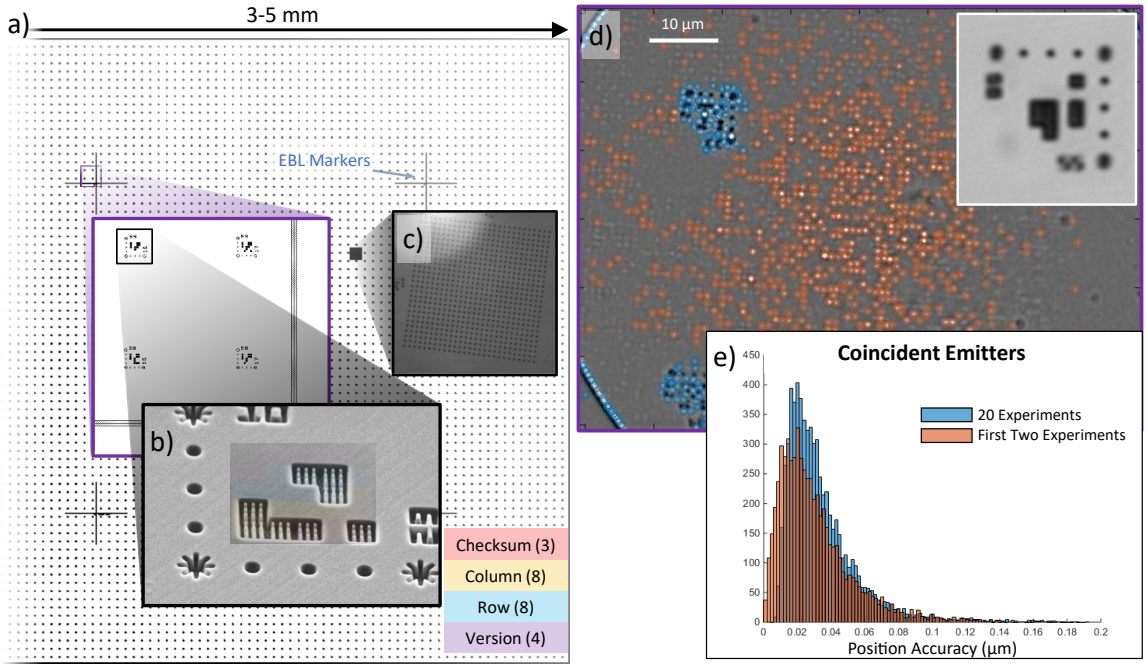

Figure 2-6: **Sample Registration. a)** Example of full chip patterned with markers, EBL alignment markers and spherical aberration correction grids (c). **b)** An SEM of an early version of the QR Locators. **c)** An optical image taken in the microscope under white light showing the grid of circles used as our aberration correction grid. **d)** A microscopic fluorescence image of the sample, showing emitters located by fluorescence detection. Orange circles indicate peaks that have been detected and identified as emitters, blue circles indicate peaks that have been spatially filtered either due to proximity to the frame border or masked by a location marker. The purple border roughly maps to the scale of the purple border on the left. The inset shows the marker captured with white light microscopy. **e)** A histogram showing the standard deviation of distances between emitters repeatedly registered in the global coordinate system over the course of 20 trials (blue) and the first 2 trials (orange). Nearest neighbors between runs were considered the same emitter.

values in the original image to retrieve a best-fit and precise coordinate that the marker encodes.

Figure 2-5 shows an example of different parts of this algorithm and the user interface to aid the user's effort to understand the steps being taken by the algorithm. This presentation of metadata in a logical and efficient manner is crucial to debugging systematic issues and understanding what adjusting parameters are doing under the hood.

By coupling the sample localization components to fluorescent peak-detection, we

can register the location of fluorescent emitters to the global sample coordinate system. The right column of Figure 2-6 displays an example of an extracted frame of this process. The histogram below the image represents the results of 20 alignment experiments across the surface of the chip, as the chip is re-positioned to a new, random orientation on the stage for each experiment. These data suggest a localization precision of 20-30 nm.

2.2.3 Spherical Aberration Correction

Image distortion exists to some degree in every imaging system, and is primarily manifested in radial and tangential components. Radial distortion is caused primarily from the shape of the lens; rays entering the lens at different radii from the optical axis are focused to different locations. Tangential distortion is typically a result of lenses that are not perfectly orthogonal to the optical axis.

A Brown-Conrady model is used to account for radial and tangential distortion. Basically, the system navigates to an aberration-correction region identified as an array of EBL patterned circles. The equations below are used to select the vector $a = [a1, a2, ..., a5]$, such that the error between the true grid locations and the imaged grid locations is minimized. An example of this can be seen in Figure 2-7.

$$\begin{aligned} radial &= (1 + a_1 r^2 + a_2 r^4 + a_3 r^6) \cdot \hat{x} \\ tangential_x &= 2a_4 xy + a_5(r^2 + 2x^2) \\ tangential_y &= a_4(r^2 + 2y^2) + 2a_5 xy \\ BrownConrady &= radial + tangential, \end{aligned} \tag{2.1}$$

where $\hat{x} = [x, y]$, $r^2 = x^2 + y^2$, and $tangential = [tangential_x, tangential_y]$.

A handful of techniques designed to correct image distortion using the Brown-Conrady model are available. These models generally attempt to fit the free parameters referenced above, as well as the set of the camera's intrinsic and extrinsic

parameters that describe its angle relative to the scene and its focal properties such that a proper transformation to true spatial coordinates can be made [24, 65, 70, 190]. For our purposes, the camera's optical axis is perpendicular to our sample.

In addition to the location markers patterned on the sample (as discussed in Section 2.2.2), I include an "aberration-correction region" which is a 27x27 array of circular holes etched into the diamond. I generally assume that EBL is more precise and accurate than our imaging system and take the intended positions to be the actual positions in space. As such, the computer can optimize for spherical aberrations by enforcing a Brown-Conrady correction across the entire field of view. Multiple snapshots of our aberration grid are taken as it is moved across all parts of the field of view. The metric that is optimized is the mean error between the best-fit "perfect" square grid and the measured grid. Specifically, the steps taken after 10 images have been taken (for example) are:

1. Peak detection and fitting to obtain measured location of the grid: x_{ij}, y_{ij} (10 images; so $i = 1 : 10$, and a 27×27 grid, so $j = 1 :\sim 729$, subject to a few markers being out of the field of view or covered/not etched correctly).

2. Simulate a perfect grid x'_{ij}, y'_{ij} with scale, rotation and offset degrees of freedom to fit as closely as possible to x_{ij} and y_{ij}.

3. Match such that x, y and x', y' sets are correctly paired up (e.g. rearrange j if necessary).

4. Perform a particle swarm/nonlinear least-squares optimization where the function being optimized is:

   (a) For each i:

      i. $(x''_j, y''_j) = BrownConrady(x_j, y_j)$

      ii. Redo step 2 using x''_j, y''_j.

   (b) error = `mean(distance between` x''_{ij}, y''_{ij}, and x'_{ij}, y'_{ij}`)`.

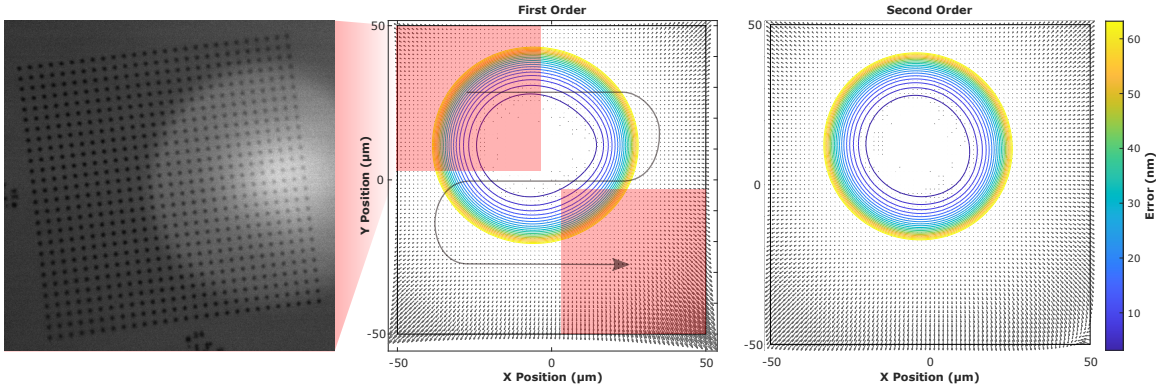

Figure 2-7: **Spherical Aberration Correction.** The microscopy image shown on the left corresponds to a partial region of the overall field of view that overlaps the aberration grid. The red square in the center image shows the location of this snapshot in relation to the full field of view. Additional snapshots are taken as the grid is moved through the overall field, as illustrated for one iteration shown by the arrow. The blue vector field shows the "error," or shift between the imaged locations and the corrected locations. A contour plot associated with the colorbar indicates the magnitude of these shifts (e.g. the length of the arrows). The right-most plot shows the vector field identified using the full second-order Brown-Conrady model described in the main text.

Figure 2-7 shows the result of implementing this protocol in a 100 µm × 100 µm field of view. Such a large field of view relative to the limited depth of focus of the 0.95 NA objective being used in this study certainly compromises the outcome of our focusing efforts. Imaging through this lens degrades the accuracy of location estimates of imaged markers near the edges of the field of view. Nonetheless, the computer can diagnose the required correction, as seen in Figure 2-7.

2.2.4 Pulse Sequences

Another important software component of the lab infrastructure is the design and implementation of a pulse-sequence infrastructure. It is important that the data structure of the pulse sequence be easily manipulated, efficiently optimized, and is freely scalable with the capability to perform abstractions. A tree data structure was chosen such that the *intent* of the pulse sequence could be captured. This was inspired by the structure of the commit tree in Git [168]. Each node on this tree can represent either a transition in the channel (e.g. "on" to "off") or the beginning/end

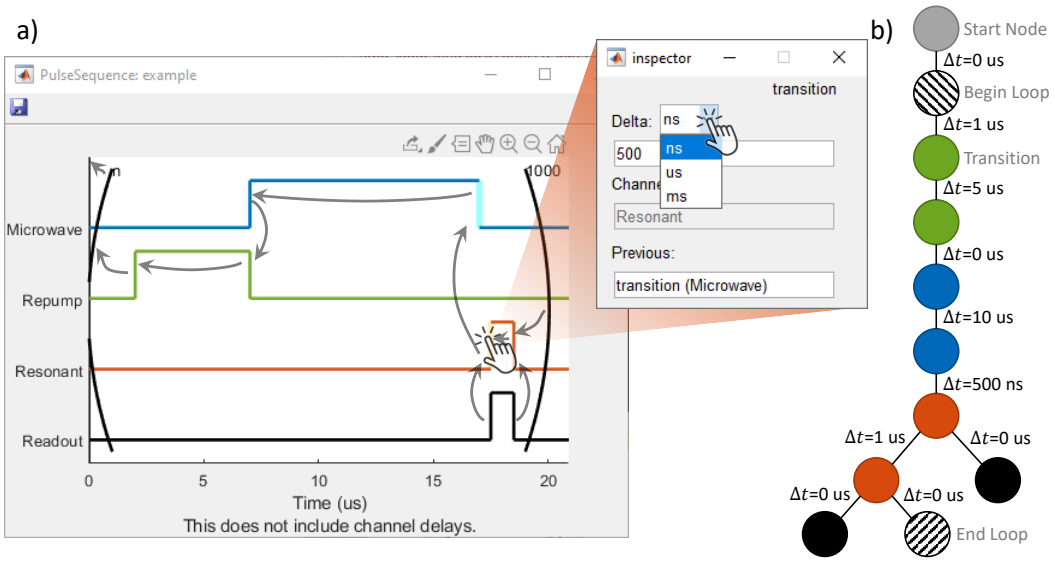

Figure 2-8: **Pulse Sequence Generation. a)** A screenshot showing the figure used for pulse sequence visualization and construction/editing. Overlaid arrows show the underlying relation of the tree stored in memory. A pop-up opens when clicking on a node allowing further editing of that node's properties. The two highlighted nodes correspond to the selected one and its parent. **b)** The corresponding tree in memory. Each circle represents a particular node from **a)** where the color matches the channel. Compilation requires traversing and flattening this tree.

of a loop. The edges of the tree correspond to a relative time offset from the parent node. This encodes a node's intent because it is specifically tied in time to a parent node. Thus if an update to the timing of an early node in the sequence is made, it is not necessary to consider all nodes down stream since they specify a time relative to our newly updated node. This can be seen in a simple example shown in Figure 2-8.

The editor for the pulse sequence is represented in time, typically how the experimentalist thinks about its progression. Right-clicking on the axes allows the user to add/order channels interactively. Once added, a right click will allow editing of a channel or initiate the beginning of a loop. To create a transition on a channel, a left click at the appropriate time will begin the process. Instructions to complete node creation (either a transition or loop) will be provided in the title of the axes. Part of this process includes selection of the parent node to be associated with that node. Clicking on an existing transition will allow editing of that node's properties

(including the relative timing to its parent node). When rendering the pulse sequence in the editor, a sequence instance will traverse the tree to determine absolute timings and allow the node to plot itself at the appropriate location in the x-y space.

Compilation is a relatively simple process. A JSON standard is created to represent an intermediate-compilation. Below is an example of what this might look like.

```
{
  "name": "Example",
  "units": "ns",
  "repeat": false,
  "channels": ["channel1","MW Switch","","channel4"],
  "sequence":[
    {"flags": [1,0,1,0], "duration":52,
      "instruction":"LOOP", "data":10},
    {"flags": [0,0,0,1], "duration":1032,
      "instruction":"CONTINUE", "data":null},
    {"flags": [1,1,0,0], "duration":126,
      "instruction":"CONTINUE", "data":null},
    {"flags": [0,1,0,1], "duration":1000,
      "instruction":"END_LOOP", "data":0}
  ]
}
```

The nodes have been converted into items in the "sequence" array. Special care must be taken for nodes that end up coinciding at the same absolute time. Here, a simple hierarchy can be used to choose what "instruction" should be used. The flags accompanying this instruction can be merged. If the merged flags are both attempting to change a state, it is impossible to determine what the user intended, and an error is raised.

A relatively simple generalization of this can be easily converted into a continuous

voltage space rather than the existing binary "on"/"off" space. A transition must simply include one additional piece of data, the voltage itself. One additional step could be taken to remove the restriction on a node's data entirely. The only constraint is the need to be JSON-serializable and parsable by the module that will be responsible for compilation of the physical hardware.

2.3 Hardware Back-End

It became apparent that decoupling the experimental front-end and the hardware-oriented back-end was crucial. In a real-world environment, unpredictable events can lead to unexpected (and potentially undocumented) equipment errors. It is important that these errors be handled appropriately to avoid crashes at the front-end. A client-server model is a standard technique designed to circumvent this problem. This project can be found on GitHub with maintained documentation [179]. Figure 2-9 schematically represents the relevant components of the ModuleServer.

2.3.1 Overview

The server runs as a standalone process that receives the initial client request. There are a small subset of special admin commands that the main process will respond to, primarily related to the upkeep of the currently loaded modules. The client socket is passed off to a subprocess (the "worker") using a multiprocessing queue. This worker is responsible for management of the module requested by the client, and is tasked to fulfill the rest of the client's request.

A module consists of user code that represents an abstract piece of equipment. The user code contains a class with relevant methods to control and interact with the physical hardware. This can be executed over TCP, serial, shared libraries, etc., the choice of which is left entirely to the user's discretion. The worker exists to sandbox and monitor this user code to ensure errors are returned to the client appropriately. If the code in a module gets modified, the worker will reload the module when it is not actively busy with a client to ensure the minimization of downtime between code

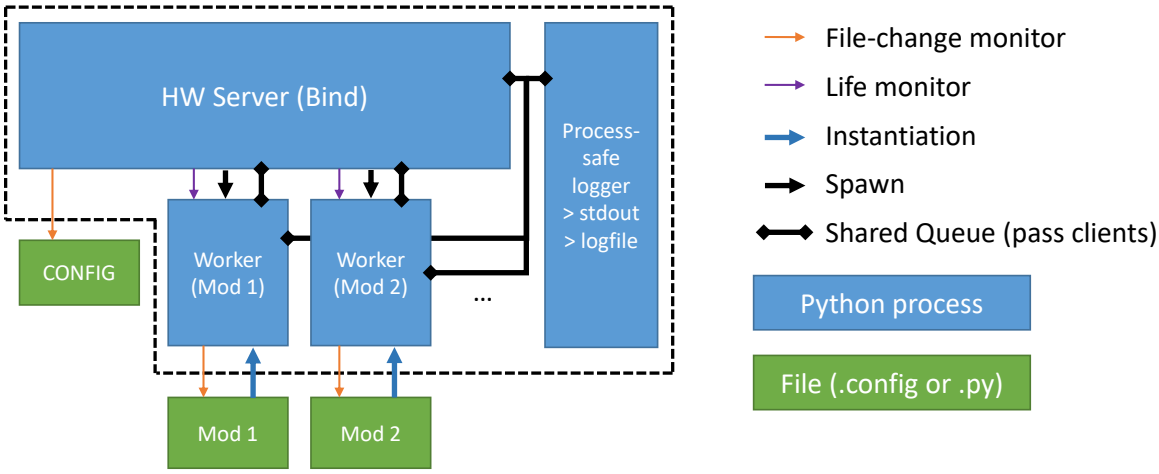

Figure 2-9: **ModuleServer Schematic.** Blue rectangles represent python processes. The main process is the "HW Server" which is responsible for spawning all other sub-processes, constructing queues, and sharing queues. The green rectangles represent files on the filesystem that are relevant for the ModuleServer's operation. The main while-loop governing the server monitors the CONFIG file for changes when the server is not busy with a client (e.g. no request received within 1 second). If changed, it will parse the contents of the file and load/unload/reload module workers accordingly. In the same manner, and for the same reason, the workers perform the same monitoring process for their module's source code file. This enables a continuous integration and continuous development environment with no server downtime.

updates. The rationale for separating each module into a separate process can be thought of in the same context as the rationale associated with the process designed to build the ModuleServer in the first place — to ensure that errors from one module cannot influence any other parts of the system. In fact, each module is completely unaware of other loaded modules.

The server will monitor the workers to protect against fatal errors capable of crashing any of the modules. If a fatal error does occur, the server will attempt to re-spawn the worker until it is apparent that the action cannot be accomplished. In this situation, the server will directly respond to clients with the appropriate error message along with as much metadata as possible to help diagnose the issue.

The server reads a config file to know which modules to load, and will monitor that file for changes during runtime when it is not busy handling a client. It will take care of loading and unloading modules as necessary, as instructed by the updated config file.

Finally, a separate logging process runs next to all existing subprocesses. Much like the manner in which clients are passed from the main server process to workers using a queue, logs are sent from all active processes (main- and sub-) over a queue to the logging process. This acts to serialize otherwise asynchronous messages and handle them in a way that the user can configure.

2.3.2 Protocol and API

All communication streams between the server and client are terminated by a newline character `'\n'` (ASCII 10). The protocol, illustrated schematically in Figure 2-10, uses ASCII characters to stream serialized data between the server and client in the form of JSON strings. To avoid interruption in the stream caused by special characters, the JSON strings are URL-encoded (plus) which escapes any white space and special characters by replacing the content with their hexadecimal representation. The client initiates the communication by connecting to the port on the machine that the server process has binded to:

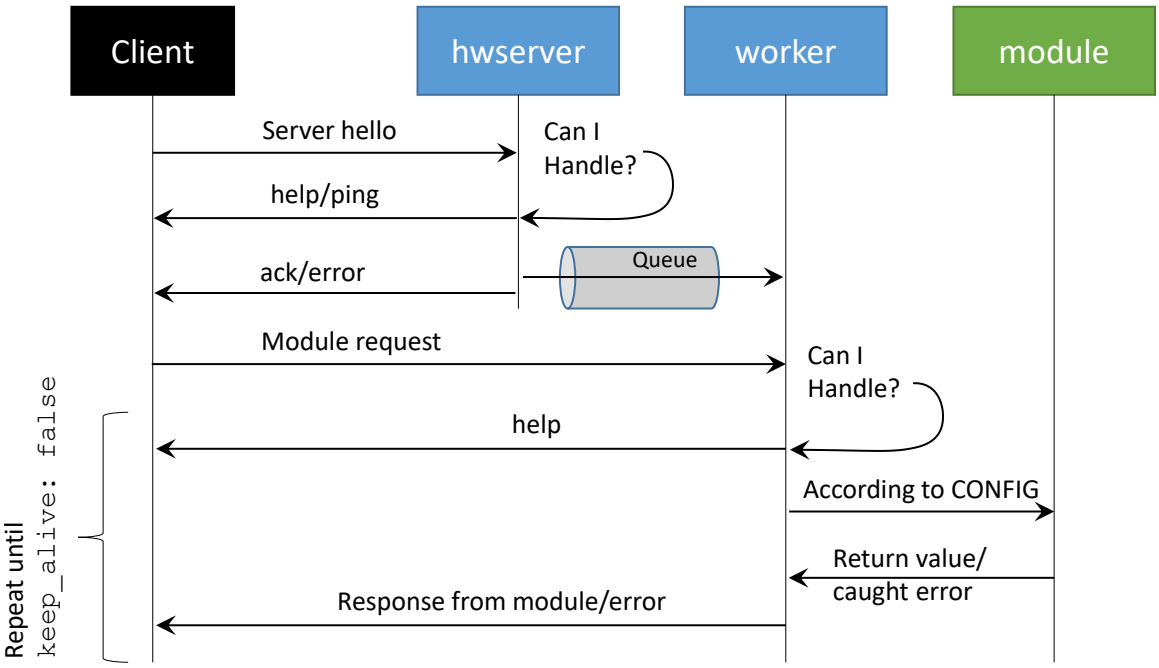

Figure 2-10: **ModuleServer Client Protocol/API.** Summary of API requests sent from the client to the server. Time progresses from left to right, and top to bottom. Everything to the right of "hwserver" (and including "hwserver") are all members of the ModuleServer stack running on one machine (potentially multiple cores). The client initiates the communication by sending the "server hello" packet. The main process on the ModuleServer will attempt to handle the request. If successful, it will reply accordingly and close the connection. If unable to handle the request directly, the request must be addressing a module, and the server will place the open client socket in a queue to the appropriate worker for further handling. After accomplishing this, the server replies to the client with an acknowledgement. At this point, the client is expected to send a follow-up packet containing the request information for the worker. The worker attempts to handle all following requests and, if necessary, will forward a request to the user's module code for fulfillment. All return values/messages are relayed back to the client, or an error is packaged in the reply instead.

```
Server hello:
{"name": <name as str>}
```

The server will send `"ack"` if successfully passed to the worker queue, or an appropriate error and traceback if the request fails before making it onto the queue. Next, the client sends a follow-up JSON string that targets the request for the worker:

```
{
  "function": <function in "name" as str>,
  "args": [<arg0 as any type>, <arg1 as any type>, ...],
  "keep_alive": <True/False>
}
```

where "any type" refers to any type that is JSON serializable by Python, which includes all Python primitives (e.g. dicts, lists, strings, ints, floats, etc.). If for some reason a type that is not JSON serializable is used, the user's module code should account for this, otherwise the server will raise an error. The general approach to solving this issue is simply finding a way to pack an object into a Python primitive and inflate it on the client side.

All aspects of the operation, including `"keep_alive"`, includes a 1 second timeout window that begins after the server sends a reply. This should be more than sufficient from a timing perspective to account for network delays, even in slow networks. Nonetheless, as with many parameters, this can be adjusted by the system administrators.

When an error in the main process or in a worker occurs, the connection socket is closed regardless of the `"keep_alive"` flag. Clients can also send a specially constructed request to disconnect from the server without requiring the server to raise its timeout exception.

```
{
  "function": None,
  "args": [],
```

```
  "keep_alive": False
}
```

The server includes a number of special commands that are processed in the core server process code before potentially calling on user code within a loaded module:

- `_help` can be called as `"name"` in the "server hello" for available modules.
- Likewise, `_help` can be called in request to workers as `"function"` fields (note it is still necessary to include other two fields even though they will be ignored).
- `_ping` (or null) can be issued as well for `"name"` which will result in an echo of the client's IP address.
- `_get_modules` as the `"name"` will return a list of module names that are loaded. If you append `.*` (e.g. `_get_modules.msquared`), only the modules that begin with `*` will be returned.
- `_reload_{URLENCODED_MODULE_NAME}` as the `"name"` can be issued to force a reload of the module specified.

The `URLENCODED_MODULE_NAME` should be the module name that has been urlencoded (plus). If no module is specified, the server will force the config file to be reloaded. This syntax is to circumvent the lack of arguments in the "server hello". The server will respond with a description of the action taken. Workers and server will send responses that are urlencoded(plus) JSON strings:

```
{
  "response": RESPONSE,
  "error": ERROR_STATUS,
  "traceback": traceback.format_exc()
}
```

Where `ERROR_STATUS` is True/False and `RESPONSE` is the JSON-encoded return value from the requested `MODULE`.

2.3.3 Configuration

Here, I would like to outline a very basic configuration to get this server setup and running. I will assume that the ModuleServer repository is somewhere on your python's path, and the following project directory structure:

```
myproject/
    server.py
    server.config
    mymodules/
        __init__.py
        moduleA.py
        moduleB.py
    logs/
        server.log
        server.log.1
        ...
        server.log.5
```

Server Setup

You can create a server.py file as follows:

```
1  import logging, os, sys
2  import ModuleServer.server as server
3
4  BASE_PATH = os.path.dirname(os.path.abspath(__file__))
5
6  LOGLEVEL = logging.INFO
7  CONFIG_PATH = os.path.join(BASE_PATH,'server.config')
8  SERVER_IP = 'localhost' # 0.0.0.0 to bind to all interfaces
9  SERVER_PORT = 36577
10 LOGFILE = os.path.join(BASE_PATH,'logs','server.log')
11
```

```
12 if __name__ == '__main__':
13     server.main('HW Server',CONFIG_PATH,SERVER_IP,SERVER_PORT,LOGLEVEL,LOGFILE)
```

Config File

This simply requires use of a JSON file that informs the server's workers how to load and dispatch requests to your module. Entries that have an underscore as the first character of the module name are ignored. The format is a dictionary with keys being the module names and values being a list: `["module import path", "class name or function entry point", "dispatch method in class or null if calling directly by client request"]`:

```
{
    "moduleA": [
        "mymodules.moduleA",
        "moduleA",
        "foo"
    ],
    "_moduleB": [
        "mymodules.moduleB",
        "bar",
        null
    ]
}
```

Modules

Modules do not have a particular required recipe. Here I offer a possible implementation to complete the example (based on the config file). moduleA.py:

```
1 import os, logging, time
2 logger = logging.getLogger(__name__)
3
```

```
class moduleA:
    def __init__(self):
        logger.debug('Here we go')
        time.sleep(3)
        logger.debug('Loaded')

    def foo(self,client_ip,fn_name,*args):
        logger.debug('Calling '+fn_name+str(args))
        return 'You successfully called the dispatching method!'
```

moduleB.py:

```
import os, logging, time
logger = logging.getLogger(__name__)

class bar:
    def fun1(self,*args):
        logger.debug('Called fun1 directly! Args: '+str(args))
        return 'No dispatching method necessary.'
```

Note that workers setup root logger properly, enabling modules to inherit and log easily at any level:

```
import logging
logger = logging.getLogger(__name__)
logger.info('testing123...')
```

Clients

Clients connect with server.py on the host machine to communicate with modules. An example illustrating the creation of a client follows. It is also worth noting that client.py uses numpy-style docstrings [114].

```
from client import client
myclient = client(host = 'localhost')
```

The relevant public methods for the client are:

- The `client.ping()` method can be issued to ping the server to get the client's IP address and binding port.

```
print(myclient.ping())
```

- The `client.com(module, funcname='_help', *args)` method can be called to communicate with a module and request it to perform a function. Here is an example of requesting `"moduleA"` to call `"foo"` with arguments `['ay', 1, False, None]`.

```
resp = myclient.com('moduleA', 'foo', 'ay', 1, False, None)
print(resp) #-> You successfully called the dispatching method!
```

- The `client.help()` method can be called to get server help text.

- The `client.get_modules(prefix='')` method will return a list of module names that are loaded. If you specify `.*` (e.g. `myclient.get_modules('msquared')`), only the modules that begin with `*` will be returned.

- The `client.reload(module)` method can be issued to force a reload of the module specified.

2.3.4 M Squared Module Example

Preparing the M Squared tools for automation presented a particular challenge because they are implemented in an early version of the application programming interface (API). Consequently, I will present the module architecture developed in an effort to adapt their API into our automation infrastructure. It is important to remember that this is by far the most complicated module in the ModuleServer due to this particular laser's API. Standard modules will reflect the examples in Section 2.3.3 more closely than they will reflect the architecture of this module.

The M Squared laser ecosystem revolves around communication with their ICE Blocs (the control unit for the laser components) over HTTP and WebSockets. The ICE Blocs for various components of the laser, specifically their core Ti:sapphire laser (SolsTiS) and an external mixing module (EMM) to bring the output into the visible spectrum, use a proprietary JSON over HTTP protocol. Control of the laser is performed in the web browser using HTTP to open a WebSocket. The ICE Blocs further connect to a TCP Server running on a machine that is connected to a supported wavemeter. This TCP Server allows the laser to access a wavemeter to perform closed-loop tuning protocols. The full network topology used to control these devices can be seen in Figure 2-11b.

To control the laser remotely, the ICE Blocs allow opening of a TCP port for a preselected host from a certain IP address (configured in the web browser). To sweep the output of the SolsTiS **and/or** the EMM, you must have control of the SolsTiS to tune its resonator. However, for the EMM to operate properly, it must play the role of the *host* and be allowed to connect to the remote control point of the SolsTiS. To further complicate matters, there are not enough functions in the API associated with the EMM remote control protocol to control the SolsTiS as well. This prevents a third-party (our automation) code from controlling all aspects of the EMM output.

These issues can be resolved by implementing a "Machine-in-the-Middle" (MITM) approach. In cyber security, this is known as a man-in-the-middle attack, where a host (in this case, the "HWcomputer") pretends to be the other party. In this particular case the EMM connects to our MITM, thinking it is the SolsTiS, and the SolsTiS believes it is the EMM (although the SolsTiS does not particularly care since this is the generic API port). With this architecture, when MITM is active, the EMM is allowed to connect to the SolsTiS when necessary. When not active, our ModuleServer is allowed to connect to the SolsTiS since they reside at the same IP address. This set of connections is represented by the hollow arrows in Figure 2-11a. By giving the ModuleServer control responsibility when the MITM is running, it now has full control over the M Squared laser.

The final challenge to overcome is the implementation of an approach that al-

lows the SolsTiS to communicate with the wavemeter. In principle, the TCP Server that arrives with the SolsTiS can load its own version of the dynamic-link library (DLL) responsible for communicating with the wavemeter. However, this particular wavemeter services multiple (up to 8 lasers in our case) and various clients (experiments around the lab) that depend on uninterrupted access to the wavemeter through the ModuleServer. The internals of the original TCP Server overwrite all settings in the wavemeter app for channels not used by the M Squared devices. Furthermore, TCP Server operates the wavemeter's channels in a way that excludes all channels not in use by the M Squared laser. Obviously, this is problematic for use-case. As such, with a little packet-sniffing between the SolsTiS and TCP Server, the protocol can be reverse engineered and my own implementation of the TCP Server that modifies only the components of the wavemeter app necessary for the M Squared's operation can be built and integrated nicely with the existing ModuleServer API.

The architecture of the code responsible for this can be seen in Figure 2-11c. Here, a more detailed view of the module structure introduced in Figure 2-9 can be seen. The general concept behind the structure is that a client connects and sends a request to a general dispatch method in LaserWrapper. Based on the request, LaserWrapper will instantiate either the SolsTiS or EMM to fulfill the request. Upon instantiation, the EMM class will spawn the MITM program to allow the EMM ICE Bloc to communicate with the SolsTiS ICE Bloc.

2.4 Microwave Delivery

Two hardware components that are necessary for emitter creation and characterization are an ultra-high vacuum annealing furnace [35] and a microwave (MW) delivery system that will work over an entire chip-scale experiment. The physical construction of the furnace was completed as part of my S.M. Degree program [177]. Since then, I have integrated annealing recipes, as well as sufficient diagnostic data to detect problematic furnace runs, into the lab framework (described in section 2).

With regard to MW delivery, following exploration of multiple strategies to create

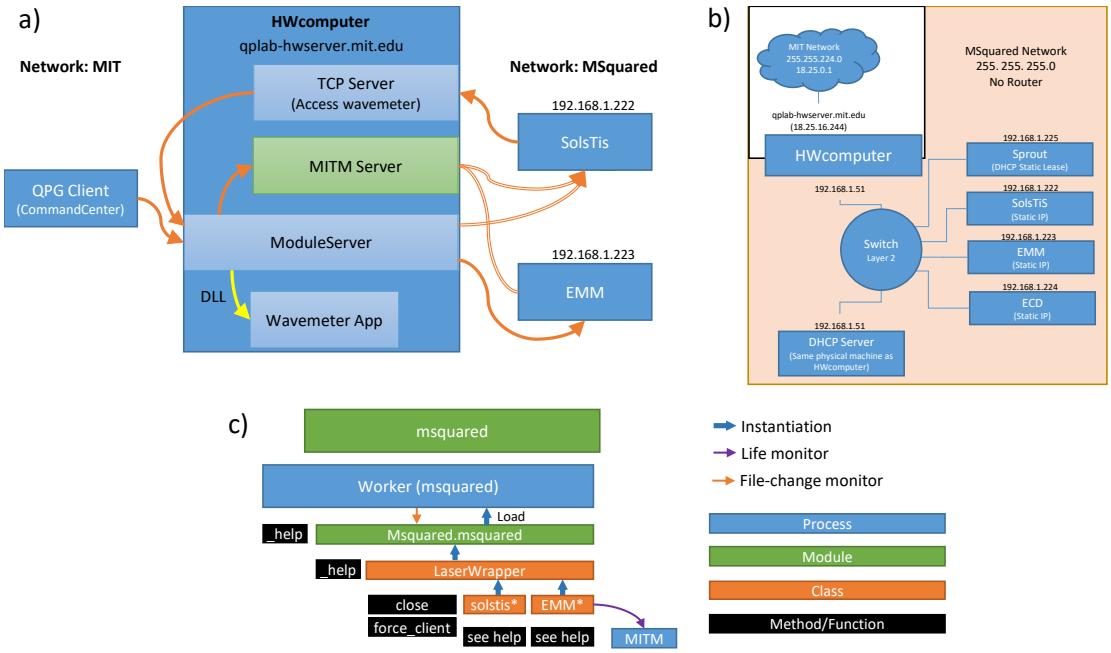

Figure 2-11: **Module Server: M Squared Laser Configuration. a)** The processes running within the "HWcomputer" that facilitate control of the M Squared devices setup. A TCP Server (named after the program the M Squared company supplies) is the binding application for the M Squared's ICE Blocs. The protocol between this program and the ICE Blocs is reverse-engineered from the company's version. Instead of directly loading the Wavemeter App through the DLL, the re-engineered version connects through the ModuleServer's interface. The ModuleServer will spawn a "Machine-in-the-Middle" (MITM) program that completes the connection between two ICE Blocs when necessary, thus acting as a switch between the ModuleServer's connection and the EMM's connection to the SolsTiS. **b)** The network topology responsible for connecting all relevant components of the M Squared infrastructure. This network is kept behind a strong firewall imposed by the HWcomputer due to security vulnerabilities in the ICE Bloc's web interface. **c)** The "msquared" module code structure that fits into the ModuleServer (see Figure 2-9).

a homogeneous field across the sample, a strategy that ensures a uniform field across the field-of-view of the imaging system and is static relative to that field-of-view was selected. Figure 2-12 illustrates the design and modeling of such a delivery system that integrates a 50 Ω strip-line transmission line to a loop around the final lens of the objective nearest the sample. By cutting notches into the metal housing (1-2 are sufficient for operation at 2.87 GHz) of the objective, the current induced by inductive coupling (i.e., an image current) can be prevented. This approach improves the field magnitude by a factor of about 2.33. The construction of such a system was further optimized by moving the loop as close to the focal plane of the objective as possible without contacting the sample. The version finally implemented was designed by Ian Christen (Quantum Photonics Lab) on a flexible PCB.

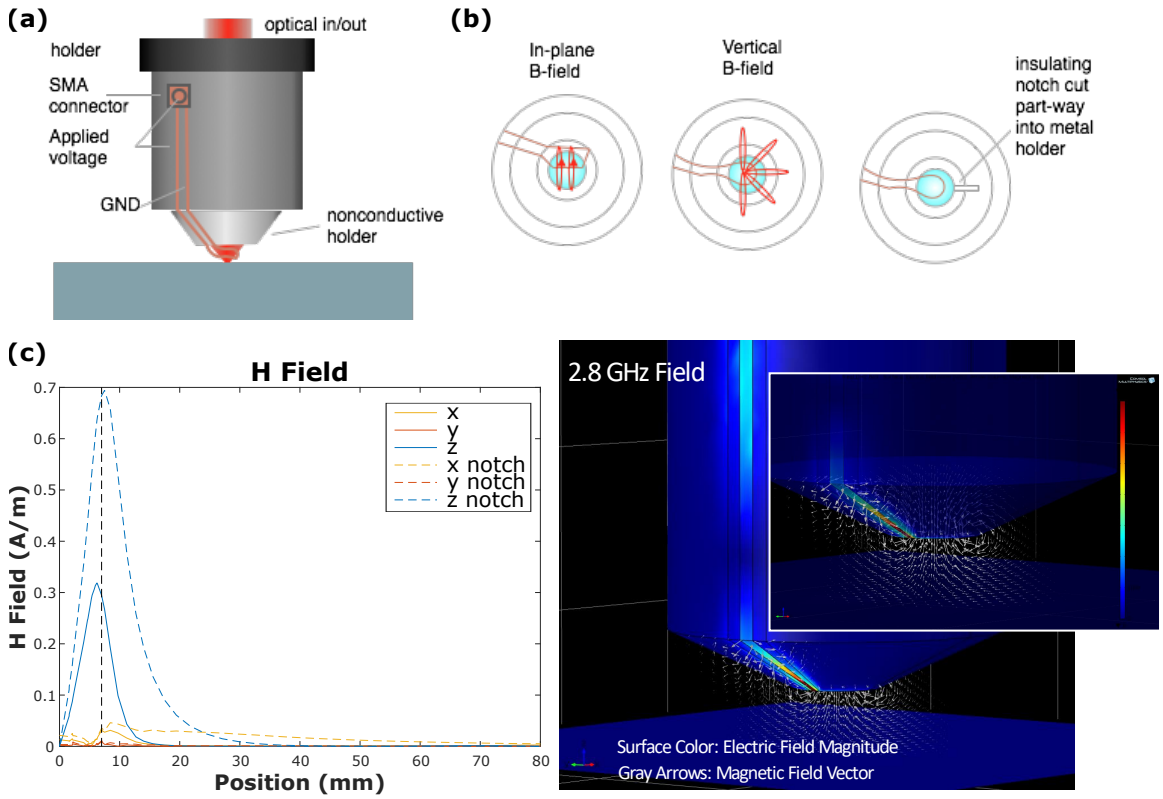

Figure 2-12: **Free-Space Microwave Delivery.** **(a)** The general design of the microwave objective in schematic form. A coaxial connector (SMA, SMP, etc.) is attached to the housing of a microscope objective, connecting to signal and ground wires. These wires (impedance matched to 50 Ω on the metal casing) run down to the tip of the objective, where they form a loop. The bottommost mount of the objective can be of a non-conductive material, such as ceramic. Alternatively, it could have a notch cut into it to produce an open circuit in the ring, preventing the induction of a cancelling current. **(b)** The loop can exhibit different geometries to achieve different magnetic fields at the sample focal plane. The in-plane geometry would produce a perpendicular magnetic field at the center of the field of view, whereas the out-of-plane loop geometry would produce a strong in-plane magnetic field component. Instead of a single turn, the loop could have N turns to magnify the applied magnetic field by approximately N times. **(c)** Modeling the device. (Left) The magnitude of magnetic field components along the optical axis of an objective with and without a "notch" design. The notch increases the field strength in the geometry by a factor of about 2.33. (Right) Geometry of the microscope objective (main cylinder with cone at the bottom) with a differential stripline source leading to a notch-protected conductive loop at the base to generate the magnetic field (electric field magnitude colored) at the sample (gray arrows). The notch prevents an image current forming in the objective casing which would lead to a reduced magnetic field. The blue surface at the very bottom of the image is the sample/focus plane.

Chapter 3

Silicon-Vacancy Centers

The controlled creation of defect center—nanocavity systems is one of the outstanding challenges facing the quantum science community in the effort to efficiently interface spin quantum memories with photons for photon-based entanglement operations in a quantum network. Here, we demonstrate the direct, maskless creation of atom-like single silicon-vacancy (SiV) centers in diamond nanostructures via focused ion beam implantation with $\sim$32 nm lateral precision and $<$50 nm positioning accuracy relative to a nanocavity. We determine the Si+ ion to SiV center conversion yield to be $\sim$2.5% and observe a 10-fold conversion yield increase after additional electron irradiation. Low-temperature spectroscopy reveals inhomogeneously broadened ensemble emission linewidths of $\sim$51 GHz and near lifetime-limited single-emitter transition linewidths as low as 126 ± 13 MHz, a linewidth corresponding to $\sim$1.4-times the natural linewidth. This method for the targeted generation of nearly transform-limited quantum emitters should facilitate the development of scalable solid-state quantum information processors.

In this chapter, portions of our paper entitled, "Scalable focused ion beam creation of nearly lifetime-limited single quantum emitters in diamond nanostructures" and its corresponding supplementary material [148] are revisited.

A central goal in semiconductor quantum optics is to devise efficient interfaces between photons and atom-like quantum emitters for applications including quantum memories, single photon sources, and nonlinearities at the level of single quanta. Many

efforts to optimally position emitters relative to the mode maximum of nanaphotonic devices with the necessary sub-wavelength-scale precision have been investigated, including fabrication of nanostructures around prelocalized or site-controlled semiconductor quantum dots (QDs) [11, 144, 145, 25, 163] or diamond defect centers [133], or implantation of ions for defect center creation in nanostructures concomitant with the nanofabrication [146, 149]. However, these approaches do not allow the high-throughput post-fabrication creation of quantum emitters with nearly indistinguishable emission in nanophotonic structures already fabricated and evaluated; the approach implemented here greatly simplifies the design and fabrication process and improves the yield of coupled emitter-nanostructure systems.

Unlike quantum emitters such as molecules or quantum dots, diamond defect centers can be created through ion implantation and subsequent annealing [98, 129], enabling direct control of the center depth via the ion energy. Lateral control has been demonstrated through the use of nanofabricated implantation masks [105, 169, 125, 159, 124, 15], which have been employed for color center creation relative to optical structures through atomic force microscopy (AFM) mask alignment [133], and combined implantation/nanostructure masking [146, 149]. Implantation through a pierced AFM tip [133] does not require modification of the fabrication process and allows for implantation after fabrication and evaluation of these structures. However, the process is time-consuming, requires special AFM tips, and can lead to reduced positioning precision by collisions with mask walls. As an alternative, focused ion beam (FIB) implantation of ions, for example nitrogen [85] and silicon [166], can greatly simplify the implantation process by eliminating the need for a nanofabricated mask. Similar to a scanning electron microscope, an ion beam can be precisely scanned, enabling lateral positioning accuracy at the nanometer scale and 'direct writing' into tens of thousands of structures with high throughput.

The SiV belongs to a group of color centers in diamond that has emerged as promising single photon emitters and spin-based quantum memories. Among the many diamond-based fluorescent defects that have been investigated [6], the silicon-vacancy (SiV) center [184, 112, 111, 110] is exceptional in generating nearly lifetime-

limited photons with a high Debye-Waller factor of 0.79 [38] and low spectral diffusion due to a vanishing permanent electric dipole moment in an unstrained lattice [154, 69]. These favorable optical properties have notably enabled two-photon quantum interference between distant SiV centers [154, 138] and entanglement of two SiV centers coupled to the same waveguide [153]. In addition, the SiV has electronic and nuclear spin degrees of freedom that could enable long-lived, optically-accessible quantum memories [104, 126, 139].

Here, a method for positioning emitters relative to the mode maximum of nanophotonic devices is introduced: direct FIB implantation of Si ions into diamond photonic structures. This post-fabrication approach to quantum emitter generation achieves nanometer-scale positioning accuracy and creates SiV centers with optical transition linewidths comparable to the best 'naturally' growth-incorporated SiV reported [138]. The approach allows Si implantation into $\sim 2 \cdot 10^4$ sites/s, which allows creation of millions of emitters across a wafer-scale sample. We also show that additional post-implantation electron irradiation and annealing creates an order of magnitude enhancement in Si to SiV conversion yield. By repeated cycles of Si implantation and optical characterization, this approach promises nanostructures with precisely one SiV emitter per desired location. Finally, we demonstrate and evaluate the site-targeted creation of SiVs in prefabricated diamond photonic crystal nanocavities. The ability to implant quantum emitters with high spatial resolution and yield opens the door to the reliable fabrication of efficient light-matter interfaces based on semiconductor defects coupled to nanophotonic devices.

3.1 SiV Creation and Sample Preparation

Focused ion implantation was performed at the Ion Beam Laboratory at Sandia National Laboratories using the nanoImplanter (nI). The nI is a 100 kV focused ion beam (FIB) machine (A&D FIB100nI) making use of a three-lens system designed for high mass resolution, using an ExB filter, and single ion implantation, using fast beam blanking. The ExB mass-filter (M/ ΔM of $\sim$61) separates different ionic species

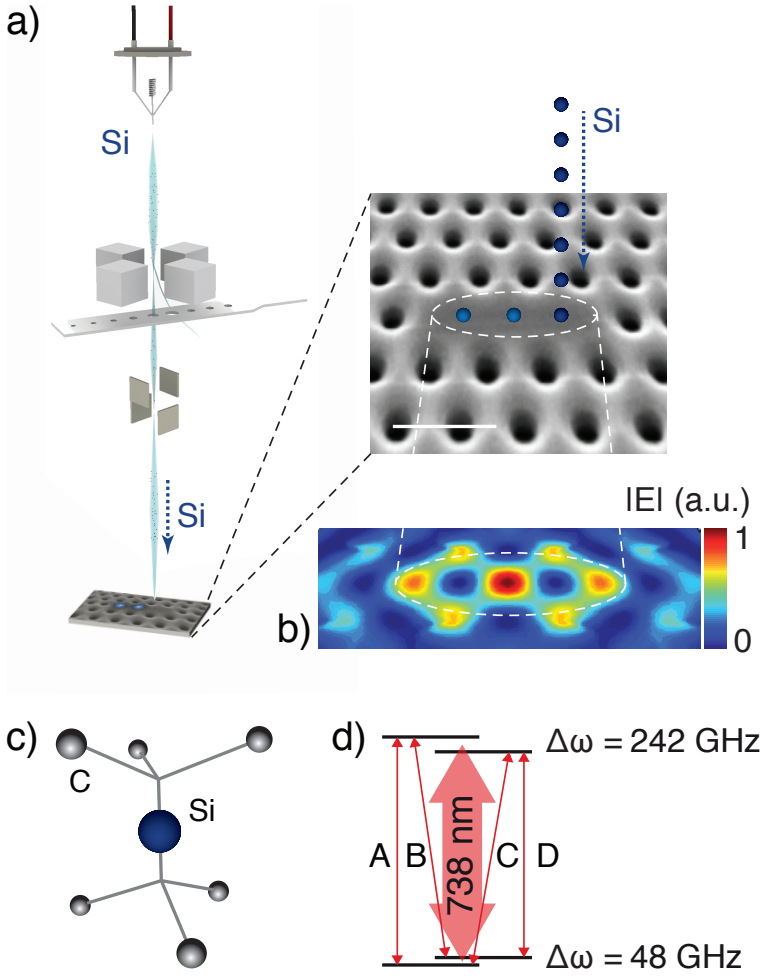

Figure 3-1: **Targeted Si Ion Implantation into Diamond and Silicon-Vacancy Defect Properties. a)** Illustration of targeted ion implantation. Si ions are precisely positioned into diamond nanostructures via a focused ion beam (FIB). The zoomed-in image is a scanning electron micrograph of an L3 photonic crystal cavity patterned into a diamond thin film. The scale bar is 500 nm, Si is silicon. **b)** Distribution of the electric field for the fundamental L3 cavity mode with three Si target positions: the three mode maxima along the center of the cavity are indicated by the dashed circle. The central mode peak is the global maximum. **c)** Atomic structure of a silicon-vacancy defect center (SiV) in diamond. Si represents an interstitial Si atom between a split vacancy along the <111> lattice orientation and C the diamond lattice carbon atoms. **d)** Simplified energy level diagram of the negatively charged SiV indicating the four main transitions A, B, C, and D [69]. $\Delta\omega$ is the energy splitting of the two levels within the doublets.

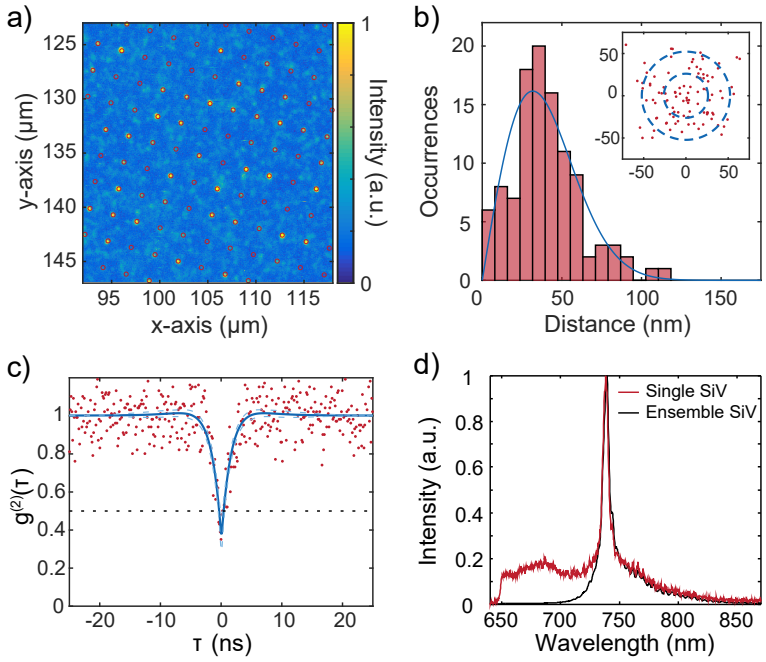

Figure 3-2: **Spatial Precision of SiV Creation. a)** Confocal scan of SiV center array. Sites are separated by 2.14 μm. Overlaid are regular grid points from an aberration-corrected reference lattice. **b)** Analysis of implantation precision. We determined the 2-d position uncertainty of the created SiV to be 40 ± 20 nm. Blue curve: fit to Rayleigh distribution. Inset: Scatter plot of created single SiV sites relative to their grid points with one and two σ guides to the eye, where the radius $\sigma = 26$ nm corresponds to the expected implantation standard deviation resulting from the combination of beam width and implant straggle. **c)** Normalized second-order autocorrelation function of a single SiV with $g^{(2)}(0) = 0.38 \pm 0.09$. Red points indicate data (without background subtraction), and the blue line is a fit to the function $1 - A \cdot exp(-|\tau/t_1|) + B \cdot exp(-|\tau/t_2|)$. The black dashed line indicates $g^{(2)}(\tau) = 0.5$ while the blue dashed lines indicate the 95% confidence intervals for the fit. **d)** Ensemble (black) and single-emitter (red) SiV room-temperature fluorescence spectra. The characteristic zero-phonon line at 737 nm is prominent.

and charge states from liquid metal alloy ion sources (LMAIS), providing the capability for implantation of ∼1/3 the periodic table over a range of energies from 10 to 200 keV. For the Si implantation discussed here, we used an AuSbSi LMAIS with typical Si beam currents ranging from 0.4 pA to 1 pA. Fast beam blanking allows direct control over the number of implanted ions. We determine the number of implanted ions by measuring the beam current and setting the pulse length to target a given number of ions per pulse. The nI is a direct write lithography platform that uses electrostatic draw deflectors, controlled by a Raith Elphy Plus pattern generator, to position the beam. Single ion positioning is limited by the beam spot size on target. With typical spot sizes ranging from 10-50 nm, we have measured the targeting accuracy to be <35 nm for 200keV Si++ beam using a series of ion beam induced charge measurements.

For targeting into nanostructures, we align the ion beam relative to the sample by registering a secondary electron image of the alignment markers generated using the ion beam to scan the sample. Shift, rotation, and magnification corrections are calculated and applied in the pattern generator control package. This allows for any location within the write field to be individually targeted for implantation.

The lithography pattern is the original design file that was used to pattern the diamond thin film via electron beam lithography (EBL) and reactive ion etching. Errors resulting from inaccuracy during EBL were not taken into account.

To create a single SiV per cavity with high probability, we implanted ∼20 Si ions per cavity mode maximum, yielding about 1.8 SiVs per cavity on average according to an extrapolated conversion efficiency of ∼3% under Poisson statistics for 160 keV Si ions (Fig. 3-3) that target the middle of membrane at 106 nm.

The sample was annealed at 1050°C under high vacuum ($< 10^{-6}$ mbar at max temperature) for two hours to form SiV centers and eliminate other vacancy-related defects. Finally, we clean the sample surface through boiling tri-acid treatment (1:1:1 nitric:perchloric:sulfuric) and subsequent dry oxidation in a 30% oxygen atmosphere at 450°C for four hours.

3.2 Experimental Setups

Here, the experimental setups used to characterize our samples at room and cryogenic temperatures is described.

3.2.1 Room-Temperature Measurement Setup

A modified fluorescence microscope (Zeiss Axio Observer), customized to allow confocal illumination at 532 nm (Coherent Verdi) and single-mode fiber fluorescence collection was used. Collected fluorescence is spectrally filtered (Thorlabs FEL0650) and detected on avalanche photodiodes (APD) with single-photon resolution (Excelitas) or spectrally resolved on a grating spectrometer (Princeton Instruments, Acton SP2500i).

3.2.2 Cryogenic Measurement Setup

These measurements were performed at 18 K in a closed cycle helium cryostat (Janis). A home-built confocal microscope collects the fluorescence with a high numerical aperture (NA) objective (Olympus UMplanfl 100x 0.95 NA) and directs the emission to either the input of a single-mode fiber connected to an APD or to a free-space spectrometer with a resolution of about 61 pm ($\sim$34 GHz) at 737 nm (Princeton Instruments, IsoPlane SCT 320).

PLE measurements were performed using a modified helium flow probe-station (Desert Cryogenics model TTTP) with a 0.95 NA microscope objective (Nikon CFI LU Plan Apo Epi 100x) inside the vacuum chamber. Details of this setup are described in Evans et al. [56].

3.3 Spatial Precision of SiV Creation

As outlined in Figure 3-2, the fabrication approach introduced here relies on Si implantation in a custom-built 100 kV FIB nanoImplanter (A&D FIB100nI) system (section 3.1) and subsequent high-temperature annealing to create SiV centers. The

nanoImplanter uses field emission to create a tightly focused ion beam down to a minimum spot size of <10 nm from a variety of liquid metal alloy ion sources (section 3.1). For the experiments described here, we used an Si beam with a typical spot size of <40 nm into commercially available high-purity chemical vapor deposition (CVD) diamond substrates (Element Six). After implantation, high-temperature annealing and surface preparation steps to convert implanted Si ions to SiVs (section 3.1) were performed.

The resulting SiV arrays were characterized at room temperature through confocal fluorescence microscopy in a home-built setup (section 3.2.1). Fig. 3-2a shows a scan of a square array of SiV implantation sites with lattice spacing of 2.14 μm across a 30×30 μm^2 write field, created via a single point exposure from the Si beam. Room-temperature spectral measurements in a dense region containing many centers (Fig 3-2d, blue curve) showed an inhomogeneous linewidth of approximately 5 nm centered around 738.3 nm, characteristic of the SiV center. We subsequently identified single SiVs through second-order correlation measurements. For instance, Fig. 3-2c shows photon antibunching for a SiV with an observed count rate of 30 kcts/s collected via an oil immersion (numerical aperture of 1.3) objective into a single-mode fiber under 20 mW of 532 nm pump power. The red line in Fig. 3-2d shows the single-emitter fluorescence spectrum at room temperature, which is very similar in shape and linewidth to the inhomogeneous spectrum. At room temperature, these lines are broadened by phonon processes and not limited by inhomogeneity between different SiV centers [74].

To determine the spatial precision of the SiV implantation, we created and imaged a square array of SiV color centers in a cryogenic setup following the procedures in section 3.1 and 3.2.1. We then fitted each SiV site with a 2D Gaussian to determine the location of the SiV centers below the diffraction limit, and considered only SiV sites with fluorescence intensities consistent with single emitters. Using these locations, we fitted a 2D grid allowing for affine transformation and found the distance between each SiV site and its nearest grid point. Finally, we binned the distances and fitted those values to a central Chi distribution with two degrees of freedom (Rayleigh

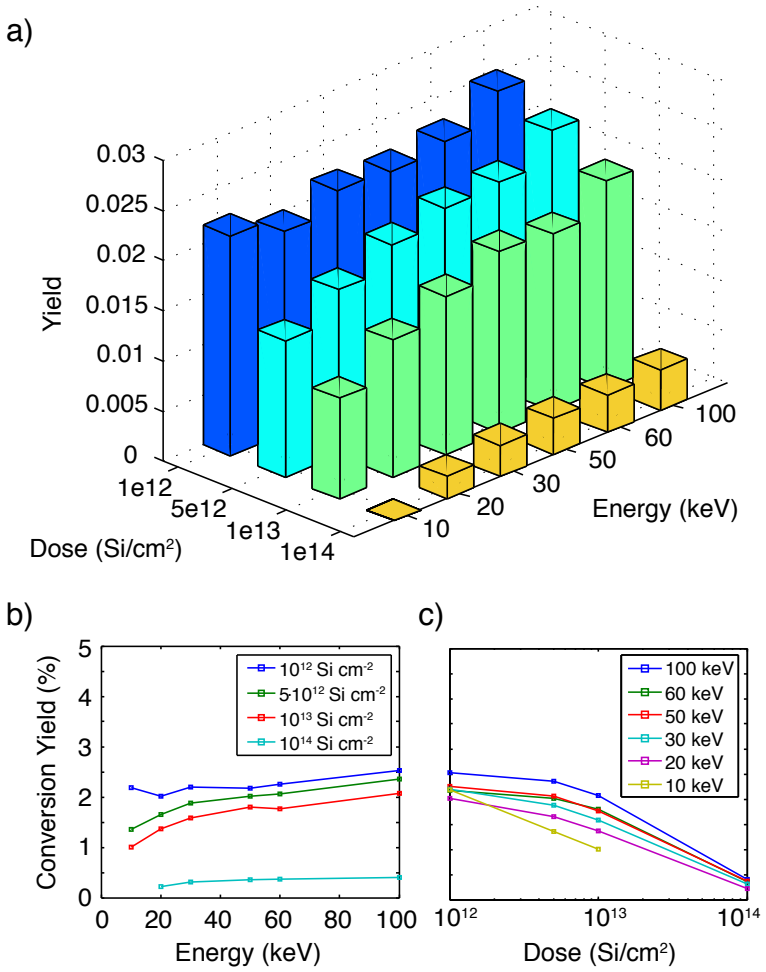

Figure 3-3: **Si Ion to SiV Conversion Yield. a)** Si to SiV conversion yield for varying implantation ion energies and doses. The conversion yield was determined by calibrating array intensities (Fig. 3-2) with the determined averaged single SiV photon count rate. Si conversion yield as function of **b)** energy and **c)** dose. The lines are guides to the eye.

distribution), which describes the distribution of the distance $R = \sqrt{X^2 + Y^2}$ where X and Y are independent zero-mean normal random variables with identical variance (Fig. 3-2b). The reported separation is the mean of the fitted Chi distribution corresponding to the mean separation in R (40 nm), and the error is the square root of the variance (20 nm). The mean separation in the X and Y directions is 0 nm with a standard deviation of 32 nm. These measured values agree well with the expected precision of 26 nm calculated by the addition in quadrature of the uncertainties arising from the nominal 40 nm FWHM beam size and 19 nm lateral implantation straggle.

3.4 Creation Yield of SiV

To determine the conversion yield of implanted Si ions to SiV centers, we swept the implantation dose logarithmically from 10^{12} to 10^{14} Si cm^{-2}, and the implantation energy linearly from 10 to 100 keV. The dose and energy determine the number and depth of vacancies created during the implantation process, with increased energy resulting in more vacancies at increased depth. The vacancy density affects the probability that a Si defect captures a diffusing vacancy and converts to SiV during annealing which is a proposed mechanism for SiV formation [47]. To estimate the yield, we measured the fluorescence intensity across a 10×10 μm^2 region of constant implantation dose and energy, and normalized to the average single-emitter intensity and implanted ion number. Fig. 3-3a summarizes the yield measurements. Yield increases as a function of energy (Fig. 3-3b), which is expected for a vacancy-limited SiV creation process, up to 2.5% for the highest-energy 100 keV ions with a dose of $\sim10^{12}$ cm^{-2}. These measurements indicated a decreasing yield as a function of dose (Fig. 3-3c). We attribute this to an accumulation of charged defects in the diamond lattice that lead to ionization, much like that observed in NV centers [151]. Alternatively, reduced yield could result from lattice damage that accumulates in the form of multi-vacancy defects as the diamond lattice approaches the graphitization threshold, a phenomenon that has been observed in similar experiments with NV centers [118].

Irradiating diamond with high energy electrons can also improve the conversion yield of vacancy-related color centers [94, 76]. Electron irradiation at high energies $>$170 keV [80] can displace carbon atoms and create additional vacancies, which allows for larger conversion efficiency of implanted ions into vacancy-related color centers. To verify these experiments with the silicon-vacancy center, we first created a reference sample by implanting four spots with silicon ions in increasing doses of 500, 2000, 5000, and 10000 ions per spot into bulk diamond with an implantation energy of 100 keV, corresponding to an implantation depth of about 68 nm. After annealing this sample at 1200°C to activate SiVs [42], a scanning confocal fluorescence image was taken by exciting these spots simultaneously with $\sim$10 mW of both 520 nm

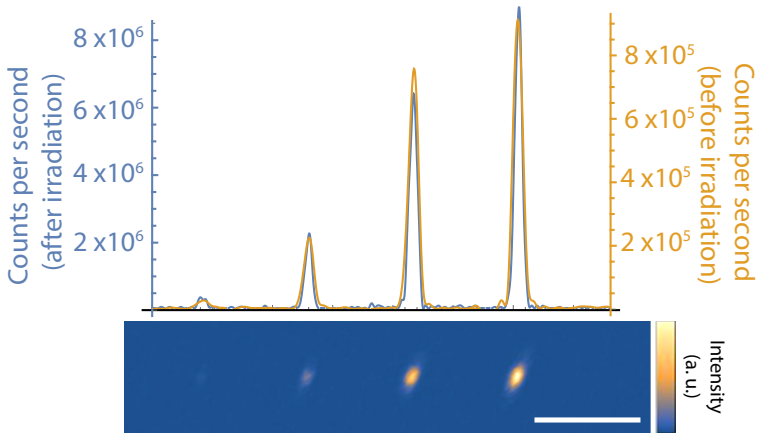

Figure 3-4: **Electron Co-implantation.** After electron irradiation and subsequent annealing we observed a 10-fold increase in fluorescence intensity at the implantation positions of Si ions (lower panel). The Si ion doses were 500, 2000, 5000, and 10000 ions per spot. The yellow line plot through the fluorescence maximum of the image indicates the intensity before electron irradiation, and the blue line after irradiation. The scale bar is 5 μm.

(Thorlabs LP520-SF15) and 700 nm (Thorlabs LP705-SF15) laser light, and collecting light into a single mode fiber through a 10 nm bandpass filter (Semrock FF01-740/13) around 737 nm (Fig. 3-4, yellow line). After this reference measurement, we irradiated the sample with 1.5 MeV electrons with a total fluence of $\sim 10^{17}$ cm^{-2}. After another annealing step, a second fluorescence image was taken with the same setup and it was verified by spectral measurements (Horiba iHR 550 with Synapse CCD) that, indeed, only the SiV typical peak at 737 nm was detected. In the second measurement, we observed increased fluorescence for all four spots by a factor of $\sim$10 (Fig. 3-4, blue line), corresponding to a final conversion yield of $\sim$20%. This result is consistent with previous observations in Si-doped diamond samples [47], supporting our interpretation that the conversion efficiency of focused ion beam implantation is limited by the vacancy density in the diamond.

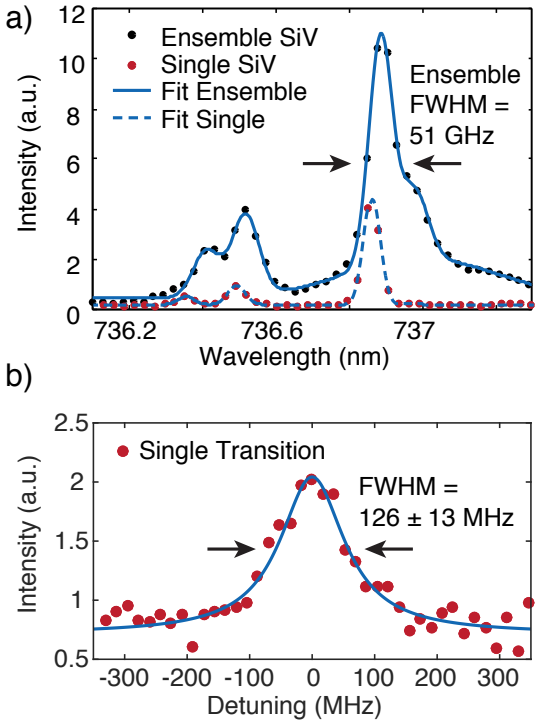

Figure 3-5: **Optical Linewidth and Coherence Properties of SiV. a)** Cryogenic spectra (< 13 K) of a single SiV (red circles) and an ensemble (black circles). The four SiV transitions (Fig. 3-1) as well as the phonon sideband are each fitted with a Gaussian function. The single SiV linewidths are spectrometer limited (FWHM $=\sim 34$ GHz). For the ensemble, an inhomogeneous broadening as low as $\sim$51 GHz (FWHM) was determined. The wavelength values are slightly blue-shifted due to an offset relative to an absolute wavelength reference by about 0.1 nm. **b)** Cryogenic (4 K) photoluminescence excitation measurement of the narrowest observed single SiV transition with a linewidth of 126 ± 13 MHz (FWHM, error estimation: 95% confidence interval) determined with a Lorentzian fit function. This linewidth of an implanted SiV is equal, within error, to the narrowest natural SiV linewidth measured to date.

3.5 Optical and Coherence Properties of SiV at Cryogenic Temperatures

I next describe the implanted SiV centers' low-temperature spectral properties. Photoluminescence spectral measurements were performed in a cryogenic home-built confocal cryostat setup (section 3.2.2). The inhomogeneous distribution of SiV transitions is plotted in Fig. 3-5a with a full width at half maximum (FWHM) of about 0.642 nm ($\sim$51 GHz). We then performed PLE measurements to determine the linewidths of individual SiVs below the spectrometer limit (section 3.2.2). We determined an average single-emitter transition linewidth of 200$\pm$15 MHz from a sample of 10 SiV implanted at 100 keV with individually resolvable transitions. The narrowest observed transition, shown in Fig. 3-5b, had a linewidth of 126$\pm$13 MHz, which is within a factor of 1.4 of the lifetime limit $\gamma = (2\pi \cdot 1.7 \text{ ns})^{-1} = 94$ MHz for a typical fluorescence lifetime of 1.7 ns [154], and equivalent to the narrowest lines observed in natural SiVs to date [138, 56].

3.6 Direct SiV Creation in an Optical Nanocavity

Finally, we demonstrated the targeted implantation and subsequent creation of SiV centers inside diamond nanostructures. We first fabricated 2D photonic crystal nanocavities into a $\sim$200 nm thick diamond membrane through oxygen reactive ion etching [88, 87]. We then used the FIB system to target Si ions into the mode maxima of the photonic crystal cavities. In the case of L3 cavities, we targeted the three mode maxima individually (Fig. 3-1b). The Si ion beam was aligned to the cavity through secondary-electron imaging of prefabricated alignment markers on the sample (Fig. 3-6b, section 3.1). We targeted the cavity mode maxima with 160 keV ions for an average of 1.8 SiVs per cavity (section 3.1). After performing the processing steps described in section 3.1 we observed about one SiV per cavity implantation spot with spectrometer-limited ($<$34 GHz) ZPL linewidths.

To determine the positioning accuracy of the cavity-targeted SiV creation, we per-

formed a spectrally resolved photoluminescence confocal scan at room temperature. At each pixel of a 2-dimensional (2D) 532 nm laser scan, a spectrum was recorded and the intensity for different spectral positions was determined. For each wavelength, we then plotted its 2D-intensity map as in Fig. 3-6 d,e. This measurement allows comparison between the photonic crystal location, determined by Raman scattering of the 532 nm laser pump from the diamond (572.52 nm) which is present in the cavity region but not in the surrounding air holes, and the SiV location determined from the emitted fluorescence (at 736.98 nm). By fitting the measured emission patterns to 2D Gaussians, we estimate a relative positioning accuracy of 48(21) nm. The error is estimated from the 68% fitting confidence interval which corresponds to one standard deviation.

3.7 Outlook

While we have demonstrated targeted creation of high-quality SiVs through FIB, several opportunities for improvement have been identified for potential future work in this area. The stochastic nature of the SiV creation process, characterized by a mean yield of η, prevents the generation of exactly one emitter with high yield [103]. One solution is to implant a low dose of Si ions (to create $\ll 1$ SiV on average) and optically verify creation of a SiV after annealing. Because implantation sites can be selected individually, the FIB process allows for repeated low-yield implantation steps that are conditionally discontinued following the creation of the desired number of emitters thus achieving sub-poissonian implantation across a sample. An alternative approach to precisely create one quantum emitter is to implant only one ion at a time, as was recently demonstrated [4], combined with electron irradiation or co-implantation of other ion species to create vacancies [151] to drive the SiV conversion yield to unity.

The linewidths of the SiVs were measured in areas with 2.5 SiVs on average, distributed within $\sim$55.4 nm (FWHM) diameter, corresponding to an implantation dose of $\sim 10^{12}$ cm^{-2}, indicating that high densities of implanted SiVs are not detrimental

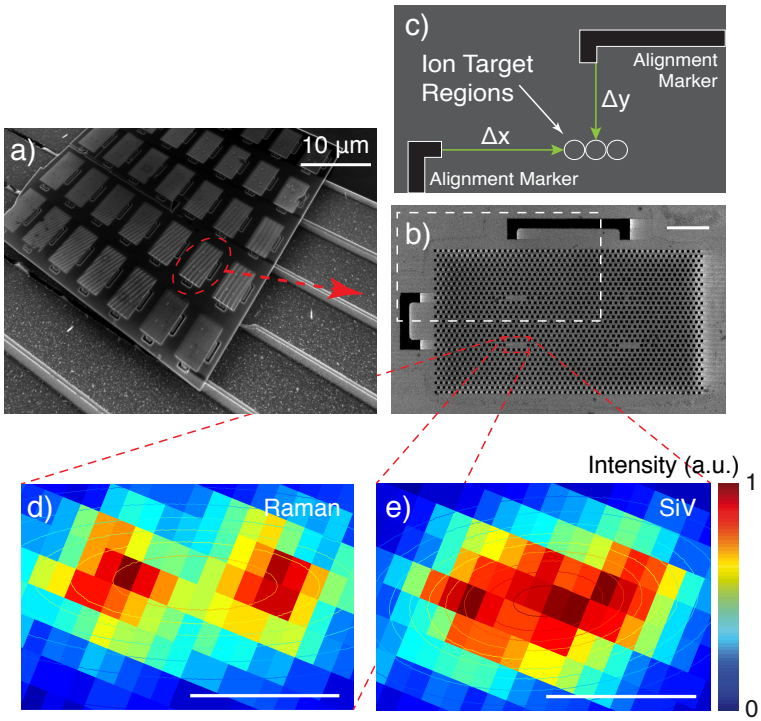

Figure 3-6: **SiV Creation in a Photonic Nanocavity. a)** SEM of example photonic crystal cavity sample. The scale bar is 10 µm. **b)** Close-up SEM of example photonic crystal lattice with four cavities. The white dashed rectangle indicates the area illustrated in **c)**. The scale bar is 2 µm. **c)** Illustration of targeting relative to alignment markers (black) with an ion spot size down to <40 nm. The white circles (not to scale for visibility) indicate the three L3 cavity mode maxima (Fig. 3-1). To determine the SiV positioning accuracy relative to the mode maxima, we performed spectrally resolved fluorescence scans. At each pixel in **d,e)** we recorded a spectrum including the Raman signal **d)**, the SiV fluorescence **e)**, and the cavity resonances (not displayed). **d)** Intensity x-y plot of the diamond Raman signal at 572.8 nm. **e)** Intensity x-y plot of SiV emission at 736.9 nm. By fitting a 2D Gaussian function to the intensity distribution, we determined the distance between the center of the cavity and the SiV fluorescence, the effective positioning accuracy, to 48(21) nm, with error estimation of one standard deviation. The scale bar in **d)** and **e)** is 0.5 µm.

to their optical properties. Although we found that FIB-implanted SiVs are similar in homogeneous transition linewidth to 'natural', as-grown centers, the inhomogeneous linewidth of ∼51 GHz (after 1050°C annealing) is slightly broader than the ∼15 GHz demonstrated for a similar SiV creation method using annealing temperatures around 1200°C [56]. Potential causes include di-vacancy breakdown caused by higher temperatures, or near-surface strain and defects in the diamond due to polishing, which can be reduced by etching the damaged layer before implantation [36].

In summary, SiV creation with high spatial accuracy by FIB implantation of Si ions into bulk and nanostructured diamond has been demonstrated. The SiV positioning accuracy relative to the targeted nanocavity mode maximum was 48 ± 21 nm, which is sufficiently precise to locate the SiV within ∼90% of the mode-field intensity maximum of nanocavities or waveguides. We also demonstrated that the SiV creation yield can be increased after implantation by a factor of 10 fold, resulting in up to 20% yield. The targeted implantation technique demonstrated here likely applies to other quantum emitters like the germanium defect center in diamond [73] and other materials of interest, such as silicon carbide [90] or molybdenum disulfide; this would be particularly advantageous for materials in which traditional nanofabricated masking is challenging.

The ZPLs of SiVs created by our method have optical linewidths within a factor of 1.4 of the lifetime limit, making them as narrow as naturally occurring SiVs described to date. Considering both this narrow linewidth and the narrow inhomogeneous distribution of implanted SiV of ∼51 GHz, this fabrication method represents a significant step towards the high-yield generation of thousands to millions of efficiently waveguide-coupled indistinguishable single photon sources. Such arrays of atom-like quantum emitters would be of great utility for a range of proposed quantum technologies, including quantum networks and modular quantum computing [19, 109], linear optics quantum computing [81, 89], all-photonic quantum repeaters [9, 121], and photonic Boson sampling [29].

Chapter 4

Multi-Qubit Registers

Medium-scale ensembles of coupled qubits offer a platform for near-term quantum technologies including computing [127], quantum sensing [46], and the study of mesoscopic quantum systems [189, 34, 99]. Atom-like emitters in solids [63] have emerged as promising quantum memories, with demonstrations of spin-spin entanglement by optical [71] and magnetic [53] interactions. Magnetic coupling in particular is attractive for efficient and deterministic entanglement gates, but raises the problem of addressing individual spins at the necessary nanometer-scale separation. Current super-resolution techniques [31, 77] can achieve this degree of resolution, but are destructive to the states of nearby qubits. Here, we measure individual qubit states in a sub-diffraction cluster by selectively exciting spectrally distinguishable nitrogen-vacancy (NV) centers [52]. We demonstrate super-resolution localization of single centers with nanometer spatial resolution, as well as individual control and readout of spin populations. This approach opens the door to high-speed control and measurement of qubit registers in mesoscopic spin clusters, with applications ranging from quantum-enhanced measurements [167] to error-corrected qubit registers [175, 40] to multiplexed quantum repeater nodes [152, 174].

In this Chapter, portions of our paper on the "Individual control and readout of qubits in a sub-diffraction volume" and its corresponding supplementary material [23] are replicated. I would also like to note that Eric Bersin contributed to the work described in this phase of the project.

Major advances towards larger coherent spin systems have recently been made by controlling nuclear spins [3] or dark electron spins [140] through one NV center and by coupling electron spins of two NV centers [53]. These advances suggest that a system of strongly coupled color centers, each coupled to proximal dark spins, could provide a scalable platform for controlled spin-spin interactions, as illustrated in Figure 4-1a.

A central challenge for coherent control of such multi-spin systems is the ability to measure individual NV centers without collapsing the states of nearby NVs. Here we address this problem by making use of the inhomogeneous distribution of NV center optical transitions attributed to natural and defect-induced lattice strain [21, 155]. The strain field $\vec{\sigma}$ enters the Hamiltonian as $H_{\text{strain}} = \vec{\sigma} \cdot \vec{V}$ [50] and can be divided into axial and transverse components, with differing effects detailed in Figure 4-1b. We find that this distribution persists even for closely-spaced NV centers, allowing us to optically address individual emitters within a diffraction-limited volume.

4.1 Nitrogen-Vacancy Strain Hamiltonian

As derived by group theory [50, 95], the strain field contribution to the NV excited state Hamiltonian can be written in the basis of the NV excited states $\{E_1, E_2, E_x, E_y, A_1, A_2\}$:

$$H_{\text{str}} = \begin{pmatrix} \sigma_z & 0 & 0 & 0 & -\sigma_y & -\sigma_x \\ 0 & \sigma_z & 0 & 0 & \sigma_x & -\sigma_y \\ 0 & 0 & \sigma_z + \sigma_x & -\sigma_y & 0 & 0 \\ 0 & 0 & -\sigma_y & \sigma_z - \sigma_x & 0 & 0 \\ -\sigma_y & \sigma_x & 0 & 0 & \sigma_z & 0 \\ -\sigma_x & -\sigma_y & 0 & 0 & 0 & \sigma_z \end{pmatrix} \tag{4.1}$$

The axial strain component σ_z provides a simple uniform shift to all levels. While this does not affect the character of the levels, it can split nearby NVs experiencing differential axial strains. This is significant in our application, as an axial strain gradient would thus allow distinguishable NVs without the often associated spin mixing

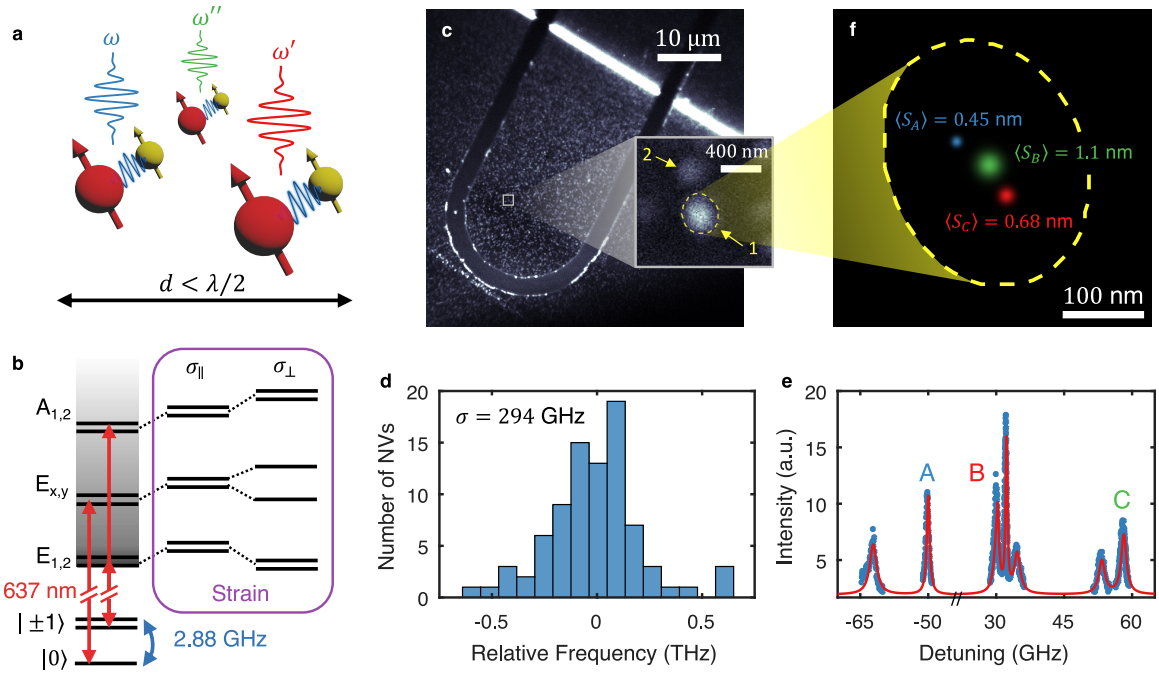

Figure 4-1: **Preferential Excitation and Imaging of Sub-diffraction Defects.** **a**, An ensemble of NV electron spins (red) coupled to nearby nuclear spins (yellow) with distinct optical transition frequencies due to local strain fields, allowing selective interaction with individual centers operating on different frequency channels within a diffraction-limited spot. **b**, NV electron level structure. A ground state spin triplet acts as a qubit, addressable via 2.88 GHz microwave driving (blue). The spin-conserving radiative transitions (red) are at distinct frequencies, allowing optical spin readout via resonant excitation. Axial ($\sigma_\parallel$) and transverse ($\sigma_\perp$) strains shift these levels further and may distinguish individual NVs. **c**, Confocal microscope image of the polycrystalline diamond (PCD) showing the microwave stripline. The bright white line is a grain boundary in the diamond. Inset, a close-up scan showing a brighter spot at site 1, determined to be a cluster of NVs, as well as a dimmer spot at site 2, determined to be a single NV. **d**, Histogram (N=87) showing the inhomogeneous distribution of ZPL transitions in the PCD, with a standard deviation $\sigma = 294$ GHz. **e**, PLE on the NV cluster at site 1, showing multiple transitions from strain-split centers. **f**, Reconstructed locations within the cluster, with width (standard deviation) indicating the standard distance error on each point, multiplied 10x for visibility. For comparison, the dashed line shows the full-width at half-maximum size of the spot under 532 nm excitation.

and coherence time degradation expected from higher strain samples.

The transverse component both splits (raising the levels A_1, A_2, E_y and lowering the levels E_1, E_2, E_x) and mixes (E_1 with $\{A_1, A_2\}$, E_2 with $\{A_1, A_2\}$, and E_x with E_y) the excited state manifold, resulting in two diverging spin triplet branches in the high strain limit.

4.2 Experimental Setup

Experiments were performed using a home-built scanning confocal microscope. The samples were cooled to 4 K using a closed-cycle helium cryostat (Montana Instruments) and were imaged through a 0.9 NA vacuum objective. 532 nm light was generated by a Coherent Verdi G5 laser, and resonant red light tunable around 637 nm was generated by a New Focus Velocity tunable diode laser. Microwave signals were generated by Rohde & Schwarz SMIQ06B and SMV03 signal generators and sent through a high-power amplifier (Mini-Circuits ZHL-16W-43+) before delivery to the sample.

4.2.1 Sample Preparation

Super-resolution localization and individual control experiments were performed on a Type IIa PCD by chemical vapor deposition (Element Six), with a native nitrogen concentration of $<$50 ppb. To increase the prevalence of sub-diffraction clusters, the sample was implanted with nitrogen at 85 keV with a density of 10^{10} cm^{-2}, and subsequently annealed at 1200 °C for 8 hours to heal the lattice and facilitate the formation of NV centers. The conversion yield of this process is on the order of 1%, resulting in a final areal NV density of roughly 1 µm^{-2}. To efficiently deliver microwaves to the sample, we fabricate gold striplines on the surface of the diamond using the following protocol:

1. Solvent clean, sonicating the sample in acetone, methanol, isopropyl alcohol (IPA), and water for 5 minutes each.

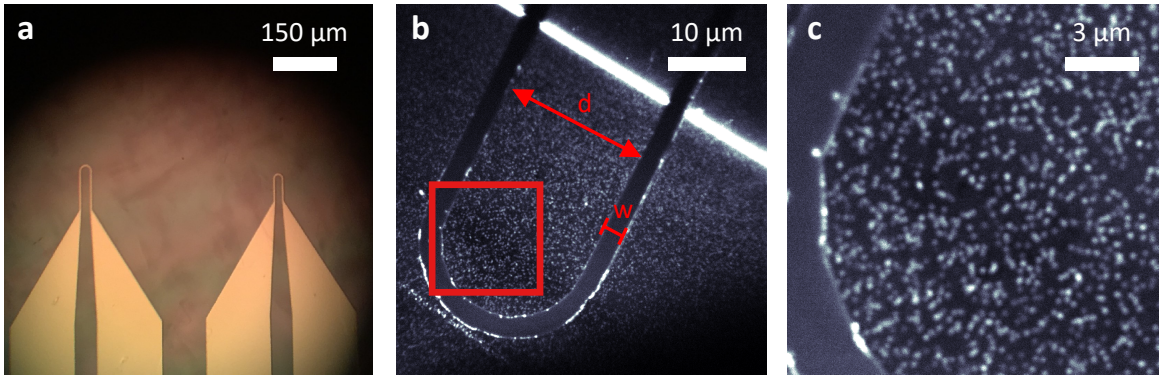

Figure 4-2: **Striplines for Microwave Delivery.** **a**, Microscope camera image of striplines post-fabrication. **b**, Confocal image of a stripline on the PCD. The bright white line is a grain boundary in the diamond. The red box corresponds to the area scanned in **c**. For this stripline, $w = 5$ µm and $d = 30$ µm. **c**, A close-up of the red boxed area in **b**; this was the region used for the experiments.

2. Oxygen plasma clean at 100 W for 5 minutes.

3. Spin-coat ZEP resist at 6 kRPM.

4. Write electron-beam patterns at 2 nA current, with a dose of 640 µC cm^{-2}.

5. Develop in ortho-xylene at room temperature for 10 seconds.

6. Deposit 5 nm of chrome for adhesion, followed by 100 nm of gold.

7. Sit overnight in N-Methyl-2-pyrrolidone (NMP) at room temperature.

8. Remove any remaining resist with sonication in NMP.

9. Clean with IPA.

The stripline is a simple loop with ends that taper out to large bonding pads. Figure 4-2a shows a camera image of two of these striplines post-fabrication. Figure 4-2b shows a confocal scan (532 nm) of the stripline used for these experiments, with a wire width of $w = 5$ µm and loop gap of $d = 30$ µm. Figure 4-2c is a close-up of the red boxed region of Figure 4-2b, showing a defect density that exhibits both clear single NVs and occasionally brighter clusters.

We perform wide-field spin echo measurements on a 25×25 µm^2 region of the PCD to characterize mean spin coherence time. Due to the randomized lattice orientation

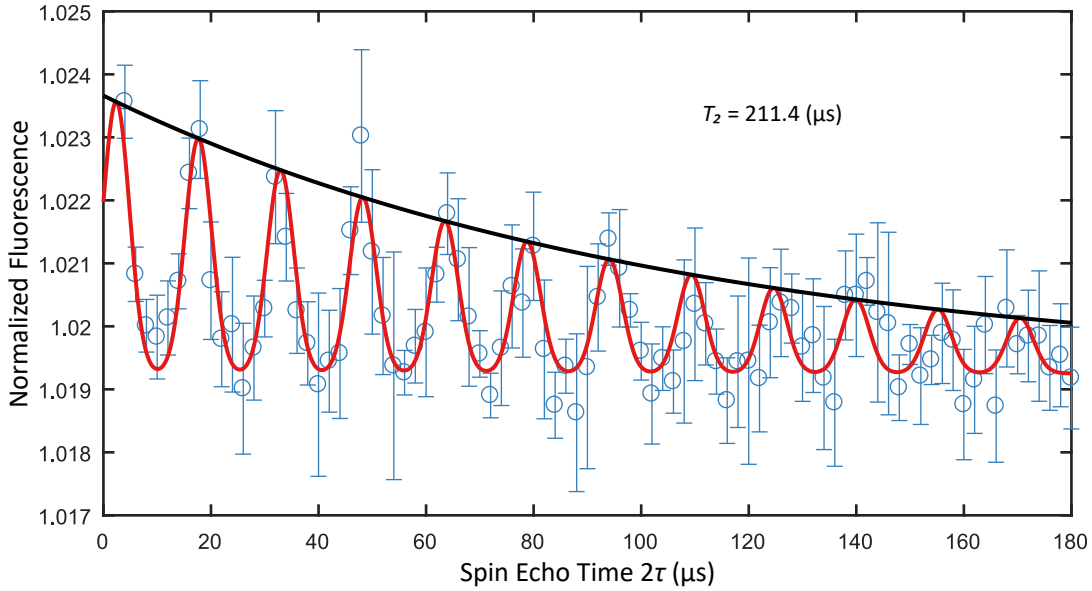

Figure 4-3: **Coherence Time Characterization via Spin Echo Measurements.** Averaged spin echo measurements taken on NV centers in a 25×25 µm^2 field of view on the PCD. Fitting the exponential decay of the revivals gives a mean coherence time of 211 µs.

in each crystal grain, it is difficult to align a magnetic field to the NV axis, resulting in some off-axis field components that can degrade the coherence time [160]. Despite this, we measure a mean coherence time of $T_2 > 200$ µs (Fig. 4-3), indicating that NV centers in this sample maintain long coherence times despite the presence of high strain.

4.2.2 Pulse Sequences

To measure PLE from individual NV centers, we use a pulse sequence consisting of a 5 µs 532 nm pulse to reionize and initialize the NVs into their $m_s = 0$ ground state, followed by a 10 µs pulse from our tunable red laser during which time photon counts are collected on an avalanche photodiode. For the PLE measurement in Figure 4-1e, this is repeated 10^5 times before retuning the frequency and repeating. For the super resolution localization experiments, the laser frequency is locked, and the sequence repeated 10^4 times before moving to the next pixel in the scan.

4.2.3 NV Cluster Characterization

As shown in Figure 4-1e, we measure seven prominent zero-phonon line (ZPL) transitions in the PLE sweep. Our super resolution localization scans indicate that these correspond to three NVs; this is further corroborated by second-order autocorrelation measurements (Figure 4-4a) where the $g^{(2)}(0) = 0.728$ falls between 0.667 and 0.75, the $n = 3$ and $n = 4$ Fock state bounds respectively. In our PLE pulse sequence (see below), we start by initializing the NVs into their negatively charged, $m_s = 0$ spin state. Under perfect initialization and low spin-mixing, this state generally has two allowed transitions into E_x and E_y excited state manifolds. However, as discussed above in 4.1, highly strained systems can experience nontrivial mixing of the larger excited state manifold, yielding observation of more than the expected two transitions per NV center. We probe the ground states using microwave application. Under an applied external magnetic field, we observe four optically detected magnetic resonance (ODMR) dips (Figure 4-4b), indicating that these three NVs have two net orientations (out of four possible). One resonance yields roughly twice as much contrast, indicating that two NVs fall along this orientation and one along the other. To determine which ODMR dips correspond to which NV centers, we apply microwaves at a single frequency corresponding to one of the spin resonances, then selectively read out the system by collecting photon counts during application of a narrow laser locked to a single frequency corresponding to one of the ZPL resonances. If the microwave frequency and optical frequency are both resonant (with their respective transitions) for the same NV, we expect to observe Rabi oscillations in fluorescence with varying microwave application times. If, however, the microwave frequency and optical frequency do not correspond to the same NV, we expect to observe little to no modulation in fluorescence. Repeating this for each pairing of frequencies, we are able to map which magnetic resonances come from which NVs, leading to the finding that, indeed, two NVs correspond to the spin resonance with greater contrast. Furthermore, we are able to resolve the apparent extra ZPL transition, and find that while three of the ZPL peaks correspond to one spatial location (and thus one NV),

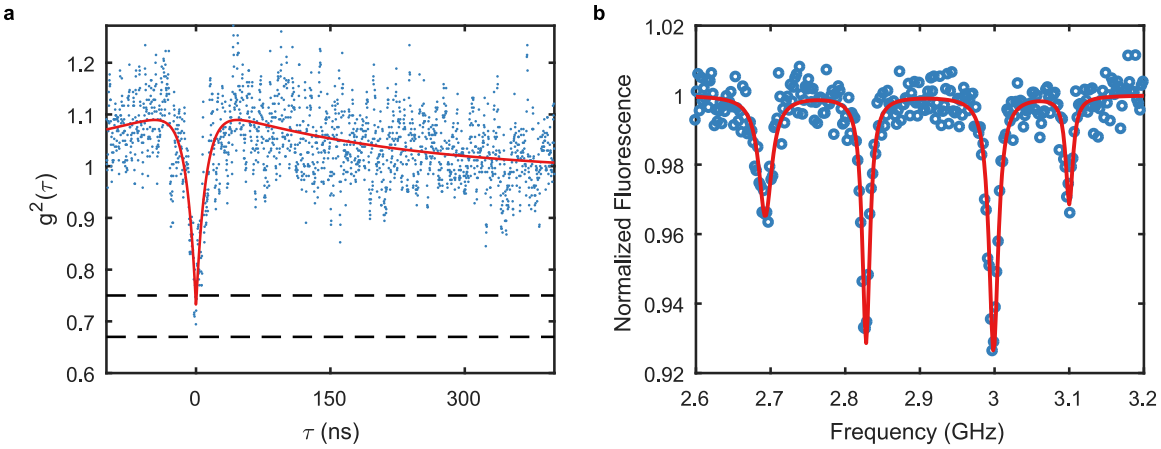

Figure 4-4: **Characterization of an NV Cluster. a**, Second-order autocorrelation measurement of the cluster system under 532 nm illumination. The red line is a fit to a model incorporating a bunching term, necessary due to the presence of shelving states of the NV. The dashed black lines mark the $n = 3$ (0.667) and $n = 4$ (0.75) photon bounds assuming equally measured emission rates from each emitter. **b**, ODMR of the cluster system under an applied external field. In the power-broadened regime, each NV orientation will exhibit at most two resonances, corresponding to the $m_s = 0 \Rightarrow m_s = \pm 1$ transitions. The observation of 4 thus indicates the presence of two orientations in the interrogated spot.

one of these three (peak B) yields an increase in fluorescence under the microwave application described here, while all other transitions yield a decrease in fluorescence. This suggests that this extra peak is from a spin-mixed transition with both $m_s = 0$ and $m_s = 1$ character.

4.3 Super-resolution Localization

We investigate this approach to multi-qubit readout in a Type IIa PCD (see Section 4.2.1). The scanning confocal image in Figure 1c shows NV centers in one domain of this PCD near a gold stripline for microwave delivery that cuts across a grain boundary, visible as the bright strip in the image. Despite the high strain of the PCD [171], its low nitrogen content allows for NVs with coherence times exceeding 200 µs 4.2.1 at room temperature. The distribution of the NV optical transitions (Figure 4-1) indicates an inhomogeneous distribution with standard deviation of 294 GHz, nearly 5 times broader than what we measure in single-crystal diamond samples 4.2.1.

Figure 4-1e shows a photoluminescence excitation (PLE) spectrum taken on a representative fluorescence site on the sample, labeled site 1 in the inset of Figure 4-1c. The spectrum reveals several distinct ZPL peaks, indicative of the presence of multiple NV centers within the diffraction-limited spot. Spatially scanning a narrow laser resonant with one of the transitions in Figure 4-1e preferentially induces fluorescence from a single NV center, selectively imaging this defect out of the cluster. Performing this scan for each observed transition, we find that they correspond to only three spatial positions. Second-order autocorrelation and optically detected magnetic resonance (ODMR) measurements further confirm the presence of three NV centers in this site 4.2.1. The most prominent and well-isolated peaks for each NV center are labeled as A, B, and C in Figure 4-1e. For these transitions, we repeat the resonant imaging experiment 69 times over a period of around 20 hours, each time fitting the result with a Gaussian point-spread function.

Examining the temporal trend for each NV, it is readily apparent that there is some uniform drift on our stage over the course of the measurement period. The independent results of the individual trials are shown in Figure 4-6a, with the color gradient indicating relative time of each data point. As the data from each of the three NVs are well separated and clusters easily identifiable by eye, we plot each with the same color scheme. In Figure 4-6b, for each NV, we plot the difference in x-coordinate and y-coordinate between the fit center at time t and that at time $t = 0$. Both x and y follow clear trends, and linearly fitting these drifts allows us to compensate by shifting each data point's center according to the fitted drift for that time point. This adjustment results in the localization image shown in Figure 4-6c, clearly showing much tighter clustering than Figure 4-6a. It is from these data that we extract the standard distance, i.e. standard deviation in position, for each NV, dividing by $\sqrt{N}$ to convert to a standard error:

$$S(N) = \frac{1}{\sqrt{N}} \sqrt{\frac{\sum_{i=1}^{N} (x_i - \bar{x})^2 + (y_i - \bar{y})^2}{N}} \tag{4.2}$$

where each i is one of the 69 trials and $\bar{x}$ and $\bar{y}$ are mean positions of the total

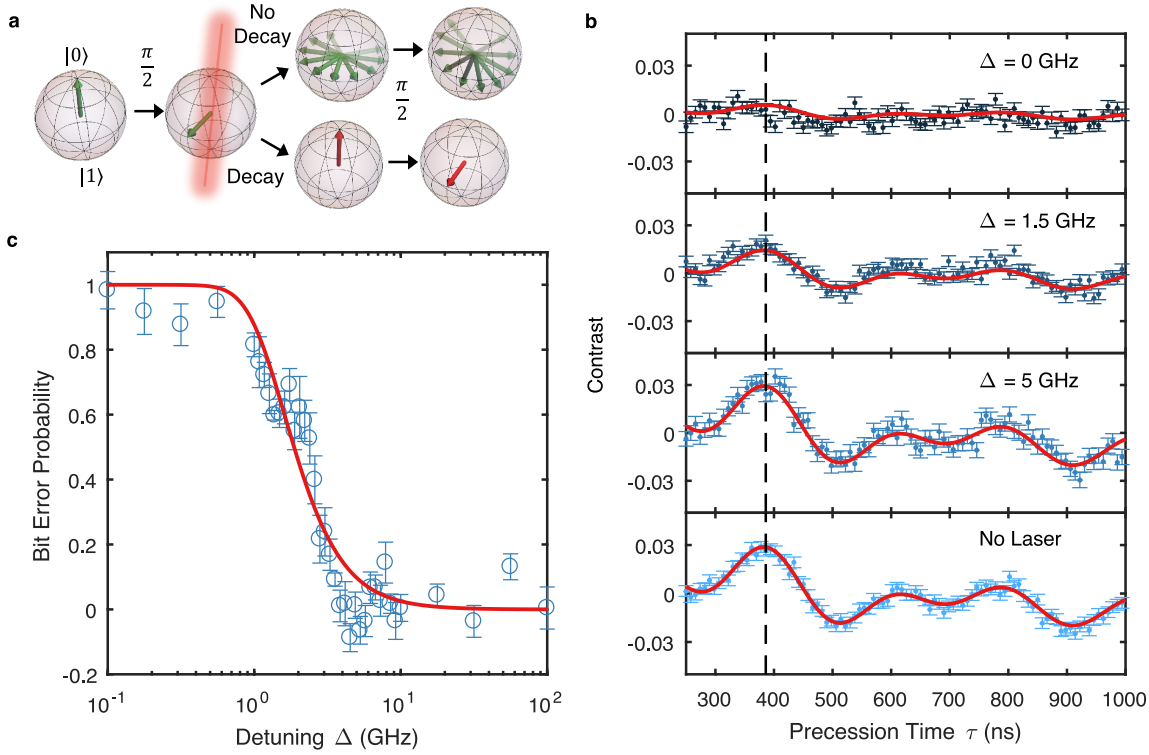

Figure 4-5: **Qubit Degradation under Near-resonant Excitation for a Single Isolated NV. a**, Bloch sphere schematic for crosstalk measurement sequence. After a $\pi/2$-pulse prepares the qubit in a superposition state, it precesses around the Bloch sphere during application of a near-resonant laser. With probability $(1-\Gamma)$, the laser will not induce excitation and subsequent decay, preserving the phase built up during the precession period, which is then mapped into the population by a second $\pi/2$-pulse and readout with a non-resonant readout pulse. However, the laser may also induce a spin-projecting decay event; in this scenario, the second $\pi/2$-pulse will always place the spin in an even superposition state, independent of any phase accumulated during the precessionary period, leading to a precession time-independent intensity at the final readout. **b**, Ramsey sequences with a resonant laser of varying detunings applied during the free precession period. The fits (solid lines) have one fit parameter for the fringe amplitude relative to that of a reference Ramsey taken with no crosstalk laser. **c**, Crosstalk probability as a function of laser detuning, taken by fixing the precession time to the fringe maximum at $\tau = 386$ ns (dashed line in **b**) and sweeping the resonant laser detuning. The contrast values are normalized to the fringe amplitude from the no-laser case. In red, the model for Γ (Eq. 4.13) with one fit parameter for the optical Rabi frequency.

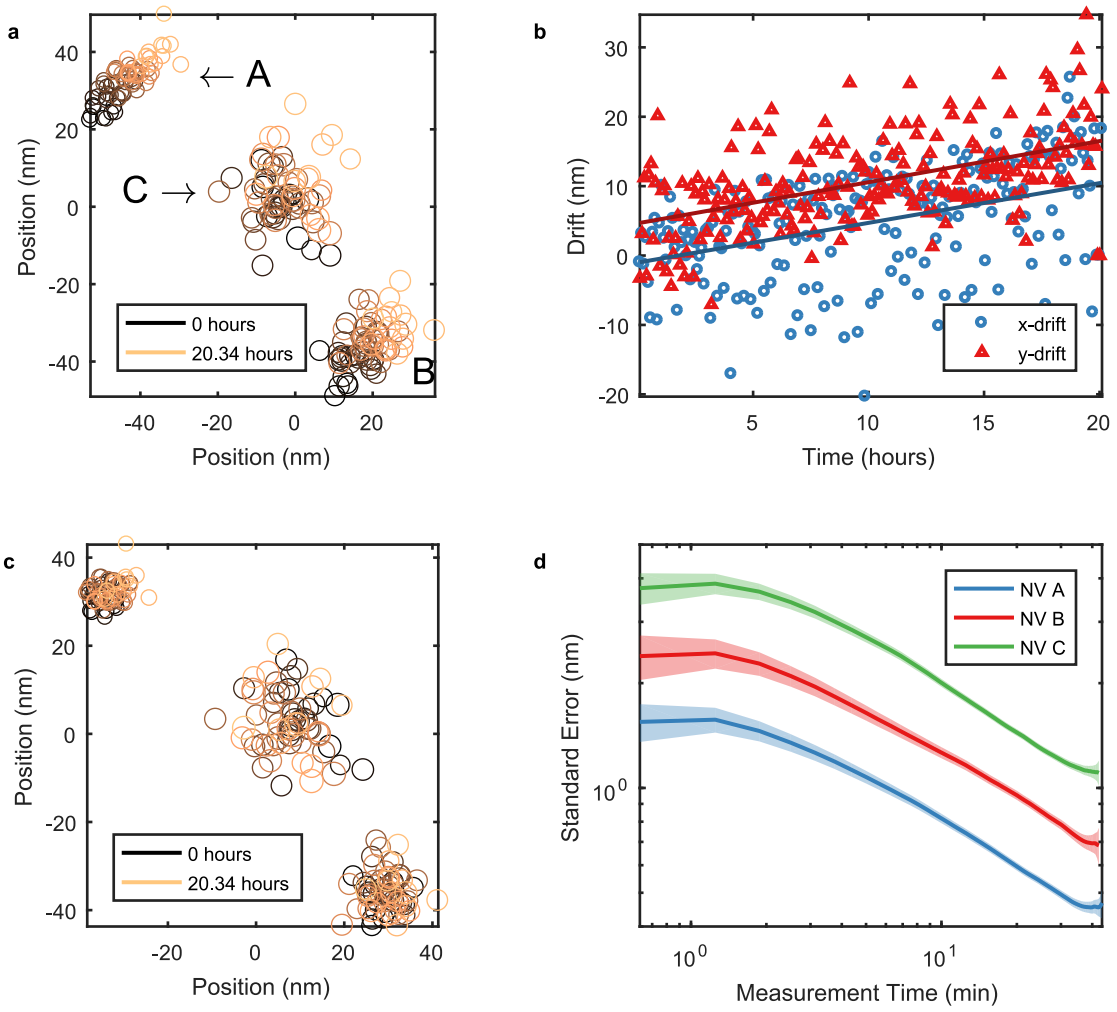

Figure 4-6: **Super-resolution Localization of Individual NV Centers. a**, Results of 69 super-resolution localization trials for each NV, with color representing the time at which the measurement was taken. Different NVs labeled by convention as used above, and given the same color scale, as the clusters are separated enough to distinguish by eye. Sizes of circles are in arbitrary units, but are scaled to indicate 95% confidence intervals on each measurement. **b**, Drift of all three NVs in x (blue circles) and y (red triangles) over the measurement period, overlaid with linear fits. **c**, Data from **a**, with drift compensated according to the fits in **b**. **d**, The standard error as per Equation 4.2 for each NV as a function of total measurement time.

data set (for a given NV). We calculate S for every sequential binning of N trials, with N running from $N = 1$ to $N = N_{max} = 69$. Figure 4-6d plots the mean standard error as a function of total measurement time given by $T = Ndt$, where $dt = 37.5$ seconds is the total pulse sequence time to perform one scan experiment. Error bars indicate the standard error on the calculation of each $S(N)$. Figure 4-1f shows the reconstructed positions. Note that the spot width indicates 10x the localization precision after 40 minutes of integration and the dashed overlay showing the full-width half-maximum size of the original diffraction-limited spot. From these results, we demonstrate a mean localization precision of $\langle S_A \rangle = 0.74$ nm of single NV centers and a precision of 0.45 nm for the brightest and most spectrally distinct NV.

4.4 Individual Readout and Crosstalk

We next consider the degradation that an optical readout of one NV induces in other NVs in a diffraction-limited spot. For simplicity, we first study this crosstalk in a simple system consisting of a single NV (NV_D) in site 2 of Figure 1c, which is initialized into state $|\psi_0\rangle = |m_s = 0\rangle + |m_s = 1\rangle$.

For verification of our crosstalk model, we perform Ramsey interferometry on a well-isolated single NV, verified by second-order autocorrelation measurements (Figure 4-7a), where a value $g^{(2)}(0) < 0.5$ indicates that a single photon emitter is being probed. An important parameter in the crosstalk model is the emitter lifetime. We characterize this on the single NV of interest by time-tagging photon counts after pulsed excitation, with results shown in Figure 4-7b. Fitting the decay after the initial instrument response yields a lifetime of 9.2±0.1 ns. We note that this is lower than the typical 12 ns lifetime commonly reported for NVs in a single-crystal bulk sample; this difference may stem from the presence of a particularly strained environment.

Resonances of otherwise identical systems that are strain-split can experience preferential excitation (and thus fluorescence). In general, the steady-state excited level population of a two-level system with linewidth γ under coherent excitation with

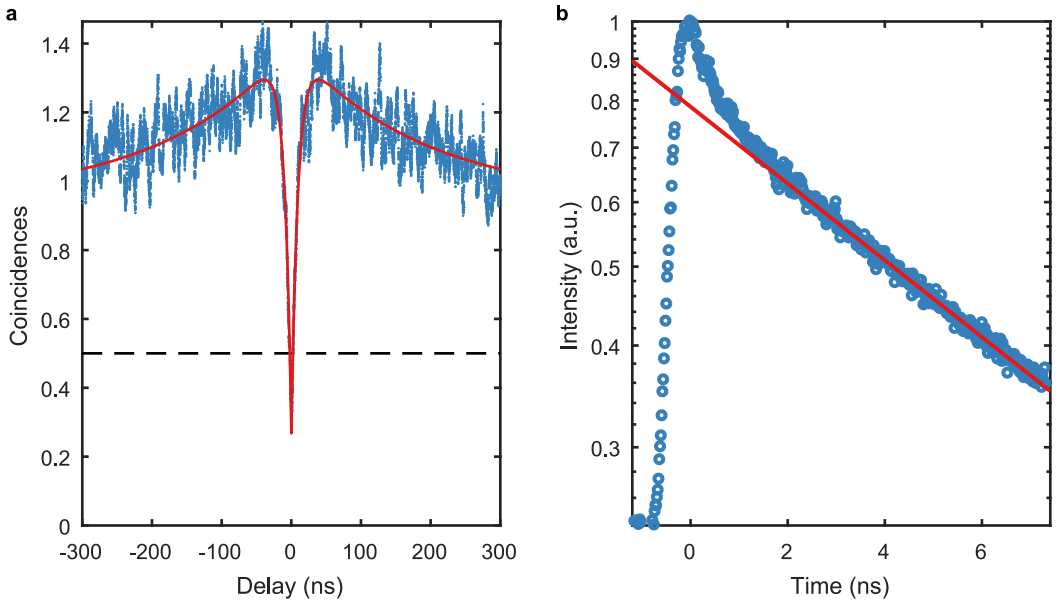

Figure 4-7: **Characterization of a Single NV for Detailed Crosstalk Measurements. a**, Second-order autocorrelation measurement taken with a Hanbury-Brown-Twiss interferometer. The coincidence dip below 0.5 at delay time $\tau = 0$ confirms that we are probing a single emitter. **b**, Lifetime measurements taken via pulsed excitation. The red line fitted to the decay after the initial instrument response yields an excited state lifetime of 9.2±0.1 ns.

Rabi frequency Ω at a detuning Δ is given by the optical Bloch equations to be:

$$\rho_{ee} = \frac{|\Omega|^2}{\left(\frac{\gamma}{2}\right)^2 + \Delta^2 + 2|\Omega|^2} \tag{4.3}$$

For a pair of two-level systems with one on resonance, the ratio of their fluorescence rates is thus:

$$\frac{F_{resonant}}{F_{detuned}} = \frac{\left(\frac{\gamma}{2}\right)^2 + \Delta^2 + 2|\Omega|^2}{\left(\frac{\gamma}{2}\right)^2 + 2|\Omega|^2} \tag{4.4}$$

$$\approx \frac{\Delta^2 + 2|\Omega|^2}{2|\Omega|^2} \tag{4.5}$$

where the approximation in Eq. 4.5 is for the limiting case where $\Delta, |\Omega| \gg \gamma$. While this basic rate enhancement is sufficient for super-resolution localization and readout of an individual system, preservation of the off-resonant system's state requires more stringent conditions. We consider two types of crosstalk mechanisms; first, spin-

projection errors that equate to a "measurement" of the off-resonant NV. For time scales shorter than the spin population decay time T_1, we can treat the NV ground-excited states as a two-level system. During the resonant readout period, the off-resonant NV ($\Delta \gg \gamma$) undergoes Rabi oscillations:

$$\rho_{ee} = \frac{|\Omega|^2}{|\Omega|^2 + \Delta^2} \sin^2\left(t\sqrt{|\Omega|^2 + \Delta^2}\right) \tag{4.6}$$

During this time, a decay from any small excited state population contribution constitutes a measurement of the system that degrades whatever initial spin superposition the NV originally had. In the limit for large detuning and short excitation times such that probability of spontaneous emission is $\ll 1$, this state has an expected number of decay events during a time T:

$$\lambda = \int_0^T \gamma\rho_{ee} dt \tag{4.7}$$

$$= \frac{\gamma|\Omega|^2}{|\Omega|^2 + \Delta^2}\left[\frac{T}{2} - \frac{\sin\left(2T\sqrt{|\Omega|^2 + \Delta^2}\right)}{4\sqrt{|\Omega|^2 + \Delta^2}}\right] \tag{4.8}$$

$$\approx \frac{\gamma|\Omega|^2 T}{2\left(|\Omega|^2 + \Delta^2\right)} \tag{4.9}$$

where in the last line we take $T \gg \frac{1}{\sqrt{|\Omega|^2+\Delta^2}}$, which is appropriate for any non-pulsed measurement. Following Poissonian statistics, the probability Γ of at least one decay event (crosstalk) occurring is then:

$$\Gamma = 1 - e^{-\gamma|\Omega|^2 T/2(|\Omega|^2+\Delta^2)} \tag{4.10}$$

Second, we consider phase errors resulting from differential AC Stark shift on the $|m_s = 0, 1\rangle$ spin ground states. The accumulated qubit phase error is given by the difference:

$$\phi = \frac{|E|^2}{\hbar}\left(\frac{\bar{\mu}_0^2}{\Delta_0} - \frac{\bar{\mu}_1^2}{\Delta_1}\right) t \tag{4.11}$$

where each $\bar{\mu}_i$ is the projection on the field vector of the transition dipole for the spin i ground-excited zero-phonon line transition, and each Δ_i is the detuning of the

near-resonant light from each respective transition. Typically, these transitions will be within ∼10 GHz of one another, and the dipole moments roughly equal (though with different projections owing to the different polarizations of the transitions). To get a sense of the order of magnitude, we treat this in the case where $\Delta_1 \gg \Delta_0$, and note that this is a worse scenario than one would typically expect. We then see that the phase error goes simply with:

$$\phi \sim \frac{|\Omega|^2}{\Delta} t \tag{4.12}$$

Taking typical experimental parameters of $|\Omega| \sim \gamma$, $\Delta \sim 10$ GHz, and $t \sim 100$ ns, this phase error is of order 10^{-2}, and is, therefore, undetectable in our experiment. We further note that under worse conditions, $|\Omega|$, Δ, and t can be well characterized and this phase error corrected.

So, if a laser is applied at frequency ω_L for time T to perform resonant readout on a hypothetical neighboring NV. This laser projects $\mathrm{NV_D}$ by non-resonant spontaneous emission into ground state $|m_s = i\rangle$, where $i \in \{-1, 0, 1\}$, with probability

$$\Gamma_i = 1 - \exp\left(-\frac{\gamma_i \Omega_i^2 T}{2(\Omega_i^2 + \Delta_i^2)}\right), \tag{4.13}$$

where Δ_i is the detuning of ω_L from $\mathrm{NV_D}$'s $|i\rangle$ ground-to-excited state transition, Ω_i is the optical Rabi frequency, and γ_i is the excited state's decay rate.

We probe this laser-induced crosstalk using Ramsey interferometry, as illustrated in Figure 4-5a. The application of an off-resonant laser (detuned by Δ from the NV's E_x transition) during the free precession period projects the NV into the mixed state:

$$\begin{aligned}\rho = (1-\Gamma)\,|\psi\rangle\langle\psi| + \Gamma_0|0\rangle\langle 0| + \Gamma_1|1\rangle\langle 1| \\ + \Gamma_{-1}|-1\rangle\langle -1|,\end{aligned} \tag{4.14}$$

where $|\psi\rangle = \frac{1}{\sqrt{2}}\left(|0\rangle + e^{-i\theta(t)}\,|1\rangle\right)$ is the result of the Ramsey experiment and $\sum \Gamma_i = \Gamma$. In our experiment, $\Gamma_0 \gg \Gamma_1, \Gamma_{-1}$ such that Γ_0 dominates the decay. The latter three terms in Equation 4.14 are stationary states and provide no contrast in the

Ramsey experiment, such that the fringe amplitude is directly proportional to $1-\Gamma$. The final spin state (after the second $\pi/2$-pulse of the Ramsey sequence) is measured by state-dependent fluorescence F through 532 nm illumination. F is normalized to account for power fluctuations by repeating the sequence, but replacing the final $\pi/2$-gate with a $3\pi/2$-gate and taking the contrast $C = \frac{(F_{3\pi/2}-F_{\pi/2})}{(F_{3\pi/2}+F_{\pi/2})}$.

We can derive the functional form of C by evolving our state's density matrix through the experiment. We probe off-resonant crosstalk by applying a near-resonant laser pulse of duration $T = 200$ ns during the precessionary period of a Ramsey interferometry sequence. In this case, crosstalk events manifest as decreased fringe contrast as the qubit is projected into an increasingly mixed state. To fit these results, we first take a reference measurement of a Ramsey sequence with no crosstalk laser applied. The resultant fringes, shown in the last row of Figure 4-5b, are fit to a model with a decaying coherence envelope over three sinusoids corresponding to the three hyperfine transitions from coupling between the NV electronic spin and the nearby nitrogen-14 nuclear spin. Once this fit is retrieved, the data for varying crosstalk laser detunings (Figure 4-5b) are fit to this same equation, but with fixed decay envelope, sinusoid frequencies, phases, and relative amplitudes, leaving only one free parameter for the overall fringe amplitude, which gives the crosstalk probability.

That this crosstalk probability corresponds to the normalized Ramsey fringe amplitude is seen by considering the mixed state generated by the off-resonant pulse. In our Ramsey sequence, the spin is first optically polarized into the $m_s = 0$ spin state, then rotated by a $\pi/2$-pulse. In the $\{|m_s = 0\rangle, |m_s = 1\rangle, |m_s = -1\rangle\}$ basis, the density matrix for this process is:

$$\rho_{\text{initial}} = \begin{bmatrix} 1 & 0 & 0 \\ 0 & 0 & 0 \\ 0 & 0 & 0 \end{bmatrix} \xrightarrow{\pi/2} \frac{1}{2} \begin{bmatrix} 1 & 1 & 0 \\ 1 & 1 & 0 \\ 0 & 0 & 0 \end{bmatrix} \tag{4.15}$$

The precession period then causes build-up of some phase $\theta(\tau)$. However, in the case of the off-resonant laser inducing a spontaneous emission event, the system's spin state is projected. The state at the end of this precession period can thus be written

as a mixed state:

$$\begin{aligned}\rho_{\text{precession}} = \frac{(1-\Gamma)}{2}&\begin{bmatrix} 1 & e^{-i\theta(\tau)} & 0 \\ e^{i\theta(\tau)} & 1 & 0 \\ 0 & 0 & 0 \end{bmatrix} \\ &+\Gamma_0 \begin{bmatrix} 1 & 0 & 0 \\ 0 & 0 & 0 \\ 0 & 0 & 0 \end{bmatrix} + \Gamma_1 \begin{bmatrix} 0 & 0 & 0 \\ 0 & 1 & 0 \\ 0 & 0 & 0 \end{bmatrix} + \Gamma_{-1} \begin{bmatrix} 0 & 0 & 0 \\ 0 & 0 & 0 \\ 0 & 0 & 1 \end{bmatrix}\end{aligned} \tag{4.16}$$

Where Γ_i is the probability of at least one spontaneous decay event into the ith ground state, and $\Gamma_0 + \Gamma_1 + \Gamma_{-1} = \Gamma$. The final $\pi/2$-pulse of the Ramsey sequence then produces the final state:

$$\begin{aligned}\rho_{\text{final}} = \frac{(1-\Gamma)}{2}&\begin{bmatrix} 1-\cos(\theta(\tau)) & i\sin(\theta(\tau)) & 0 \\ -i\sin(\theta(\tau)) & 1+\cos(\theta(\tau)) & 0 \\ 0 & 0 & 0 \end{bmatrix} \\ &+\frac{\Gamma_0}{2} \begin{bmatrix} 1 & 1 & 0 \\ 1 & 1 & 0 \\ 0 & 0 & 0 \end{bmatrix} + \frac{\Gamma_1}{2} \begin{bmatrix} 1 & -1 & 0 \\ -1 & 1 & 0 \\ 0 & 0 & 0 \end{bmatrix} + \Gamma_{-1} \begin{bmatrix} 0 & 0 & 0 \\ 0 & 0 & 0 \\ 0 & 0 & 1 \end{bmatrix}\end{aligned} \tag{4.17}$$

At which point we measure the fluorescence under 532 nm illumination, which yields:

$$\begin{aligned}F_{\pi/2} = &\left[\frac{(1-\Gamma)}{2}\left(1-\cos(\theta(\tau))\right) + \frac{\Gamma_0}{2} + \frac{\Gamma_1}{2}\right] F_0 \\ &+ \left[\frac{(1+\Gamma)}{2}\left(1+\cos(\theta(\tau))\right) + \frac{\Gamma_0}{2} + \frac{\Gamma_1}{2}\right] F_1 + \Gamma_{-1} F_{-1},\end{aligned} \tag{4.18}$$

where F_i is the average fluorescence from the $|m_s = i\rangle$ state. For normalization over power fluctuations, we repeat this experiment, replacing the final $\pi/2$-pulse with

a $3\pi/2$-pulse, which yields:

$$\begin{aligned} F_{3\pi/2} = &\left[\frac{(1+\Gamma)}{2}\left(1+\cos(\theta(\tau))\right)+\frac{\Gamma_0}{2}+\frac{\Gamma_1}{2}\right]F_0 \\ &+\left[\frac{(1+\Gamma)}{2}\left(1-\cos(\theta(\tau))\right)+\frac{\Gamma_0}{2}+\frac{\Gamma_1}{2}\right]F_1+\Gamma_{-1}F_{-1} \end{aligned} \tag{4.19}$$

Note that in both cases $F_1 = F_{-1}$. Using this, the contrast $C = \frac{(F_{3\pi/2}-F_{\pi/2})}{(F_{3\pi/2}+F_{\pi/2})}$ is then found to be:

$$C = \frac{(1-\Gamma)\cos(\theta(\tau))\left[F_1-F_0\right]}{\left[F_1+F_0\right]+\Gamma_{-1}\left[F_1-F_0\right]} \tag{4.20}$$

In our experiment, the Γ_{-1} term is small ($\Gamma_{-1} \ll 1$), allowing us to simplify the above:

$$C = (1-\Gamma)\cos(\theta(\tau))\frac{\left[F_1-F_0\right]}{\left[F_1+F_0\right]}, \tag{4.21}$$

such that the time-varying fringe amplitude of the contrast in the main text is directly proportional to the crosstalk fidelity $(1-\Gamma)$. The correspondence between our model and the measured data in Figure 4-5c further supports that $\Gamma_{-1} \ll 1$.

Figure 4-5b plots C for varying Δ. For $\Delta = 0$, the Ramsey contrast vanishes, as expected for the laser-induced state projection. With increasing detuning, the fringe contrast recovers, approaching a control experiment without a readout laser.

We map the crosstalk as a function of Δ by fixing the precession time to the fringe maximum at 386 ns and sweeping the resonant laser over a wide range of detunings. These data are converted to a bit error probability in Figure 4-5c by normalizing the fluorescence from each detuning to that from the reference "no-laser" control experiment (Fig. 4-5b), which gives the crosstalk-free case. The red curve represents our model from Equation 4.13 with only one fit parameter for the optical Rabi frequency, which is difficult to accurately measure experimentally due to spectral diffusion of the ZPL. The optical excitation time T is fixed by our pulse generator, and the decay rate is determined by lifetime characterization (Fig 4.2.1. The theory

shows good agreement with our data and indicates that a detuning of 16 GHz or greater keeps crosstalk errors below 1%, a regime accessible by the cluster at site 1 of Figure 4-1c.

4.5 Simultaneous Control

4.5.1 Logical Green Readout

Due to experimental limitations associated with the availability of a single red laser, we are forced to use non-selective 532 nm excitation to read the states of NVs A and B. In order to measure the states of NVs A and B in a way that is still independent of the state of NV C, we use a multi-pulse logical green readout. In this sequence, we first ionize NV C with a red pulse (2 µs) resonant with this NV's ZPL transition. To ensure ionization independent of the state of NV C, we further perform a π MW pulse (32 ns) on this NV followed by another red pulse. The readout is then concluded by a 5 µs 532 nm pulse, where the first 500 ns are used for photon count collection and the remaining time is used to reset the charge state of the system.

4.5.2 Pulse Sequences

The full pulse sequence used for the simultaneous control experiments is described in Figure 4-8. As shown in Figure 4-8a, all spins are first initialized with a 5 µs 532 nm pulse. Next, a reference Ramsey measurement is taken on the two NVs of like orientation (NVs A and B) by applying a $\pi/2$ MW pulse (SMIQ06B, -9 dBm preamplifier, 42 ns), waiting for a free precession time τ, then applying another $\pi/2$-pulse. Finally, we measure the state of these two NVs via a logical green readout, described in detail below.

After this reference Ramsey, the simultaneous control sequence in Figure 4-8b is performed. With all NVs initialized following the green readout, we first induce coherent Rabi oscillations in NV C by applying resonant MW (SMV03, 0 dBm pre-amplifier) for a time τ. Next, we perform the same Ramsey pulse sequence as above;

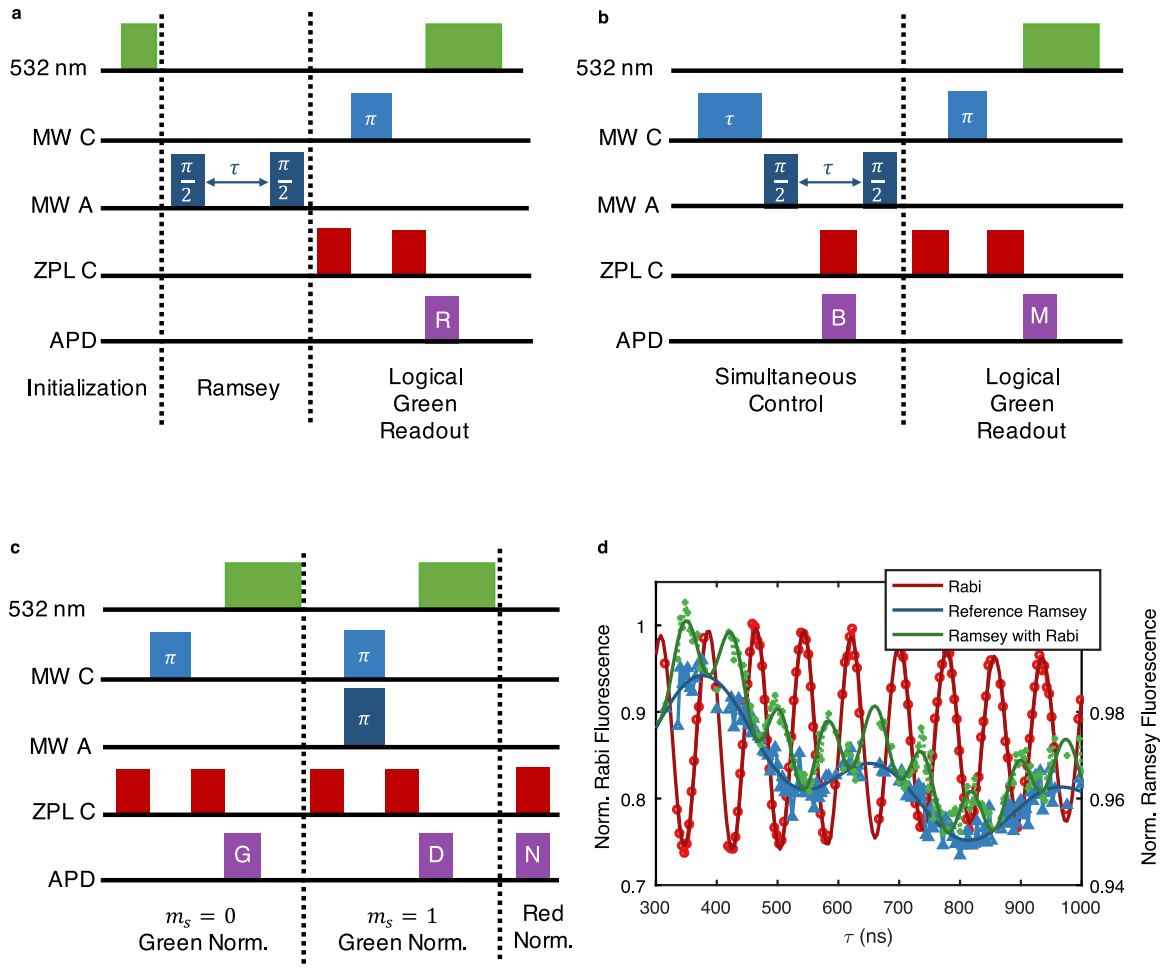

Figure 4-8: **Full Pulse Sequence and Results for Simultaneous Control Experiments.** Sequences depicted in **a-c** were run end-to-end and repeated to yield the results shown in **d**. **a**, Sequence for reference Ramsey. **b**, Sequence for demonstrating simultaneous control by inducing Rabi oscillations on one spin population concurrent with a Ramsey sequence on another spin population. **c**, Sequences for normalizing the data collected in **a** and **b**. **d**, Fluorescence results normalized by the $m_s = 0$ green norm or red norm as appropriate, without any further modification.

however, during the free precession period, we apply a red pulse resonant with the ZPL transition of NV C for a time $T = 300$ ns to read out its state, simultaneously collecting photon counts on an APD. After the second $\pi/2$-pulse concludes the Ramsey sequence, the system is read out with a logical green readout.

The next sets of pulses in Figure 4-8c are used for normalization. First, we perform our logical green readout to normalize the bright $m_s = 0$ state of all NVs. Next, we repeat the logical green readout, but with a π pulse performed on NVs A and B in order to normalize the dark $m_s = 1$ states of these two NVs. Lastly, we repeat our red readout pulse to normalize to the bright state of NV C.

4.5.3 Raw Data Analysis

Figure 4-8d shows the raw counts divided by the appropriate normalization counts (G for all Ramseys, N for the Rabi), along with the fits described below.

We normalize the raw Rabi signal by dividing the counts retrieved during the B bin by those retrieved during the red normalization bin N. This is fit with a model for Rabi oscillations with a sinusoidal envelope for the additional hyperfine interaction:

$$\text{Rabi } = [A_1 + A_2 \cos(\omega_1 \tau)] \cos(\omega_2 \tau - \phi) + C_B \tag{4.22}$$

The fit minimum $A_1 + A_2$ is then used to normalize the counts to a population measurement as shown in the main text (Figure 4-9b).

The raw Ramsey counts (from both reference R and simultaneous control M signals) are normalized by the green $m_s = 0$ normalization bin G. These results are plotted in Figure 4-8d; for the main text, the reference (simultaneous control) signals are converted into a population measurement using the following normalization:

$$|c_0|^2 = \frac{R(M) - D}{G - D} \tag{4.23}$$

This yields the results shown in Figure 4-9b. The reference Ramsey is fit to the following model, with three sinusoids for each of three hyperfine levels, as well as a

decay term for the finite NV coherence time T_2:

$$\text{Ramsey } = e^{-\tau/T_2}\Big[A_1\cos(\omega_1\tau-\phi_1)+A_2\cos(\omega_2\tau-\phi_2)+A_3\cos(\omega_3\tau-\phi_3)\Big]+C_M \quad (4.24)$$

For the simultaneous control Ramsey, due to infidelities in the π-pulse during the logical green readout, we see an additional signal from the Rabi on NV C corresponding to imperfect ionization of the $m_s = 1$ state. We thus fit this signal to the following model:

$$S = A_1\text{Ramsey} + C_M + A_2(1 - \text{Rabi}) \quad (4.25)$$

Where the "Ramsey" and "Rabi" terms correspond to the fit results of the signal components of the above two models without offsets C_B and C_M, and the C_M term here is similarly not a fit parameter, but the same constant fit in the reference Ramsey. In this way, the only two fit parameters are the fidelity of the Ramsey signal A_1 and the relative contribution from the Rabi signal A_2, letting us determine the crosstalk. The crosstalk fidelity of our readout $(1 - \Gamma) = A_1$ is determined to be near unity at $A_1 = 1 \pm 0.04$, indicating that we have no detectable degradation of our signal as a result of the individual readout on NV C. This is consistent with our model; based on the known $\gamma = 13$ MHz, $\Omega = 1.7$ GHz, readout time $T = 300$ ns, and detuning $\Delta = 23$ GHz shown in Figure 4-1e, our model predicts a bit error probability of around 1%, below the 4% fit bounds. The residual difference between S (data) and the reference Ramsey fit has a mean of 0.47%, further supporting our claim of crosstalk-free readout.

4.5.4 Results

In this section, we demonstrate individual control and readout on this cluster. We achieve independent microwave control of the spin states by applying a magnetic field, which splits the spin levels depending on the NV center crystal orientation. In this

cluster, we find that two of the NV centers (A and B) are oriented along one crystal axis and the third (C) along another, as indicated by the four dips in the magnetic resonance spectrum as seen in Figure 4-4b.

We take advantage of this ground state splitting and apply the same Ramsey sequence from above to perform individual control and readout. Figure 4-9a shows the gate representation of our sequence. After initialization of all three NV centers with a 532 nm repump, the spin of NV C is coherently driven with a resonant microwave pulse for a time τ, inducing Rabi oscillations corresponding to a rotation of angle θ about the X-axis. Next, NVs A and B are rotated into an equal superposition state by a $\pi/2$-pulse, followed by a passive precession by angle ϕ about the Z-axis for the same time τ. While NVs A and B are in this phase-sensitive superposition state, we perform individual readout on NV C using a resonant optical pulse. After waiting a total precession time τ, a final $\pi/2$-pulse completes the Ramsey sequence on NVs A and B, and we read out these states with 532 nm light. Note that while limitations in the available equipment necessitated the use of a non-resonant green readout on NVs A and B, additional lasers or modulators would allow for individual readout of each NV center in the cluster. Figure 4-9b shows the results of each readout window, where both gates measure the expected Rabi and Ramsey signals. Comparing these Ramsey results to that of a control Ramsey experiment on NVs A and B taken with no additional control or readout sequences on NV C, the fringe amplitudes are equal within our noise bounds (0(4)% bit error probability). That is, we find no detectable fringe amplitude degradation as a result of the resonant readout pulse, indicating that the states of the off-resonant NV centers are left unperturbed through this readout. This result is consistent with our model, which predicts a bit error probability of $\sim 1\%$, below the 4% fit bounds.

4.6 Outlook

We assess the viability of this platform for the creation of scalable multi-spin registers by considering the probability that systems of multiple distinguishable emitters are

effectively formed. Figure 4-11a shows the inhomogeneous distribution of NV center ZPL frequencies acquired on a single crystal diamond (SCD, see section 4.2.1) from a data set of 406 ZPL transitions from 197 distinct emitter sites. In this section, we consider an SCD to compare our results with those acquired from samples most typically used in diamond quantum information experiments [175, 67, 34]. From this distribution, we build an empirical kernel estimate (red curve, Figure 4-11a).

The data sets for the empirical ZPL distributions are built using a multi-step sample characterization process designed to minimize sampling bias by using low thresholding at each stage in order to ensure all potential candidates are fully investigated. First, a confocal fluorescence scan under 532 nm excitation is taken, and bright peaks are identified via coarse Gaussian image filtering and basic peak-finding. Second, the optical spectrum of each identified bright spot is acquired and analyzed for peaks in the range 636–638 nm. Finally, we perform high-resonant-power PLE measurements on all bright spots with identifiable spectral peaks. The use of high power here broadens the resonance lines, but does not change the central frequency, and ensures that even dimmer NVs will pass the threshold for peak-finding at this stage and be included in our final data set. The empirical distributions for both the single-crystal and the polycrystalline samples are shown in Figure 4-10. As can be seen, the PCD exhibits a much broader distribution, which stems from the high-strain nature of the diverse grain structure. As the strain environment and corresponding ZPL distribution vary significantly between grains in the polycrystalline sample, we restrict our analysis to data from one representative grain, resulting in a lower number of data points compared to the single-crystal case.

Based on Monte Carlo sampling from this measured distribution, we estimate the probability that N emitters in a cluster have a crosstalk probability $\leq \Gamma$ under the parameters used for our multi-shot readout (MSR) shown in Figure 4-5. These results are given in Figure 4-11b. For example, the probability for an $N = 3$ NV site to have a crosstalk $\Gamma \leq 10^{-2}$ is estimated at 27%. If each of the NVs were coupled to 3 nuclear spin data qubits, such an $N = 3$ system would be sufficient for implementing the [9,1,3] Shor-Bacon code [10].

Improved light collection using photonic microstructuring and single-shot readout (SSR) [136] could markedly improve these yields. To this end, we repeat our simulation under experimental parameters ($\Omega = \gamma$, $T = 3.7$ µs) comparable to those used to achieve single shot readout with 97% fidelity in a solid immersion lens [67]. The results in Figure 4-11c indicate an increase to 45% of the $N = 3$ yield discussed above. Keeping these readout parameters and additionally assuming the measured ZPL distribution for the PCD (Figure 4-1d) produces the yield histogram in Figure 4-11d, which shows that registers of $N = 9$ NVs with $\Gamma \leq 10^{-2}$ could be produced with 39% yield.

In conclusion, we demonstrated readout of individual solid-state qubits within a diffraction-limited cluster. This capability was enabled by strain-splitting of the NV centers' ZPL transitions in a PCD. While this work uses native strain, the strain field may also be engineered [97] to provide greater control and increase inhomogeneous distributions. If an application necessitates a low-strain environment, these resonances can also be shifted by applying a DC electric field, allowing defects of different orientations — or the same orientation under a strong field gradient — to be uniquely addressed. The technique presented here is also applicable to other atom-like emitters, such as quantum dots [128], rare-earth ions [48], and other solid-state color centers. When combined with existing techniques designed to produce sub-diffraction clusters via aperture implantation [75], entangling defect centers with ancilla nuclear spins [3], and single-shot readout [136], this provides a path towards creating large ensembles of individually-addressable qubits, with a number of applications. For example, error-corrected registers using the 7-qubit [161] or 9-qubit [10] codes could be constructed with clusters of multiple coupled NV-dark spin systems, with full connectivity given by spin-spin coupling between adjacent NV centers. This would allow extension of architectures comprising one optically active and multiple dark spins [3] by reducing the problem of spectral crowding, as well as increasing the effective gate rate by parallelization. NV clusters with individual readout could also enable entanglement-assisted and spatially-resolved nanoscopic quantum sensing [46]. Finally, such clusters present an appealing architecture for modular quantum com-

puting schemes [113, 120] and spectrally-multiplexed quantum repeaters [152].

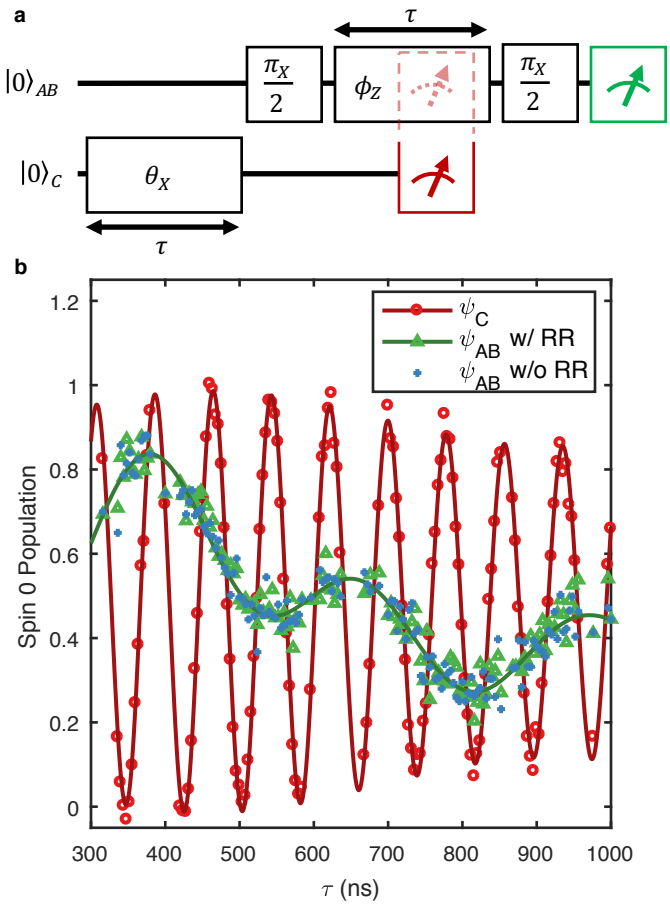

Figure 4-9: **Simultaneous Control and Readout of Three NVs in a Sub-diffraction Volume. a**, Gate sequence for demonstrating simultaneous control and readout of multiple NVs. A Rabi sequence is performed on NV C, followed by a subsequent Ramsey sequence on NVs A and B. During the Ramsey sequence, the state of NV C is read out using resonant readout (RR). The RR gate is depicted as partially spilling into $|\psi\rangle_{AB}$ to indicate the possibility of crosstalk. **b**, Results of the sequence in **a**, showing Rabi oscillations on NV C (red circles) and Ramsey fringes for NVs A and B (green triangles), alongside the reference Ramsey fringes (blue diamonds) for NVs A and B taken with no Rabi sequence nor RR on NV C. The green fit to the data for $|\psi\rangle_{AB}$ indicates no signal degradation within measurement error bounds.

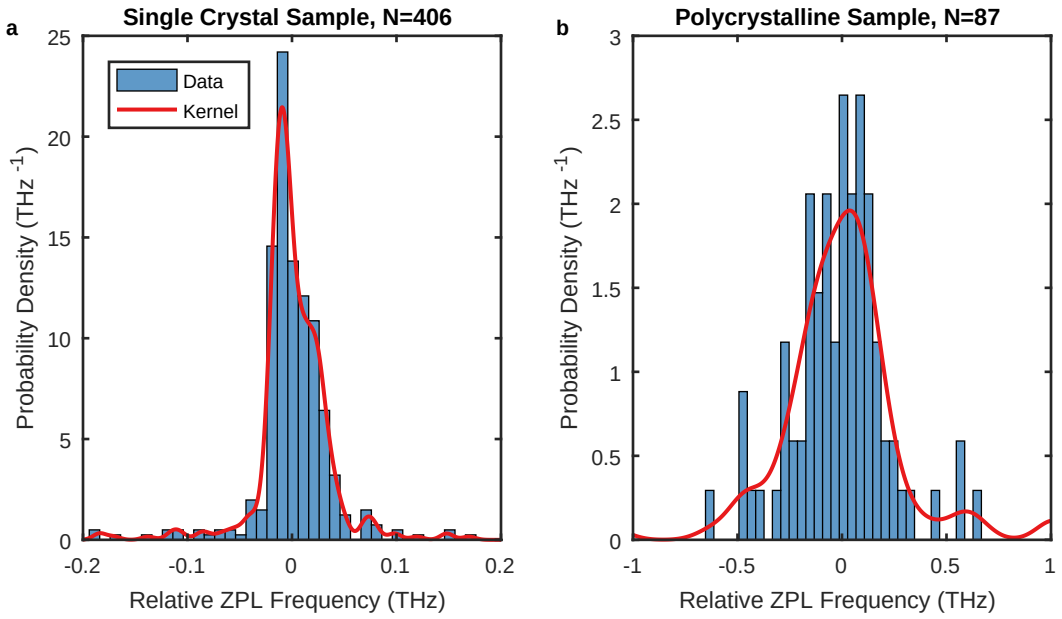

Figure 4-10: **Comparison of Data Sets for Empirically-Determined Inhomogeneous Distributions of Resonances. a**, Data and kernel estimate for the single crystal sample. **b**, Data and kernel estimate for the polycrystalline sample. Note the difference in scaling of the horizontal axes.

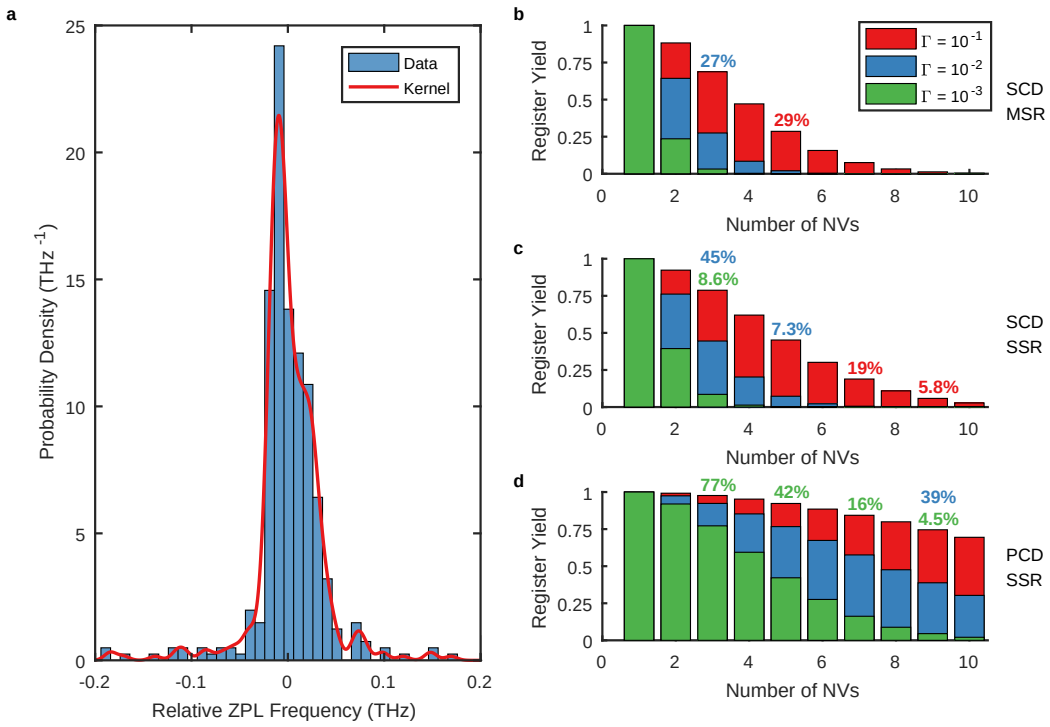

Figure 4-11: **Architecture Scalability.** **a**, Histogram (blue bars) of 406 ZPL resonance frequencies normalized to be in units of probability density, and corresponding kernel density estimate (red line) of this inhomogeneous distribution. **b-d**, Simulated probabilities of successfully creating viable registers of varying numbers of NVs under different tolerance thresholds for the probability Γ of undesired spontaneous decays from off-resonant NVs. **b**, Results using MSR parameters shown in this work and the low-strain SCD distribution in **a**. **c**, Results using parameters used to demonstrate high-fidelity SSR [136, 67] and the low-strain SCD distribution in **a**. **d**, Results using single-shot readout parameters and the high-strain distribution measured in the PCD sample from Figure 4-10.

Chapter 5

NV Centers Formed by Ion Implantation

The advancement of quantum optical science and technology with solid-state emitters such as nitrogen-vacancy (NV) centers in diamond critically relies on the coherence of the emitters' optical transitions. A widely employed strategy to create NV centers at precisely controlled locations is nitrogen ion implantation followed by a high-temperature annealing process. In this thesis, I report on experimental data directly correlating the NV center optical coherence to the origin of the nitrogen atom. These studies reveal low-strain, narrow-optical-linewidth (<500 MHz) NV centers formed from naturally-occurring ^{14}N atoms. In contrast, NV centers formed from implanted ^{15}N atoms exhibit significantly broadened optical transitions (>1 GHz) and higher strain. The data show that the poor optical coherence of the NV centers formed from implanted nitrogen is not a consequence of an intrinsic effect related to the character of the diamond or isotope itself. These results have immediate implications for the positioning accuracy of current NV center creation protocols and point to the need to further investigate the influence of lattice damage on the coherence of NV centers from implanted ions.

This Chapter reuses portions of our paper on the "Optical coherence of diamond nitrogen-vacancy centers formed by ion implantation and annealing" and its corresponding supplementary material [173].

Coherent optical control over solid-state quantum emitters has enabled new advances in quantum science [5, 8, 91] and may lead to technologies such as quantum networks [185]. A quantum network crucially relies on entanglement connections that can be established through a coherent spin-photon interface. The nitrogen-vacancy (NV) defect center in diamond is a well-suited candidate owing to a spin ground state with a long coherence time [12, 2], nearby nuclear spins for quantum memories [78] or algorithms [176, 41, 92], and spin-selective optical transitions allowing for efficient optical spin initialization and readout [137]. Moreover, at low strain and low temperature (< 10 K), effects from phonon mixing in the excited state are small [61, 64], and the optical transition can be coherent. Indeed, narrow-linewidth, coherent optical transitions [164, 13, 135] have been used for the generation of indistinguishable photons suited for two photon quantum interference [22, 156] and entanglement generation between remote NV centers [20].

To date, all experiments employing coherent photons from NV centers have been performed with NV centers that were formed during diamond growth. Key to their optical coherence is that these NV centers experience an environment with few defects since the stability of optical transitions (as with many solid-state systems) suffers from unwanted interactions with nearby bulk and surface defects leading to changes in the strain and electric-field environment [93, 60, 119, 143, 58]. For NV centers with a broadened linewidth below ≈ 200 MHz dominated by slow spectral diffusion, protocols using resonant charge repumping [157] and real-time monitoring of the transition frequency [68] have been used to reduce the broadened linewidth to an effective linewidth below 50 MHz, a transition linewidth suitable for quantum optical experiments. However, such protocols are challenging for NV centers with greater spectral diffusion.

Instead of being limited to NV centers formed during diamond growth, NVs can be created, for example, by nitrogen ion implantation [123]. Nitrogen ion implantation provides an NV positioning accuracy that enables integration with on-chip photonics [102, 147] and coupling between nearby NV centers [62, 54, 188]. Precise positioning of NV centers or accurately registering their location is also a prerequisite for

optimal overlap of the dipole with the electric field mode of diamond optical cavities, for engineering and enhancing light-matter interaction [57, 58, 66, 84, 86, 134, 131]. Moreover, ion implantation allows for the creation of single NV centers in high purity diamond, providing a potentially low-defect environment [119].

However, the bombardment of the diamond with nitrogen ions creates crystal damage that can deteriorate spin and optical coherence properties of NV centers [60, 119]. High-temperature annealing can mitigate some of these issues by repairing the diamond lattice [83, 106, 187, 45]. A procedure including a low implantation dose, careful cleaning, and high-temperature annealing was reported by Chu et al. [35], leading to the creation of narrow-linewidth NV centers. These narrow-linewidth NV centers can result from implanted nitrogen atoms, or from native nitrogen atoms, combined with, for example, implantation-induced vacancies (Figure 5-5a). In principle, the source of nitrogen can be verified by implanting ^{15}N isotopes (natural abundance 0.37%) and resolving the hyperfine structure of the NV magnetic spectrum [130], as done in studies of the spin coherence [115, 187] and creation efficiency [62, 107, 170, 186, 17] of NVs formed from implanted nitrogen. However, in Chu et al. [35] the isotope of the narrow-linewidth NV centers was not investigated [1]. In a later study with similar results [131], ^{14}N isotopes were implanted, so that the origin of the NV center's nitrogen atom could not be determined. Here we report on a study that enables us to directly correlate the optical linewidth of NV transitions to the NV formation mechanism.

5.1 Samples and Processing

Sample A

Sample A and the data set for sample A were acquired and prepared at MIT. We used a type IIa chemical vapor deposition (CVD) grown diamond (Element Six), with a $\langle 100 \rangle$ crystal orientation. The nitrogen content is specified to be less than 5 ppb and is typically less than 1 ppb. The diamond contains a natural abundance

of carbon isotopes. This sample was implanted with $^{15}N^{+}$ (minimum purity 98%) at 85 keV (fluence of 10^9 N/cm^2) by Innovion Corporation. After implantation, the diamond underwent cleaning involving a tri-acid clean (boiling sulfuric, nitric and perchloric acids [1:1:1] for one hour) followed by a Piranha clean (sulfuric acid and hydrogen peroxide in a ratio of [3:1]). The sample was subsequently annealed at high temperatures [35]. During the annealing process the temperature was increased at a rate of 1°C/min and held constant for 2 hours when temperatures reached 400°C, 800°C and 1200°C respectively. The sample underwent the same acid treatment sequence following the annealing process.

Sample B

Sample B was prepared at Delft with a protocol identical to that used in sample A, with the exception of an annealing procedure specified below. The data set for sample B was also acquired at Delft. As with sample A, we used a type IIa CVD grown diamond (Element Six), with a ⟨100⟩ crystal orientation. The diamond was cut, thinned and polished by Delaware Diamond Knives (DDK) into thin (∼14 µm) membranes, one of which is sample B. The membrane was implanted with $^{15}N^{+}$ at 400 keV (fluence of 10^8 N/cm^2) by Innovion Corporation. At this energy, nitrogen ions will travel on average approximately 400 nm below the diamond surface, as verified through simulation using SRIM [191]. Subsequently, the sample underwent an acid clean in boiling sulfuric, nitric and perchloric acids [1:1:1] for one hour, followed by 15 minutes in a Piranha solution. After cleaning, the sample was annealed at high temperatures [35] at Harvard University. During the annealing process the temperature was increased from room temperature to 400°C over a 4 hour period and subsequently held constant for 8 hours. Following this step, the temperature was increased to 800°C over a 12 hour period, and held constant for 8 hours. Finally, the temperature was increased to 1100°C and held constant for 2 hours. After annealing, the sample underwent the same acid treatments as before annealing. Through Van der Waals forces, we bonded the sample to a fused silica substrate [28]. The fused silica substrate had integrated gold MW striplines patterned on the surface for spin

control as detailed in Ref. [28].

5.2 MIT Automation Protocol

Experiments were performed using a home-built scanning confocal microscope. The samples were cooled to 4 K using a closed-cycle helium cryostat (Montana Instruments) and were imaged through a 0.9 NA vacuum objective. A Coherent Verdi G5 laser was used to generate 532 nm light and resonant red light tunable around 637 nm was generated by a New Focus Velocity tunable diode laser. Microwave (MW) signals were generated by a Rohde & Schwarz SMIQ06B signal generator and sent through a high-power amplifier (Mini-Circuits ZHL-16W-43+) before delivery to the sample via a wire soldered (15 µm diameter) across the surface. An Excelitas avalanche photodiode (APD) served as our single photon detector. Wavelength/frequency measurements were made with a Princeton Instruments Isoplane SCT 320 spectrometer and/or a WS7 HighFinesse wavelength meter (these two devices were calibrated relative to each other by scanning the Velocity laser through the wavelengths of interest). All digital signals used to produce pulse sequences were generated on a PulseBlaster ESR-Pro from SpinCore; additional analog control and photon counting were performed on a USB NI6343 from National Instruments. The automated measurement sequence for sample A is shown in Figure 5-1 in detail.

5.2.1 NV Identification

Fluorescent spots were identified using a peak-detection algorithm on a confocal scan. The image was first filtered using a spatial band-pass filter (constructed with a "low-pass" Gaussian kernel with a full-width at half-maximum (FWHM) of 235 nm and a "high-pass" Gaussian kernel with a spatial FWHM of 700 nm). A peak is defined as a pixel that is greater than or equal to its 4 nearest neighbors and greater than the 4 second nearest neighbors. A threshold was calculated to be 1-2 standard deviations above the median pixel value. Only peaks that carried an intensity value above the calculated threshold were used in the experiment. Each image was inspected, and the

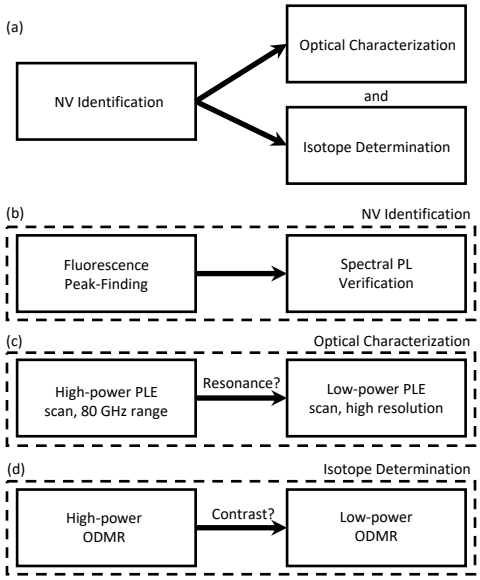

Figure 5-1: **Measurement Sequence for Sample A. (a)** The three parts of the experimental sequence: NV identification, optical characterization and isotope recognition are executed by an automated protocol. **(b)** Fluorescent peaks are identified after processing the image with a spatial band-pass filter and taking peaks above a certain threshold (more detail in the text). This yields many NV candidates that are tested for the presence of PL between 636-639 nm using a spectrometer to confirm the peak is from an NV. **(c)** Using the wavelength of the peak identified in **(b)**, we coarsely tune the resonant laser to the emitter and scan over the entire range allowed by the cavity (82 GHz) with high power to assure we do not miss the transition peak. Once found, we repeat the measurement with higher resolution and low enough power to avoid power-broadening. **(d)** For each NV center a low-power continuous wave (CW) ODMR spectrum is taken, to find the N isotope.

threshold fine-tuned before continuing the experiment to ensure that every visible peak was located.

The fluorescent spots were validated by examining a PL spectrum under 532 nm excitation for a peak between 636 nm and 639 nm (the range in which we can tune our resonant laser). No peaks were found out of this range. We illuminated the sample with 300 µW of power while the spectrometer acquired a measurement with an exposure of 10 seconds (a relatively short amount of time compared to the optical characterization). Peaks were detected after noise removal using a similar technique as described above for the fluorescent spot detection.

5.2.2 Optical Characterization

All photoluminescence excitation (PLE) measurements in this section will refer to a pulse sequence described in Figure 5-6c. The duration of the green repump was 2 µs with a power of about 300 µW. The collection bin was 10 µs with 3 µW of resonant illumination power that could be attenuated with optical density (OD) filters. The frequency of the excitation was monitored continuously using the wavelength meter.

The first step in optical characterization was a PLE scan at high power (no attenuation with OD filters). For each ZPL peak identified, the laser was coarsely tuned to the ZPL frequency, then tuned across the full range of the Velocity laser's external cavity range (82 GHz) with a resolution of 275 MHz. This sequence was averaged 10^4 times at each frequency to ensure that the SNR is large enough to find an NV signal (Table 5.1 shows the statistics corresponding to optical and isotope recognition of our NV set).

The automated protocol roughly identified statistically relevant peaks (nearly all locations that were NVs revealed two such peaks; one for E_x and E_y). A sum of Gaussian lineshapes were fit to the data-set based on the number of peaks detected. The location and width of the peak were all recorded for use in the high-resolution scans.

Next, the high-resolution scans were performed using a low power red excitation (300 nW, obtained with an OD filter) to avoid power broadening. To account for the

	no ODMR contrast	no resolvable hyperfine	hyperfine resolved	failed	
PLE signal	59	14	36	1	**110**
no PLE signal	5	2	0	3	**10**
	64	**16**	**36**	**4**	**120**

Table 5.1: **Table Summarizing All Data for Sample A.** This table has the numeric breakdown of all NVs reported. The bold numbers indicate a particular column or row summation. NVs that resulted in an error were either due to a hardware failure during the automated protocol or a peak that was detected in one scan but could not be found again (likely due to a false-positive originally).

lower excitation power, we performed 10^6 averages. The scan range and resolution were determined by the location and width of the previous high-power scan.

Gaussian lineshapes were fit to the final low-power, high-resolution scans in the same manner as for the high-power scans. The center ZPL position is midway between the E_x and E_y transitions, and the splitting is half the distance between them.

5.2.3 Isotope Recognition

The final step in the measurement protocol is to measure a continuous-wave (CW) optically detected magnetic resonance (ODMR) that probes the NV fine structure. We determined the emitter's orientation by sweeping a strong MW field over each of the 4 possible orientations (pre-characterized prior to each run). Once determined, we iteratively lowered the MW power until the ODMR signal had resolvable hyperfine transitions (up to 10 dB lower than the power used to determine the orientation). The NV isotope was determined by inspection of the multiplicity of the number of dips in the ODMR spectrum.

Almost half of the NVs identified (showing both PLE and ODMR signals) had unidentifiable ODMR spectra. Figure 5-2 shows a summary of all identified emitters. It is important to note that the distribution of both categorized (^{14}NV and ^{15}NV) and un-categorized NVs follow the same distribution (as seen by the overlapping CDF in Figure 5-2a and the same shape of histograms in Figure 5-2b-c).

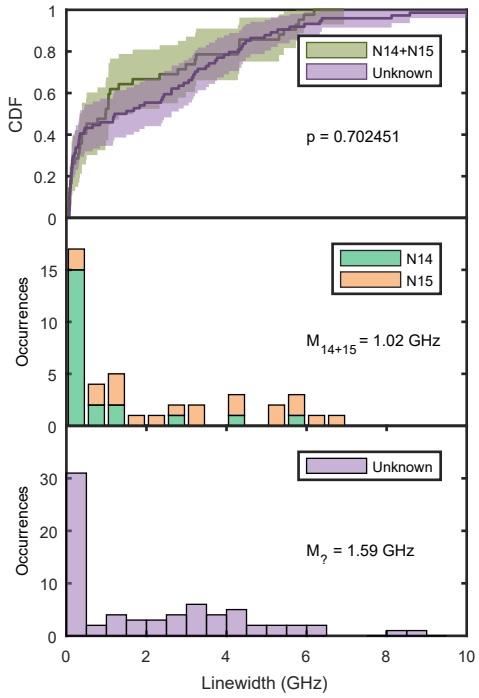

Figure 5-2: **Summary of All Data for Sample A. (a)** A CDF representing the distributions of unknown isotopes to known isotope ZPL linewidths. A similar shape indicates that both sample sets are drawn from the same distribution indicating there is no inherent bias towards sampling ^{14}NV or ^{15}NV. The probability to obtain these results if the samples are drawn from the same distribution (p) is evaluated by a Wilcoxon rank-sum test. **(b)** A stacked histogram showing the all ^{14}NV and ^{15}NV ZPL linewidths. The median linewidth (M) is indicated. **(c)** A histogram showing the linewidths for the set of ZPLs with an unknown host isotope.

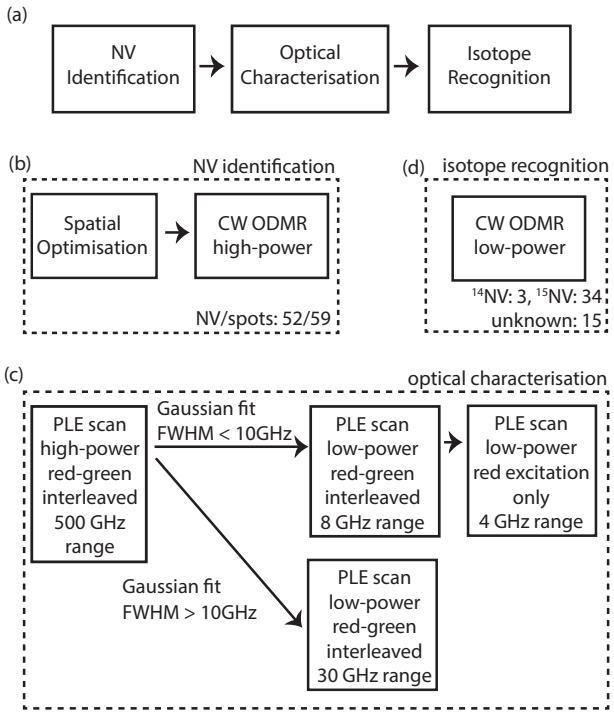

Figure 5-3: **Measurement Sequence for Sample B. (a)** The three parts of the experimental sequence: NV identification, optical characterization and isotope recognition are executed by an automated protocol. **(b)** Out of a total of 64 fluorescent spots at the implantation depth and deeper in the sample, 57 were identified as NV centers, based on a Gaussian spatial profile and the presence of an ODMR dip. 52 of these spots contained single NV centers **(c)** After a broad range scan to determine the position of the optical resonances, separate sequences are performed for very broad linewidths (>10 GHz) and the other linewidths, to restrict measurement time. Measurements probing the linewidth free from spectral diffusion (referred to as low-power red excitation only) are performed only if the linewidth was not very broad. **(d)** For each NV center, a low-power CW ODMR spectrum is taken to find the N isotope.

5.3 Delft Automation Protocol

Just as with Sample A, Sample B is maintained at a temperature of 4 K in a closed-cycle cryostat (Montana Instruments). The optical and electronic elements of the experimental setup are as previously described in Ref. [27]. Figure 5-3 schematically illustrates the measurement protocol for sample B in detail.

5.3.1 NV Identification

We identified Gaussian-shaped fluorescence locations by processing a confocal scan. At each of these locations, the instrument performs a spatial optimization in three dimensions. The automated protocol proceeded if the spot could be fit with a Gaussian shape better than some goodness of fit metric. Next, a CW ODMR measurement was performed at high microwave power. Specifically, high power was used to maximize the visibility of an ODMR dip, We fit the ODMR response to a Gaussian curve to find the resonant frequency that is to be used in the remainder of the protocol for microwave driving.

If both spatial optimization was successful and an ODMR dip was observed, the location was flagged as an NV center. Out of 52 spots identified as NV centers following this protocol, five contained two NV centers. Because a unique link between ODMR for isotope recognition and the optical linewidth could not be made, these NVs were omitted from the final analysis. NVs with both narrow and broad optical linewidths were identified in these five spots, as well as at least one ^{14}NV.

5.3.2 Optical Characterization

In this section we detail the optical characterization for sample B as described in Figure 5-6c-d.

The first step for optical characterization was to take a PLE scan at high power with interleaved red and green excitation for each wavelength step. We applied 100 nW of red power (measured before the objective) for 100 µs, followed by 100 µW green power for 10 µs and a 10 µs wait time. This sequence was repeated for a total integration time of 10 ms for each data point/wavelength step. We scanned over a range of 500 GHz, with a resolution of approximately 10 MHz.

The laser's wavelength was monitored using a wavelength meter. During all optical scans, microwave power was applied to drive the hyperfine ground states. This made all optical transitions for all spin projections visible and prevented optical pumping into dark states during the scans that probed short-timescale dynamics (the red-green

interleaved scans).

Automated protocols were used to fit a Gaussian lineshape to the PLE peaks, determining the location of the two most prominent peaks. The ZPL position is defined as the midway between these peaks and the strain splitting is half of the distance between them. No optical resonances were found for 4 NVs in the 500 GHz range scanned (between 470.3 THz and 470.8 THz) during the automated protocol. For 3 of these, optical resonances were found manually outside this range (around 469.7 THz, 470.2 THz, and 471.1 THz). For one NV, no optical lines were found in a range from 469.4 THz to 471.4 THz.

We continued with scans around the resonances, using low power resonant excitation (12 nW) to avoid any power broadening. To increase the measurement efficiency, the PLE scan parameters were dependent on the fitted linewidth in the large-range, high power scan as follows:

- If the fitted linewidth in the broad-range scan was very broad (>10 GHz), a PLE scan with interleaved red and green was subsequently carried out over a range of approximately 30 GHz. The resolution of this scan was 30 MHz. The timing of the sequence is as described for the broad-range scan.

- If the fitted linewidth was <1 GHz, we performed a single PLE scan interleaving red and green excitation for each data point over a range of 8 GHz (resolution 4 MHz and the same pattern as the broad-range scan). We next proceeded with 30 scans using just red excitation during the wavelength sweep. A green repump pulse occurred only in between each scan. The range of these scans was 4 GHz, with a resolution of approximately 4 MHz. The integration time for each pixel was 20 ms, making the duration of the full 4 GHz range approximately 40 seconds. After each scan, we performed a second scan across the resonance to determine if the NV ionized during the previous scan. We fit a Lorentzian to the non-ionized traces, and extract the FWHM, $\bar{\gamma}$, from their weighted average:

$$\bar{\gamma} = \frac{\sum_i \gamma_i \sigma_i^{-2}}{\sum_i \sigma_i^{-2}}, \tag{5.1}$$

where γ_i are the fitted FWHM of the individual traces, and σ_i the corresponding standard error of the fit parameter.

5.3.3 Isotope Recognition

The final step in the measurement protocol was an ODMR scan probing the NV's fine structure. This was accomplished by scanning around the resonance detected during the NV identification in the first step. Similar to the optical measurement, we attenuated the microwave power by 7 dB relative to the ODMR measurement during NV characterization to avoid power broadening. We could then determine the NV isotope by inspection of the multiplicity of the number of dips in the ODMR spectrum, and confirmed by the best goodness of fit out of fits with Gaussian dips with hyperfine splittings fixed to the ^{14}NV or ^{15}NV known values. The isotope could not be reliably identified by inspection in 15 NV centers located at the implantation depth. We note that these contained both NV centers with broad (>500 MHz, 13 NVs) and narrow (<500 MHz, 2 NVs) linewidths.

Table 5.2 shows a summary of the PLE and ODMR contrast for spots at the implantation depth and deeper in the diamond. In 5-4 a summary of the optical linewidths is shown, including the NVs with unknown isotopes. Similar to the observations for sample A, we find that the cumulative density function for the unknown isotopes and the combined ^{14}NV and ^{15}NV data overlap.

5.4 Results

To distinguish NVs formed by implanted nitrogen atoms from those formed by native nitrogen atoms, we implanted ^{15}N isotopes [130]. We then experimentally correlated the optical linewidth to the nitrogen isotope. The study was carried out on two separate samples as described in Section 5.1. Sample A (processed at MIT) is a bulk ⟨100⟩ CVD grown diamond (Element 6), prepared with the same implantation and annealing procedure as presented in Chu et al. [35]: it was implanted with $^{15}N^+$ at 85 keV with a fluence of 10^9 N/cm^2 and subsequently annealed at a maximum temperature

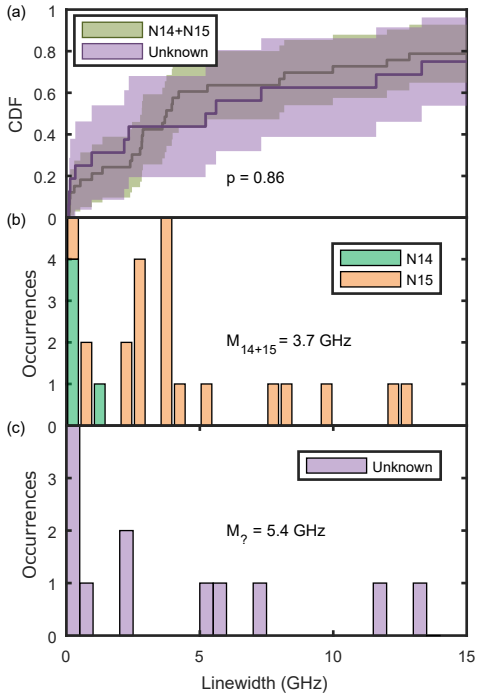

Figure 5-4: **Summary of All Data for Sample B. (a)** A CDF representing the distributions of unknown isotopes to known isotope ZPL linewidths. A similar shape indicates that both sample sets are drawn from the same distribution indicating there is no inherent bias towards sampling ^{14}NV or ^{15}NV. The probability to obtain these results if the samples are drawn from the same distribution (p) is evaluated by a Wilcoxon rank-sum test. **(b)** A stacked histogram showing the all ^{14}NV and ^{15}NV ZPL linewidths. The median linewidth (M) is indicated. **(c)** A histogram showing the linewidths for the set of ZPLs with an unknown host isotope. Data for 7 ^{15}NV and 4 NVs with unknown isotope are not shown as they are out of the 15 GHz range.

	PLE signal	no PLE signal	
ODMR isotope resolvable	35	0	**35**
ODMR isotope unresolvable	16	1	**17**
no ODMR contrast	1	4	**5**
	51	**5**	**57**

Table 5.2: **Table Summarizing All Data for Sample B.** This table has the numeric breakdown of all fluorescent spots reported, at the implantation depth (52 spots) and deeper in the diamond (5 NVs). Not included are two data points for which spatial optimization was not successful, and 5 spots that contained more than one NV. The bold numbers indicate a particular column or row summation.

of 1200°C. Sample B (Delft) is a membrane (thickness ≈ 14 µm) obtained from a bulk ⟨100⟩ CVD grown diamond (Element 6), implanted with $^{15}N^{+}$ at 400 keV (fluence 10^8 N/cm^2), and subsequently annealed at a maximum temperature of 1100°C.

During implantation, nitrogen ions penetrate the diamond to a depth determined by the implantation energy (Figure 5-5). As implanted nitrogen atoms track through the crystal, they displace carbon atoms from their lattice sites creating vacancies. The nitrogen atoms create damage along the entire trajectory, but the damage is greatest near the stopping point [44]. We performed SRIM [191] simulations to predict the stopping point of implanted ^{15}N atoms, in addition to the locations of vacancies created along the trajectory (Figure 5-5b). At temperatures >600°C, vacancies become mobile [43]. These vacancies can form an NV center, recombining with the implanted ^{15}N that created the damage or with a native ^{14}N in the lattice. The resulting ^{15}NV and ^{14}NV formation yields can vary significantly [62, 107, 170, 115, 186] depending on several factors, including the initial nitrogen concentration, the implantation fluence and energy, the number of vacancies created during the implantation process, and the duration and temperature of annealing.

A representative confocal fluorescence map at the implantation depth in sample A is shown in Figure 5-6a. Confocal fluorescence scans at foci deeper into the diamond

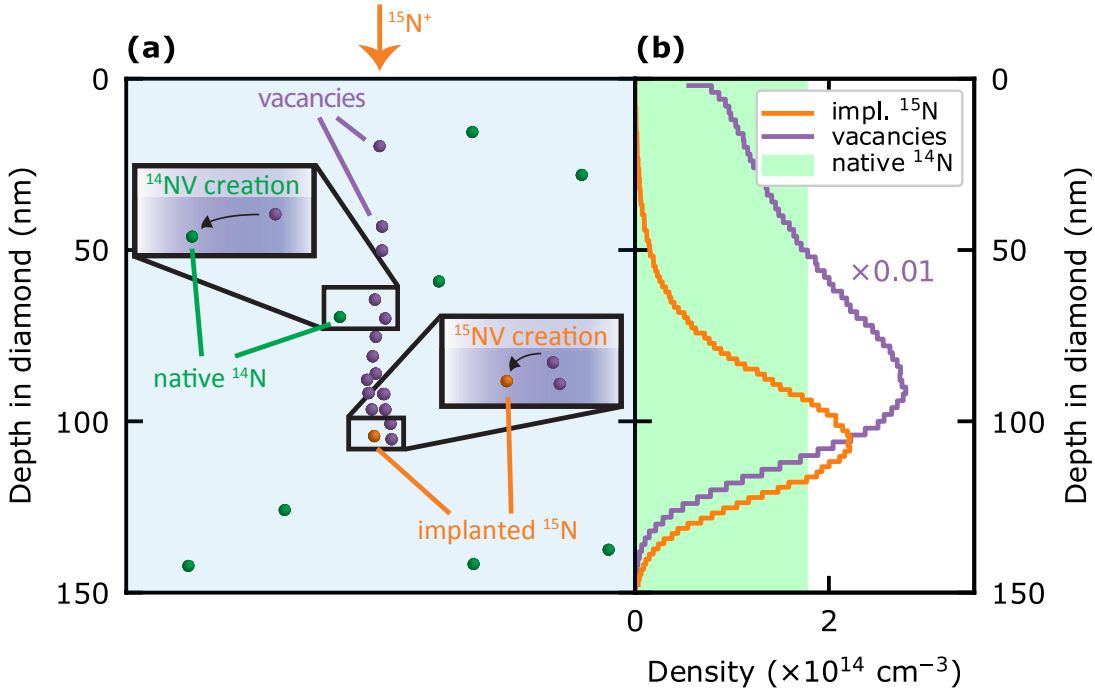

Figure 5-5: **NV Creation via Nitrogen-Ion Implantation. (a)**, Schematic showing implanted $^{15}N^+$ ions (orange) leaving a trail of vacancies (purple) until settling into a final position. Naturally abundant ^{14}N ions (green) are shown randomly distributed throughout the diamond lattice. Vacancies (implantation-induced or native) mobilized by annealing can bind to a nitrogen atom (implanted or native). **(b)**, A SRIM simulation using the parameters in sample A shows the distribution of implanted nitrogen (orange) and created vacancies (purple). The shaded green area indicates the range of the estimated natural ^{14}N concentration reported by Element 6.

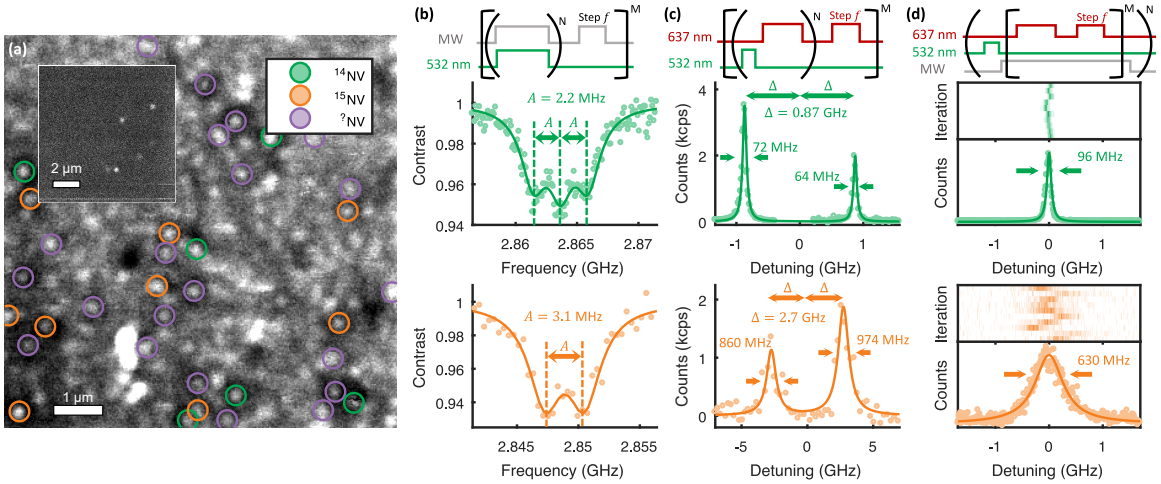

Figure 5-6: **Isotope Characterization and Optical Measurements of NV Centers from ^{14}N and ^{15}N. (a)**, A fluorescent confocal scan of sample A taken at 4 K, with labels indicating NV centers characterized as ^{14}NV, ^{15}NV, and a set with unresolvable hyperfine lines, labeled as $^{?}$NV. A scan a few microns below the implanted layer (inset) shows a lower NV density. **(b-d)**, Pulse sequences (top row) used for isotope characterisation and optical measurements, and representative measurement results for each isotope (green, middle row: ^{14}NV, orange, bottom row: ^{15}NV). **(b)**, Continuous wave ODMR measurements reveal the NV isotope. The ^{14}NV is characterized by $S = 1$ hyperfine transitions; the ^{15}NV by $S = 1/2$ hyperfine transitions. **(c)**, Interleaved red and green excitation probe the combined effect of short-timescale fluctuations and laser-induced spectral diffusion. The E_x and E_y ZPL transitions are visible for both isotopes; the ^{14}NV linewidths are narrower and show a smaller strain splitting than the ^{15}NV. **(d)**, Individual line scans of the ZPL in sample B reveal the linewidth free from laser-induced spectral diffusion. The summation of many repeated scans is broadened as a result of repump-laser-induced spectral diffusion.

show a significantly lower density of fluorescent spots (Figure 5-6a, inset), indicating that the emitters near the surface were predominantly created by the implantation and annealing process. We identified emitters using different protocols in the two samples. In sample A, automated spot-recognition was performed on a fluorescence scan. For each detected spot we identified an NV center based on its characteristic zero-phonon line (ZPL) emission around 637 nm using a spectrograph from a photoluminescence measurement at 4 K under 532 nm excitation. This protocol identified 120 fluorescent spots as NV centers in a ≈ 400 µm^2 area. In sample B, spots in a fluorescence scan were detected visually, after which an automated protocol identified NV centers based on the presence of a resonance in an optically detected magnetic resonance (ODMR) spectrum around the characteristic NV center zero-field splitting of 2.88 GHz. In this way, 52 out of a total 57 inspected spots in a ≈ 75 µm^2 area in the implantation layer were identified as NV centers.

We next determined the nitrogen isotope of each NV center by observing the hyperfine structure of the ODMR spectra. A weak external magnetic field ($B_{\|} \approx$ 5-10 G) was applied to separate the $m_s = -1$ and $m_s = +1$ electron spin transitions. We found NV centers with the characteristic triplet splitting of the ^{14}NV (with hyperfine splitting, $A = 2.2$ MHz) as well as with the ^{15}NV doublet ($A = 3.1$ MHz) [51], as indicated in Figure 5-6b. Of the 120 NVs identified on sample A, an ODMR signal was detected in 50, out of which 18 were ^{15}NV, 18 ^{14}NV, and there were 14 in which the isotope could not be reliably determined from the ODMR spectra. Similarly, of the 52 NVs identified on sample B, 34 were ^{15}NV, 3 were ^{14}NV, and the isotope could not be determined in 15 NVs. We attribute the different isotope occurrence ratios in sample A and B to different native ^{14}N content and different implantation fluence.

Subsequently, we measured the linewidth of optical transitions of identified NV centers, recording photoluminescence excitation (PLE) spectra at low temperature (≈ 4 K). A tunable laser with a wavelength near 637 nm was scanned over the optical transition while detecting emitted photons in the phonon-sideband. We performed two types of measurements. First, a scan was made in which resonant excitation (637 nm) and green illumination (532 nm) were rapidly interleaved at each data

point. The red excitation causes rapid optical spin pumping and ionization of the NV center. The green excitation provides repumping into the negative charge state and the $m_s = 0$ spin state. This measurement reveals the combined effect of short-time scale fluctuations and repump-laser-induced spectral diffusion in broadening the transition linewidth. Examples of the resulting traces are seen in Figure 5-6c.

Second, in sample B, an additional scan was performed to isolate the effect of short timescale fluctuations from repump-laser-induced diffusion. A single off-resonant repump was applied before sweeping the resonant laser at low power, as seen in Figure 5-6d. We applied microwaves on the spin resonances to prevent optical pumping into a dark spin state during the sweeps [165]. Remaining traces in which the NV center ionized were excluded by applying a second scan over the resonance to check the charge state. If no resonance was observed, the preceding trace was disregarded. This scanning protocol was repeated many times to probe spectral diffusion through the resulting spread of the observed lines [61]. To extract the linewidth free from repump-laser-induced spectral diffusion, we performed a weighted average of linewidth values found from Lorentzian fits to each individual scan.

Figures 5-6c and d display representative resonant optical scans for the ^{14}NV and ^{15}NV centers, each showing two resonances corresponding to the two $m_s = 0$ orbital transitions E_x and E_y. Notably, while the ^{14}NV center (green, top row) exhibits a narrow optical linewidth with a full-width-at-half-maximum (FWHM) of 64 ± 4 MHz, the ^{15}NV linewidth (orange, bottom row) is broad, with a FWHM of 860 ± 236 MHz. The dynamics in the second scan type (Figure 5-6d) indicate that both repump-induced fluctuations and a short-timescale mechanism broaden the ^{15}NV linewidth, but that repump-induced fluctuations are dominant in broadening beyond 200 MHz as seen in Figure 5-9.

To correlate the occurrence of narrow optical linewidths with the N isotope of the NV centers, we acquired an extensive data set using the data accumulation procedures described above. The resulting distributions of optical linewidths for both N isotopes are shown in Figure 5-7. Narrow optical linewidths in both samples can be attributed almost exclusively to NVs with a native ^{14}N host. In contrast, ^{15}NV centers exhibiting

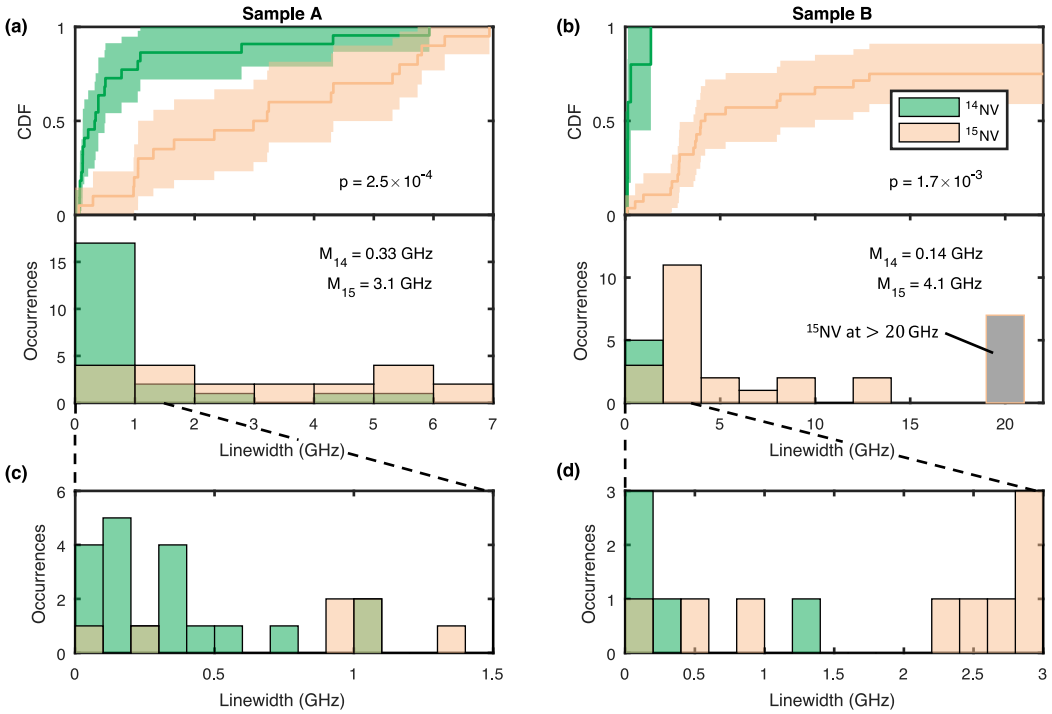

Figure 5-7: **Optical Linewidths per Isotope. (a-b)**, A summary of the optical linewidths identified in sample A **(a)** and sample B **(b)** from scans at the implantation depth. For sample B, that has comparatively few ^{14}NV centers at the implantation depth, we included three ^{14}NV centers found deeper in the diamond to enable a comparison between NVs formed from implanted versus native nitrogen. The distribution is represented as a cumulative distribution function (CDF, top), with the corresponding histogram shown below. The shaded region in the CDF indicates a 95% confidence interval calculated using Greenwood's formula. These data show that both diamonds supported narrow-linewidth NV centers, the majority of which originated from ^{14}NVs. While ^{15}NV do exhibit narrow lines, their median linewidth (M) is higher than for the ^{14}NV centers in both samples. We evaluate the probability to obtain the observed linewidths for ^{14}NV centers and ^{15}NV centers if the samples are drawn from the same distribution with a Wilcoxon Rank Sum test, finding a p-value of 2.5×10^{-4} in sample A and 1.7×10^{-3} in sample B. **(c-d)**, A magnification of the histograms shown in **(a)** and **(b)**.

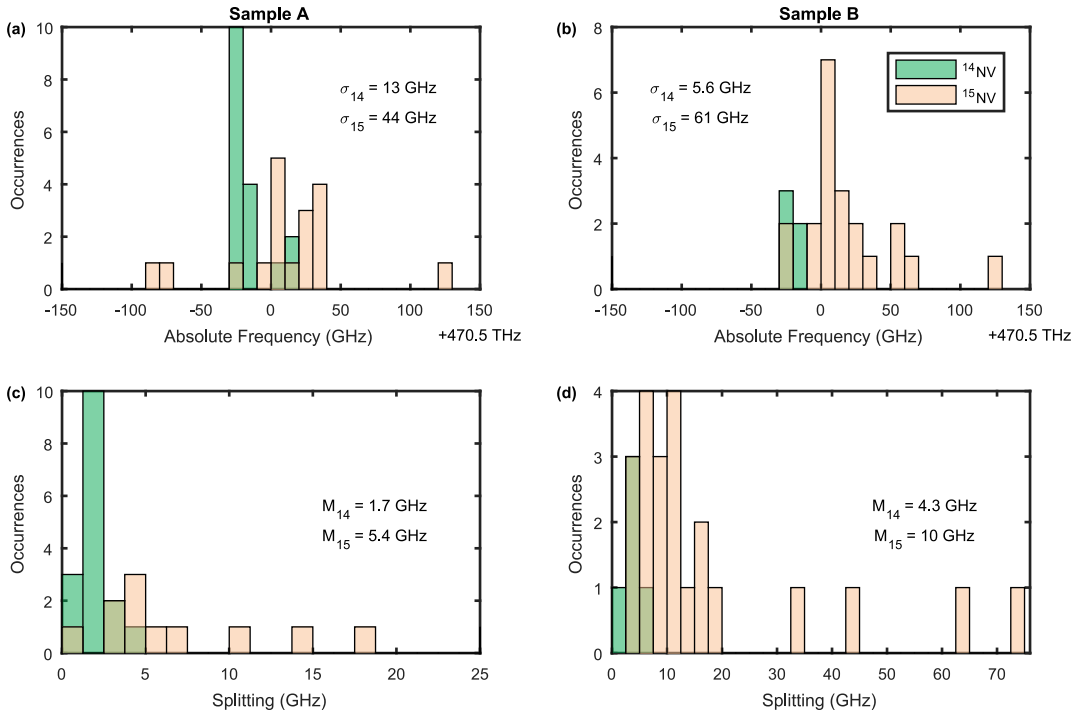

Figure 5-8: **Strain Analysis. (a-b)**, The distribution of axial strain (measured by absolute average ZPL frequency) in NVs acquired from analysis of sample A **(a)** and sample B **(b)**. The ^{15}NV ZPLs exhibit a larger spread in axial strain (standard deviation, σ) than the ^{14}NV ZPLs. **(c-d)**, The distribution of transverse strain (measured by half the splitting between E_x and E_y frequencies) in NV centers of sample A **(c)** and sample B **(d)**. The ^{15}NV ZPLs show a greater median splitting (M) in both samples.

narrow optical linewidths are extremely rare, with a median linewidth for ^{15}NV centers of 3.1 GHz in sample A and 4.1 GHz in sample B.

Notably, in both data sets one NV center with a ^{15}N host was found that showed narrow optical linewidths (< 100 MHz). Given their low occurrence and the non-zero natural abundance of ^{15}N, the creation mechanism of these narrow-linewidth ^{15}NVs cannot be conclusively determined. Nevertheless, their presence demonstrates that ^{15}NV centers can exhibit coherent optical transitions. Therefore, we conclude that the difference in distribution of optical linewidths between ^{14}NVs and ^{15}NVs is not due to an intrinsic effect related to the isotope itself, but due to differences in the local environment resulting from the implantation process.

Damage due to implantation may cause local strain fields. Axial strain results in an overall shift of the optical transition, while transverse strain will split the E_x

and E_y transitions [51]. The distributions characterizing the strain for both NV isotopes are shown in Figure 5-8. The spread of the distribution in ZPL detuning representing axial strain for ^{15}NVs (44 GHz for sample A, 60 GHz for sample B) is wider than for ^{14}NVs (13 GHz for sample A, 5.6 GHz for sample B). Further, we found that ^{15}NVs exhibit higher transverse strain, manifested by greater splitting with a median of 5.4 GHz (10 GHz) compared to 1.7 GHz (4.3 GHz) for ^{14}NVs in sample A (B). Assuming a similar strain susceptibility for both isotopes, these results indicate that local damage around the implanted ^{15}NVs creates a more strained environment, providing further evidence that implantation-induced local damage is responsible for the broadened ^{15}NV linewidth. In addition, in both samples we observed a shift of the average ZPL frequency for ^{15}NV compared to ^{14}NV ZPLs, possibly due to an intrinsic dependency of the energy levels on the isotope as observed in other color centers [49, 55].

5.5 Characterization of Spectral Diffusion

On sample B we performed scans to isolate short timescale fluctuations from repump laser-induced spectral diffusion (Figure 5-6(d)).

For each NV center we performed 30 consecutive scans, with a green repump laser pulse applied only in between the scans. The scans in which the NV center did not ionize are selected. We fit a Lorentzian curve to the resonance in each scan and calculate the weighted average for each NV center (see Eq. 5.1). We also fit the sum of the scans with a Gaussian curve, extracting the FWHM including repump laser-induced spectral diffusion. When correlating the two analyses, as shown in Figure 5-9, we find that the Lorentzian linewidths are mostly less than 200 MHz, while further broadening in the linewidth can be attributed to laser-induced spectral diffusion.

Protocols using resonant charge repumping [157] and real-time monitoring of the transition frequency [68] have been used to reduce linewidths broadened to $<$200 MHz by slow spectral diffusion. However, for larger broadening, and especially for the very broad ($>$1 GHz) linewidths for ^{15}NVs, such a repump scheme is challenging because

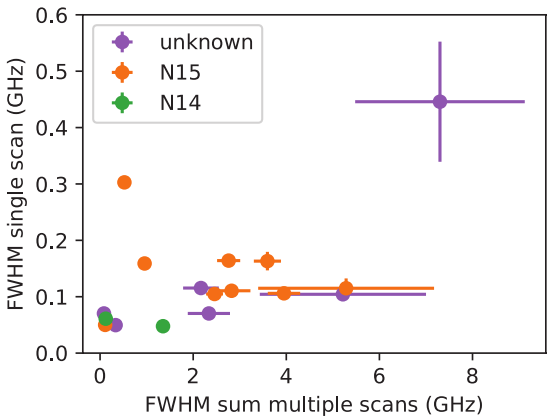

Figure 5-9: **Optical Linewidths from Scans with Red Excitation Only.** Consecutive scans over a single resonance are performed as described in the text. The FWHM of the optical linewidth in individual scans (y-axis) is correlated to the FWHM of the summed scans including repump laser-induced spectral diffusion (x-axis). We conclude that the Lorentzian linewidths are mostly less than 200 MHz, while further broadening in the linewidth can be attributed to laser-induced spectral diffusion. This figure contains data for NV centers at the implantation depth with linewidths <10 GHz (Figure 5-3).

the transition can shift dramatically, making locating the new transition resonances difficult within an acceptable time.

5.6 NV Densities

In sample A (see confocal scans in Figure 5-6a), the NV areal densities estimated from the verified isotopes at the implantation depth are at least 3.9×10^{-2} ^{14}NVs/µm^2 and 3.5×10^{-2} ^{15}NVs/µm^2. When assuming that the isotope distribution over the NVs with unknown isotope follows the same distribution as for the known NVs (this assumption is supported by the overlapping linewidth distributions in Figure 5-2), the areal density estimates are 5.1×10^{-2} ^{14}NVs/µm^2 and 4.7×10^{-2} ^{15}NVs/µm^2. This corresponds to a conversion efficiency of implanted ^{15}N to NV of approximately 3.5%-4.7%.

At a scan deeper in the sample over the same area (Figure 5-6a, inset) we found 3 NVs, that we assume to be ^{14}NV given their location in the diamond well below the implantation depth. The native areal density of ^{14}NVs that we estimate from this is

3×10^{-2} ^{14}NVs/µm^2.

Confocal scans of sample B are shown in Figure 5-10, at the implantation depth and deeper into the sample to illustrate the change in NV density due to implantation.

The confocal scan at the implantation depth (∼400 nm, Figure 5-10a) displays around ∼180 fluorescent spots. We characterized 59 of these spots from the highlighted region in Figure 5-10a, identifying 57 NV centers (47 single NVs in a confocal spot and 5 spots with two NVs). We are able to determine the isotope for 37 NVs, 3 out of which are ^{14}NVs, and 34 are ^{15}NVs. From this, a lower-bound estimate of the ^{14}NV areal density after implantation is 4×10^{-2} ^{14}NVs/µm^2. We estimate the ^{15}NV areal density to be at least 5×10^{-1} ^{15}NVs/µm^2. When assuming that the unknown isotopes follow the distribution of isotopes for the known isotopes (as for sample A, this is supported by the overlapping linewidth distributions in Figure 5-4), the areal density estimates are 6×10^{-2} ^{14}NVs/µm^2 and 7×10^{-1} ^{15}NVs/µm^2. This corresponds to an estimated conversion efficiency of implanted ^{15}N to NV of approximately 50%-70%. We attribute differences in conversion efficiencies between sample A and sample B to the difference in implantation parameters [122].

We characterized 5 out of 6 bright fluorescent spots in the deep scan (≈ 5 μm depth, Figure 5-10b). All 5 spots were identified as NVs, and all displayed narrow linewidths in the red-green interleaved scan. The isotopes were found to be ^{14}N for 3 out of 5 NVs, whereas the isotope could not be reliably determined from the ODMR measurement for 2 NVs (this is a comparable ratio of known versus undetermined isotopes as at the implantation depth). Because their location in the diamond was well below the implantation depth, these findings strongly suggest that these fluorescent spots are naturally occurring ^{14}NV. A best estimate of the ^{14}NV areal density before implantation is therefore 3×10^{-2} ^{14}NVs/µm^2.

Although the sample sizes are small, comparing the estimated ^{14}NV densities at the implantation depth and deeper in the diamond we find indications that ^{14}NVs at the implantation depth are created during implantation in both sample A and B.

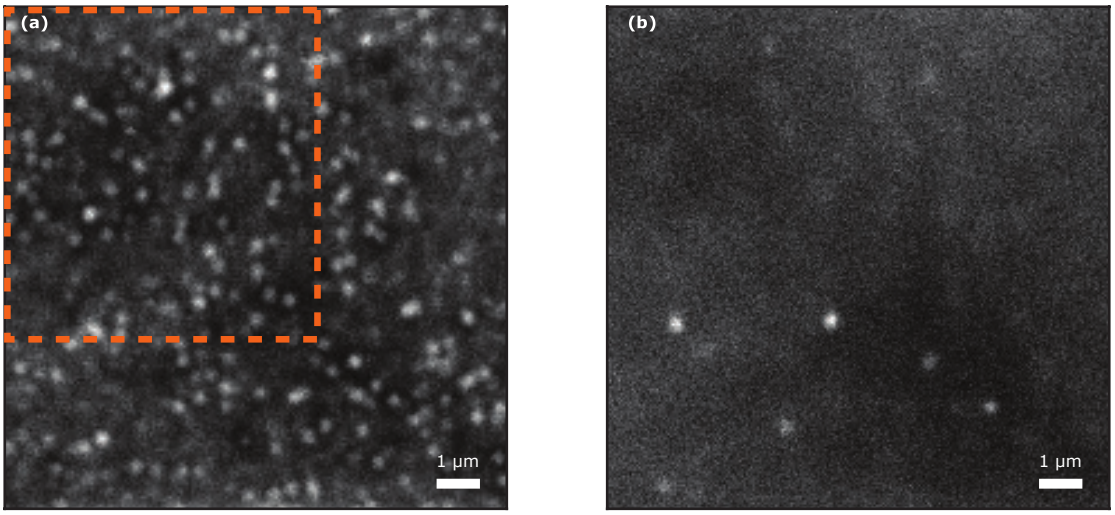

Figure 5-10: **Confocal Scans of Sample B. (a)** A scan at the implantation depth and **(b)** at ∼5 µm under the diamond surface. The orange box indicates the approximate region at the implantation depth in which fluorescent spots were characterized.

5.7 Outlook

Data acquired here show indications of an increase in ^{14}NV density in the implantation layer in both samples as discussed in Section 5.6. We hypothesize that these ^{14}NV centers can be formed from naturally occurring nitrogen combining with vacancies created during implantation. Since they can be located at greater distances from the main damage centers near the stopping point of the nitrogen track, these NV centers may be coherent and usable for quantum information purposes, although more work will be necessary to determine a statistically significant correlation. It is the case, however, that the positioning accuracy of these NVs at the device depth would be significantly lower because their spatial distribution is determined by arbitrarily positioned naturally occurring nitrogen in combination with the diffusion length of the vacancies generated during implantation.

In summary, the implanted nitrogen atoms yield NV centers with predominantly broad optical lines ($>$ 1 GHz) and substantially higher strain than NV centers formed from native nitrogen. These results indicate that implanted nitrogen atoms combined with an annealing process at high temperatures do not routinely produce NV centers with narrow optical linewidths. Vacancies produced in the implantation process may

combine with existing nitrogen atoms to produce narrow NVs, but more work will be necessary to determine a statistically significant correlation. It is clear from this work that recipes for generating implanted NV centers should be reinvestigated, addressing local lattice damage associated with implanted nitrogen. In addition, other approaches for precisely controlling the NV centers' positions while causing minimal local damage can be further explored, such as employing 2D nitrogen-doped diamond layers combined with electron irradiation or ion implantation for vacancy production [117, 116] or laser writing strategies for creating vacancies with 3D accuracy [33, 32].

Chapter 6

Closing the Design Loop: Process Control and Device Integration

Until now, I have presented detailed explanations and analyses of work performed to explore novel registers and build statistically significant data sets along with the infrastructure and tools that made it possible. Now, I want to take advantage of the full capabilities our infrastructure enables. In Chapter 5, statistics were used to discover properties of our implantation technique on qubits that were not previously known. At this point, however, qubits in the diamond exist and I can *correlate* changes to their properties through all of the processing steps — something that has not been analyzed in a statistically significant manner in previous studies. This additional capability will enable process control of our engineered devices.

Work in this area, work that is underway in the Quantum Photonics Lab (directed by Dirk Englund), is focused on the development of an operational device fully capable of acting as a quantum repeater in a larger network. The design process to achieve this goal is illustrated in Figure 6-1. Every step is enabled at scale due to the automated framework and infrastructure discussed as part of this thesis (see Chapter 2). I have shown that lattice bombardment during ion implantation (step 2, "Qubit Production" in Figure 6-1) may be the culprit when considering the lower optical coherence observed in implanted NVs as discussed in Chapter 5. As a result, we are considering other techniques for the incorporation of nitrogen in the diamond

growth process, or the development of novel annealing recipes as envisioned by Ian Christen (Quantum Photonics Lab).

Over the course of my graduate program, I have successfully demonstrated registration at a chip level scale (cf. Figure 2-6 bottom right). Using the registration process, a device yield (defined as the ratio of single-NV-coupled devices to the number of fabricated devices) of 29% was achieved, significantly higher than the yield of a process without emitter registration [183]: the NV's circular target cross section of the parabolic reflector (100 nm below the top of the parabola) has a radius of 250 nm, resulting in an area of just under 0.2 μm^2. Given an implantation dose of 10^9 $^{15}N/cm^2$, and assuming a yield of approximately 1%, the NV density is expected to be in the neighborhood of 0.1 NV/μm^2. This would result in an approximately 2% chance of an NV populating the non-etched portion of the diamond that forms the parabola. This probability is a higher bound because it is assumed that all NVs fell at this depth, and any NV, regardless of lateral position, is coupled to the parabolic optical mode. The next step in this process is the creation of a fully integrated device.

6.1 Screening Through Fabrication

I have also shown how qubit production affects emitter performance, a finding that led to the investigation of new and improved production techniques. The next step in the process that we know has a significant impact on emitters is fabrication. Emitters that are measured in fabricated structures have optical linewidths many GHz wide, while their bulk counterparts are measured on a hundreds of MHz scale. We believe this is most likely due to shallow damage induced in nearby surfaces. Anticipating efforts to isolate fabrication effects, it is first necessary to isolate our cleaning and annealing steps.

6.1.1 Samples and Processing

The experimental configuration associated with the NV optical measurements will be identical to those discussed in Section 4.2, where all optical measurements are taken

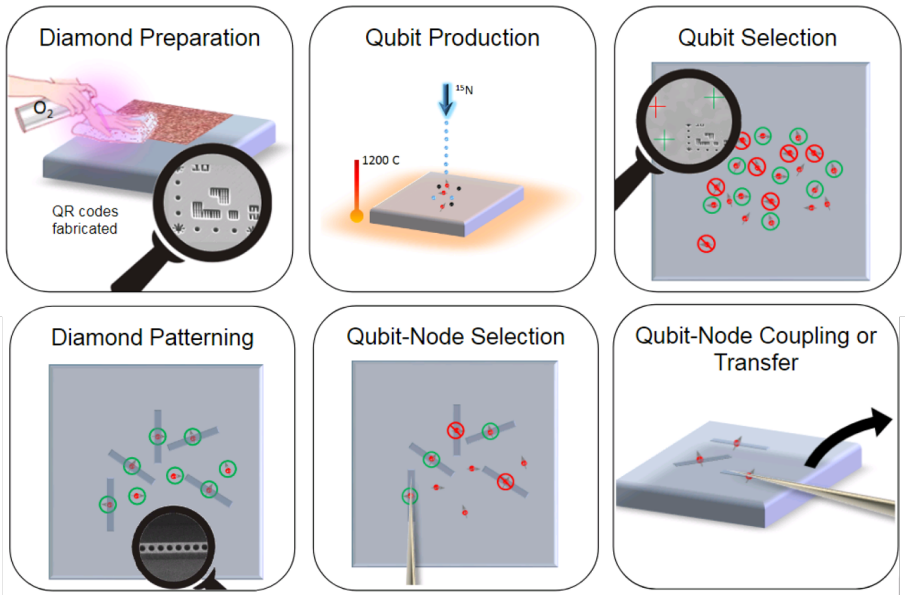

Figure 6-1: **Process Summary.** Reading from left to right, top to bottom. 1) The diamond is prepared by cleaning the surface and patterning the coordinate system markers. 2) The defect centers are created by ion implantation followed by annealing. 3) Defect centers are localized and characterized. 4) Structures to enhance light-matter interaction are patterned around localized centers. 5) Structure-defect nodes are recharacterized. 6) The best nodes are transferred to a new host chip.

at cryogenic temperatures of around 4 K. At this point in time, four measurements have been made:

1. First Cold. Here, the sample had been stored in the sample box in an atmosphere environment for roughly 8 months.

2. Pre-acid clean. This run serves as a control and changes from the "first cold" are not expected. This will also serve as the data set exhibiting NV properties just prior to the acid clean. This was acquired approximately 1 month after the previous run.

3. Post-acid clean. This experimental run was initiated as soon as possible following retrieval of the sample from the acid clean protocol to minimize the time the sample spent in atmosphere.

4. Post-O_2 bake. The sample was quickly transferred from the previous run to the furnace. The sample was baked in an atmosphere environment at 465°C for

4 hours [60]. Immediately following the bake, the sample was transferred back to the cryogenic setup, again to minimize time spent in atmosphere.

I am interested in extracting three specific parameters from the optical PLE scans: 1) optical transition linewidth, 2) ZPL central position, and 3) ZPL splitting. All of these properties are defined in more detail in Section 5.2.2. It is important to note that the linewidth property is a delicate experimental parameter because of the ease with which it may become power-broadened. As with the results from Chapter 5, the power was carefully adjusted to avoid entering a power-broadening regime. Unfortunately, this was not the case for the first cool down "First Cold," as is readily apparent in Figure 6-4b and d.

Using the localization techniques and infrastructure discussed in Chapter 2, a couple of hundred NVs were targeted for measurement during each experimental run. This number is reduced on each run if the algorithm is unable to find a particular NV again because of focusing issues or time constraints. In the end, a set of 131 NVs were successfully measured for each experimental run. The map of these NVs in the on-chip coordinate system can be seen in Figure 6-2. Sixteen sites were measured more than once during the same run (probably due to the slight overlap in confocal scan regions) and were thus excluded from the analysis to avoid double-counting NV sites.

6.1.2 Results

Generally, the diamond processing steps performed prior to fabrication are expected to improve the NV's optical properties. Specifically, the enhancement translates to the narrowing of the inhomogeneous distribution of ZPL positions (e.g. reducing the distribution of axial strain experienced by each NV), reducing the E_x to E_y splitting (corresponding to reducing the distribution of transverse strain experienced by each NV), and reducing the linewidth of the optical transitions (physically corresponding to reducing decoherence between the ground and excited states). As discussed in earlier chapters, the tri-acid clean is implemented in an effort to remove any graphitization

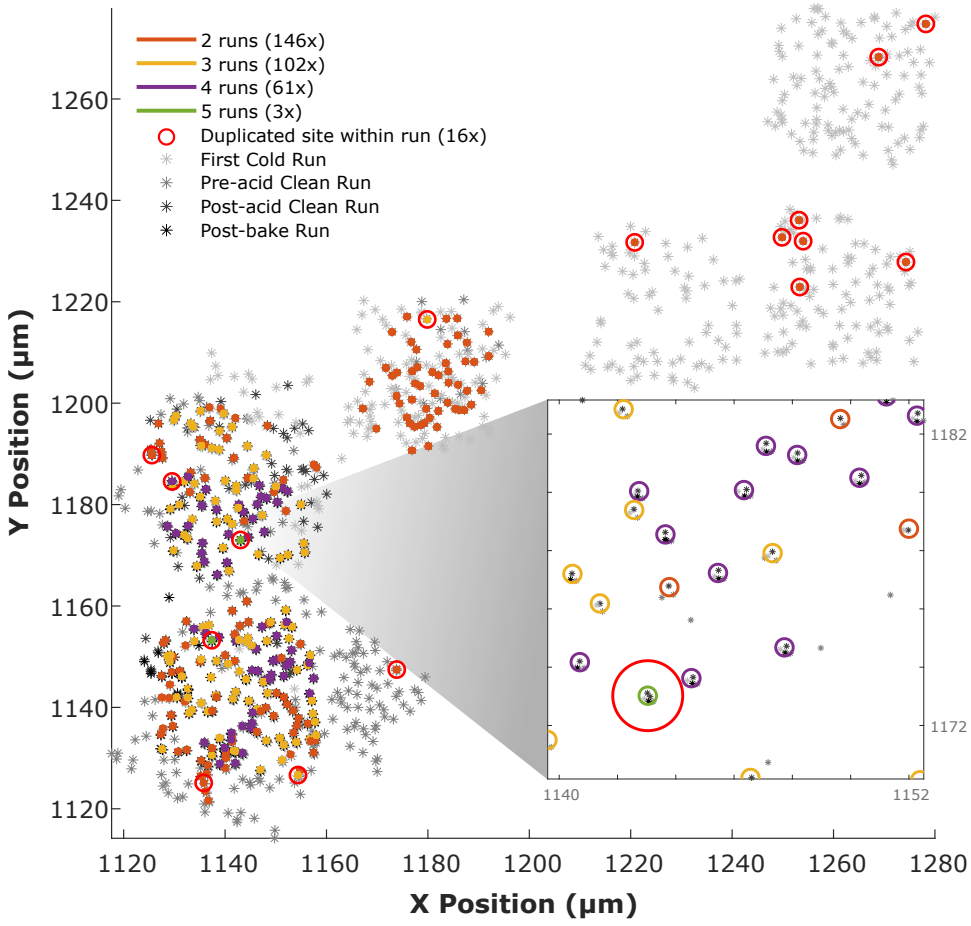

Figure 6-2: **NV Spatial Map.** A spatial map of a compiled set of runs across all of the experimental runs. Each experimental run will have many different field-of-view sites, which are each a unique color in the scatter plot. A clustering algorithm is used to detect the sites that were repeatedly found (in 2, 3, 4, or 5 runs — as labeled in the key). Sites that were duplicated within the same run are flagged with a red circle. Due to time and resource constraints in the experimental setup, the focus was placed on sites located in the lower left region.

that has occurred on the diamond surface, and the 465°C bake helps repair lattice damage caused by implantation and fabrication. Immediately after the bake, in our view, dangling sp^3 hybridized bonds can be found on the surface of the diamond, and an increase in noise due to unexpected surface states that are created dynamically [60] is expected.

A set of automated alignment techniques to overlay the multiple runs was used. The first stage of this alignment uses the QR registration taken from "reflection" confocal scan in which the sample in a widefield technique is illuminated and the reflected light is collected in the same manner as our standard fluorescence scan. This procedure alone fails to achieve the accurate registration because spherical aberration transforms the imaged positions of the location markers to their actual position. Rather than trying to correct this aberration, the constellation patterns are aligned assuming the majority of nearest-neighbors of the detected peaks are not false-positives. Finally, after running a clustering algorithm with a euclidean threshold distance of a diffraction-limit, a median spatial accuracy (standard deviation of distances from the cluster's center) within clusters of 58 nm (mean of 67 nm) was observed.

In control measurements, the distribution of the ZPL's central position, as well as splitting, both broaden as seen in Figure 6-4c. This prompted a closer inspection of the temporal behavior of a single, relatively narrow transition over many hours. As seen in Figure 6-3, it is possible to observe a transition perform a random-walk in frequency beyond its linewidth on the timescale of hours superimposed to some shorter timescale random-walks. While this is an important issue, and should not be overlooked, it can be tabled for future investigation.

Perhaps more intriguing (also apparent in Figure 6-4c), is the movement of ZPL's position into a bimodal distribution in the post-acid clean data set. It is also interesting to note that the distribution in the splitting of these transitions does not appear to be uniform between the lower and higher energy ensembles. It is likely that the observed change in ZPL position and splitting can be attributed to a spatially-uniform change in the strain tensor across the diamond. Chapter 5 discusses how these lines behave with different axial and transverse strain environments.

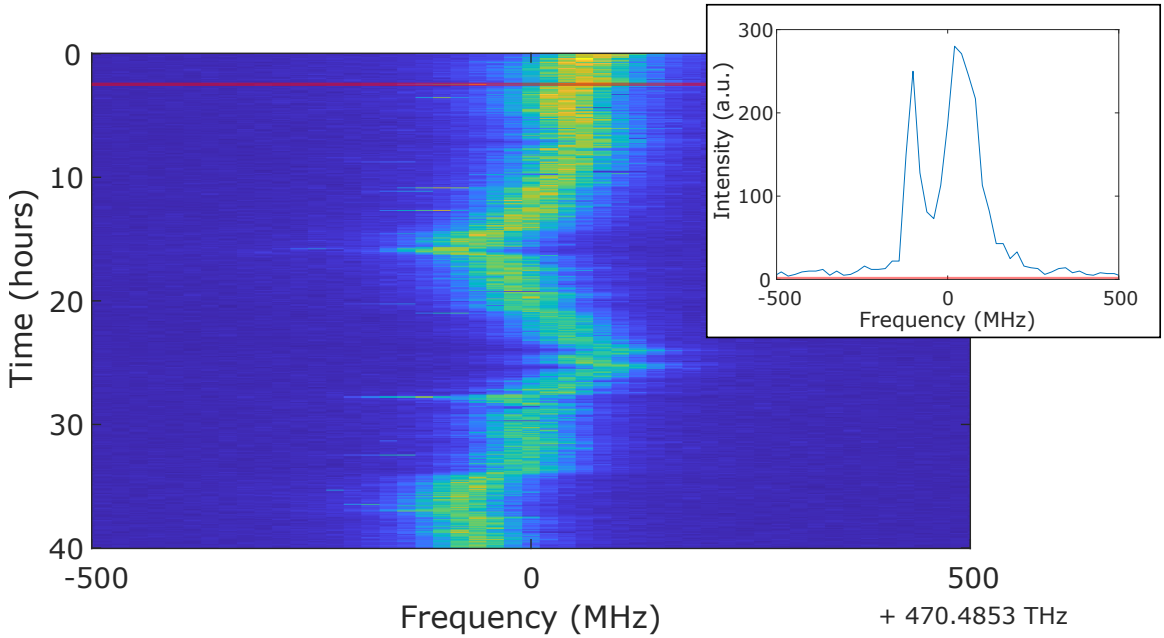

Figure 6-3: **NV ZPL Transition Dynamics.** Continuously repeated PLE sweeps over the course of 2 days. This was performed on a particularly high quality optical transition (narrow linewidth). The frequency of this transition can be seen drifting in a random walk of a few linewidths. Occasionally, this transition exhibits a bistability as shown in the inset slice. The inset slice is highlighted with a semi-transparent red line in the main figure. Slowly varying fields giving rise to this phenomenon are intriguing in and of themselves and, it can be argued, warrant independent investigation. This suggests that there are multiple timescales at which the random walks take place. The fastest of these timescales will dephase the transition making it broader than its lifetime limit, and the slower random walks manifest as spectral diffusion.

Finally, Figure 6-4d shows a marginal improvement of transition linewidth as a result of acid cleaning. This is not entirely unexpected, as acid cleaning removes a graphitic surface, however I believe that this can be improved upon significantly with a properly terminated diamond surface as discussed above. On the other hand, we see a large increase in the linewidths after performing the O_2 bake. This is not entirely unexpected due to an unpassivated surface as discussed above.

While I do not have data to support this position at this point in time, our expectation is that the increased dynamics on the surface can be remedied by implementing an additional Piranha clean. The diamond surface contains a mixture of sp^2 and sp^3 hybridized carbon. The radical oxygen in Piranha that dissociate from hydrogen peroxide are unstable and highly reactive, thus attacking the dangling bonds to form stable carbonyl (C3=O) groups at the surface [158, 142].

6.1.3 Next Steps

The current goal is to perform a thorough, statistically oriented study to determine how emitters are affected in a variety of etching processes. To accomplish this, the same set of emitters must be characterized before and after fabrication at varying distances from etched surfaces. Proposed structures are outlined in Figure 6-5. They are selected to investigate how the different crystal facets, and combinations thereof, may impact the optical coherence of the NVs as a function of proximity. The curvature of the etched surfaces must also be considered in this investigation because it exposes different gradients of facet combinations at different distances from the emitter. These structures are also chosen to mitigate the probability that the alignment of the fabricated structures is less than optimal relative to the on-chip coordinate system.

The ideal outcome of this investigation will be a data set that can be used to build a model that enables the prediction of how various structures affect the optical coherence of emitters. This will enable the implementation of more simulation-based iterations of our cavity-emitter structures before proceeding to the laborious effort of fabrication.

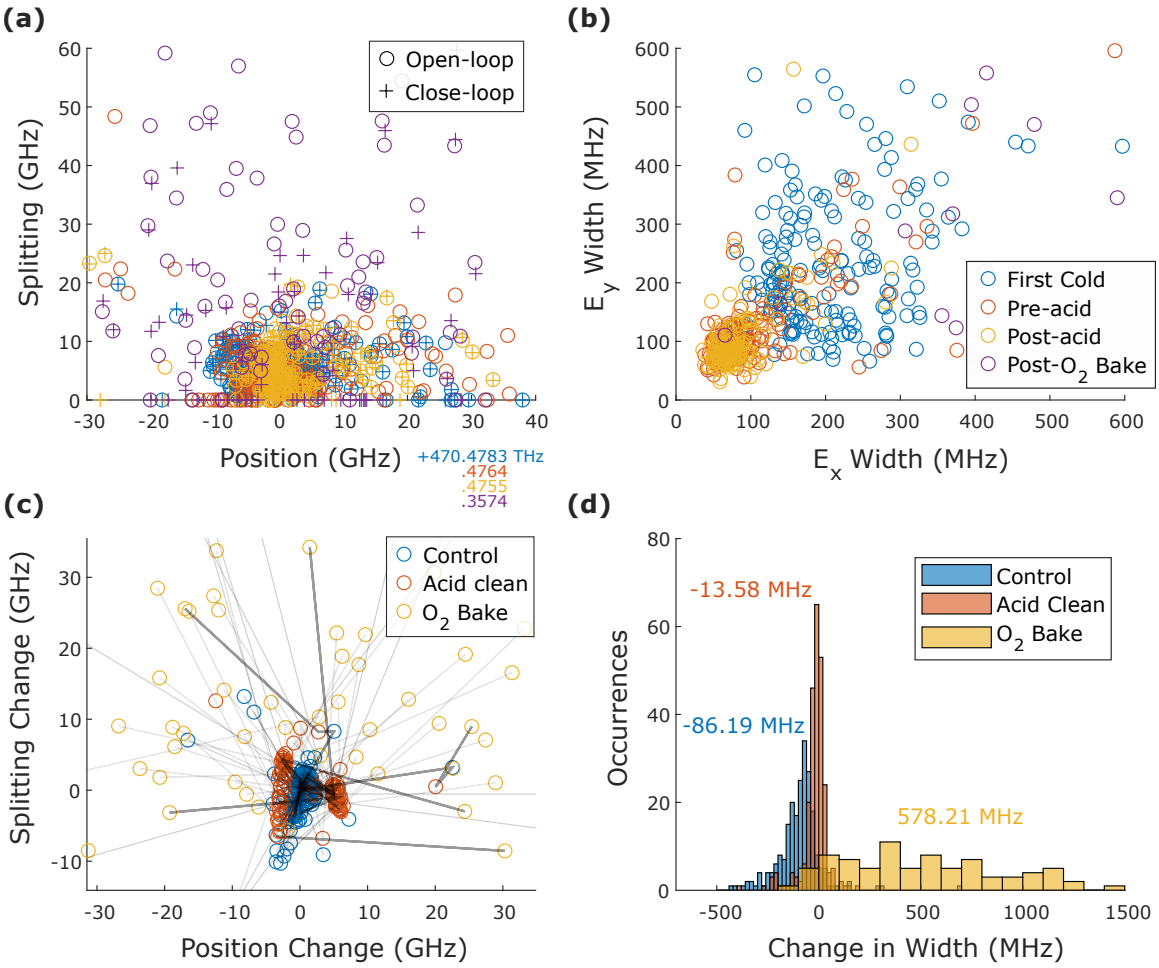

Figure 6-4: **Registered Tracking of NV Parameters.** **(a)** and **(b)** show summaries of the raw data. **(a)** Raw data showing the relationship between the NV's ZPL center position and splitting. No obvious trends can be seen. Each data set has been calibrated for that particular run's median position as indicated by the corresponding color next to the x-axis label. The colors match the key in **b**. **(b)** Raw data showing the widths of the E_x and E_y transitions. In principle, one would expect about a 1:1 to relationship between these parameters, which is present, but has a larger distribution than expected. **(c)** and **(d)** show an analysis tracking the changes between NVs directly. It is important to note that the statistics show individual deltas rather than a single result of the difference between two uncorrelated populations. The data points are labeled by the step that occurred between the runs. **(c)** Each line follows a single NV's evolution through the runs, specifically showing the difference with respect to the "First Cold" run. A few lines are highlighted to feature a couple of the trajectories. **(d)** A histogram showing the cumulative shifts between combinations of runs. The large shift with respect to the control data set is due to power broadening that was not experimentally corrected for in the "First Cold" run. More interestingly, the average linewidth of emitters narrowed by 13.6 MHz after the samples underwent the acid clean step and increased by 0.58 GHz after the O_2 bake.

The goal is to perform this test using three different etching techniques:

- Our own etching process which is performed under biased oxygen plasma [101].
- Igor Aharonovich's electron beam induced etching process (EBIE) [26]. This technique provides a larger chemical component of the directed etch that may reduce lattice damage.
- Marko Lončar's angled etching technique uses a higher biased oxygen ion beam so the sample can be located further from the plasma [7].

The undercutting step of the etch will not be a component of this investigation because the structures are not compatible with the undercut, although it would be an appropriate extension of this work.

Taken from initial measurements of one sample, I found an NV density of 0.29 NVs/μm^2. If this is converted to a linear density around the circumference of different radii rings (illustrated in Figure 6-5), the number of times it will be necessary to replicate the ring can be estimated. Based on these findings, achieving a density >10 NVs/μm (radial direction) would be ideal. Under these conditions, it should be possible to achieve this NV density for rings with radii >4 μm. To increase the odds of an NV centered in the <4 μm rings, alignment of the rings to pre-characterized emitters may be necessary.

Needless to say, this type of experiment is subject to failure at many levels. In previous attempts to carry out similar experiments, large amounts of non-specific fluorescence on the surface of the diamond obscured the detection of any single photon emitter. Although baking the sample in oxygen, or annealing in vacuum at high temperature can positively resolve the problem, these approaches can introduce an additional step in the process that is unwanted. Under some circumstances, virtually all of the NV centers recognized originally in a sample have been shown to disappear following the etching process.

As an aside, the infrastructure described in Chapter 2 could provide a correlation that may answer why these NVs vanish based on various structured data (e.g.,

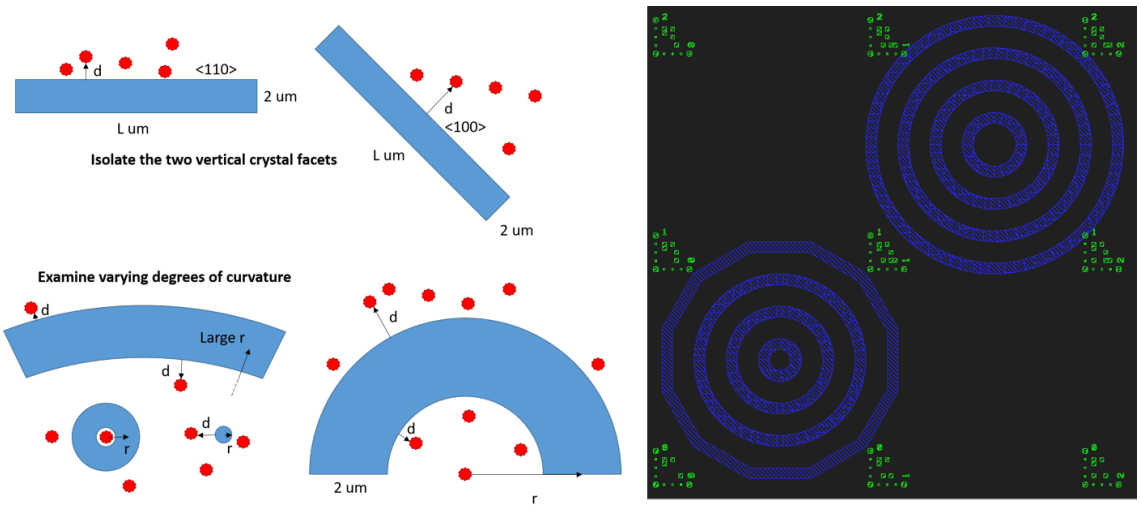

Figure 6-5: **Etch Test.** (Left) Top-down diagram showing the variety of surfaces (blue) to be etched in association with randomly located NV centers (red). The two flat surfaces shown at the top will permit the etching of a flat, vertical diamond face, while the bottom structures will permit the incorporation of varying degrees of curvature exposed to the NV centers. (Right) Realization of the schematic in a potential mask design. The outermost circle is composed of flat edges to test contributions of varying amounts to the NV's proximity to different diamond facets.

slight differences in settings of the tools used to variations in humidity in the lab). Unfortunately, insufficient access to data sets serves as a roadblock at this point in time.

The most significant assumption associated with this experiment is that the NV optical coherence will improve as a function of the distance from the etched surface. If the surface of the diamond that is protected by a mask undergoes deterioration, or becomes contaminated, discernible differences in optical coherence values anticipated as a function of distance from the etched surface may be concealed by excessively broad linewidths. While this problem may be positively resolved by cleaning and/or additional annealing steps, those solutions may introduce issues themselves. Regardless of those concerns, it is notable that we have observed that NVs in the bulk region of diamond with fabricated structures exhibit good optical coherence properties.

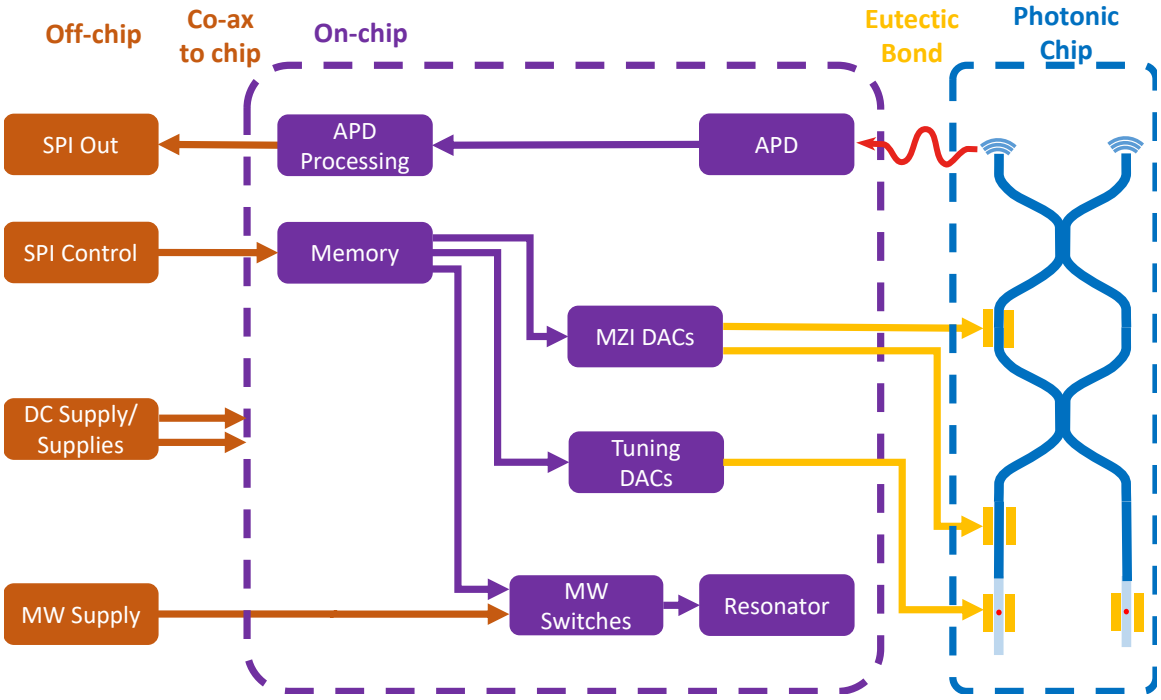

Figure 6-6: **Schematic Representation of a CMOS Chip Designed to Serialize I/O from Room Temperature to the Cryogenic Photonic Chip.** The SPI protocol is used here to load values into the cryogenic CMOS chip's memory. An on-chip clock will distribute values in memory to the appropriate DAC to update relevant voltages on the photonic chip.

6.2 The Device

As a team, we have made significant progress in the effort to build a quantum repeater device. The next step will be the development of the device itself. In 2013, our initial objective was to tackle the ambitious task of successfully demonstrating entanglement on a chip. This objective quickly morphed into the truly ambitious task of building an NV-based quantum repeater, a task clearly requiring a team effort. I devoted significant time and effort to the organization and management of the team that tackled this project.

The last piece of the puzzle is to consider what the architecture of a final functioning device might look like. Along with Isaac Harris (Quantum Photonics Lab) and Mohamed Ibrahim (Ruonan Han lab), as well as previous work led by Donggyu Kim and Chris Foy [79], we are refining the MW delivery system to achieve compatibility with CMOS technology which will enable hybrid integration with the optical

platform pioneered by Sara Mouradian [100]. This includes engineering the low-level I/O of the CMOS chip under relatively strict power budgets and electric interconnects at cryogenic temperatures, as well as performing initial tests to confirm that our CMOS models work as expected at cryogenic temperatures. To reduce heat loads at cryogenic temperatures, the number of physical I/O lines needs to be reduced by serializing communication. Figure 6-6 shows an initial design to serialize I/O using buffers and very basic on-chip processing, which at this point consists of primarily counting APD clicks.

While this is clearly an important aspect of our original engineering project, having led the team to this point in the project's evolution, my contribution to the effort will be largely advisory in nature and will focus primarily on the development of code necessary to perform automated measurements.

6.3 Outlook

The infrastructure discussed in this thesis enables larger data sets, improved institutional memory, and more accurate recordkeeping. In industry, this translates into better engineering practices and provides the framework for implementing process control. The ultimate development of large scale quantum computing systems and groundbreaking quantum technology will require the continued exploration of a wide variety of qubit register designs. Towards this end, the work presented in Chapter 3 of this thesis was just the beginning. While many unknowns and technological improvements are necessary, we have shown that it is possible to implant Si at targeted sites while retaining high optical coherence for quantum network applications. In conjunction with novel multi-qubit registers, as presented in Chapter 4, we provide a direction to implement heterogeneous nodes that utilize the long memory properties of NVs and high optical coherence properties of SiVs (similar to work associated with the trapped ion field [72, 108]). Furthermore, the capacity of coherent coupling associated with these registers provides a strategy to enable basic error-corrected nodes. All of this comes together in this Chapter. In the realm of controlling fabrication pro-

cesses related to engineering and scientific pursuits, I have introduced a technique and platform with utility in both academic and industrial settings. I have also shown how procedures developed as part of this research project are already yielding increasing returns, as described in Chapter 5 where problems associated with our implantation procedure are discovered and addressed. Although progress has been made in our efforts to develop a quantum repeater architecture, it is exciting to begin thinking about the next steps in the process, and where the next generation of students advances the field.

The body of work completed in studies associated with this thesis is encouraging both in terms of the development of quantum technologies and advancing our understanding of, and control over, quantum processing systems. The integration of machine learning, big data management, process control for designing and fabricating quantum technology, and more sophisticated analysis pipelines into a quantum engineering framework will enable more collaborative, robust, and statistically relevant protocols associated with efforts to scale quantum systems for use in a wide battery of technologies.

The outcomes of studies reported here paves the way to address a variety of new and exciting questions relating to the dynamics and origin of defect's optical transitions to the development of novel approaches associated with innovative diamond annealing strategies that will influence thinking about and engineering optical coherence. The tools outlined in Chapter 2 of this thesis have the potential to guide scientists and engineers to investigate a wide variety of new and exciting questions in the quantum computing realm.

Bibliography

[1] Y. Chu, private communication.

[2] Mohamed H. Abobeih, Julia Cramer, Michiel A. Bakker, Norbert Kalb, Matthew Markham, Daniel J. Twitchen, and Tim H. Taminiau. One-second coherence for a single electron spin coupled to a multi-qubit nuclear-spin environment. *Nat. Commun.*, 9(1):2552, 2018.

[3] Mohamed H. Abobeih, Julia Cramer, Michiel A. Bakker, Norbert Kalb, Daniel J. Twitchen, Matthew Markham, and Tim H. Taminiau. One-second coherence for a single electron spin coupled to a multi-qubit nuclear-spin environment. 2018.

[4] J. B. S. Abraham, B. A. Aguirre, J. L. Pacheco, G. Vizkelethy, and E. Bielejec. Fabrication and characterization of a co-planar detector in diamond for low energy single ion implantation. *Applied Physics Letters*, 109(6):063502, August 2016.

[5] Igor Aharonovich, Dirk Englund, and Milos Toth. Solid-state single-photon emitters. *Nat. Photonics*, 10(10):631–641, 2016.

[6] Igor Aharonovich and Elke Neu. Diamond Nanophotonics. *Advanced Optical Materials*, 2(10):911–928, 2014.

[7] Haig A. Atikian, Pawel Latawiec, Michael J. Burek, Young-Ik Sohn, Srujan Meesala, Normand Gravel, Ammar B. Kouki, and Marko Lončar. Freestanding nanostructures via reactive ion beam angled etching. *APL Photonics*, 2(5):051301, 2017.

[8] David D. Awschalom, Ronald Hanson, Jörg Wrachtrup, and Brian B. Zhou. Quantum technologies with optically interfaced solid-state spins. *Nat. Photonics*, 12(9):516–527, 2018.

[9] Koji Azuma, Kiyoshi Tamaki, and Hoi-Kwong Lo. All-photonic quantum repeaters. *Nature Communications*, 6:6787, April 2015.

[10] Dave Bacon. Operator quantum error-correcting subsystems for self-correcting quantum memories. *Phys. Rev. A*, 73:012340, Jan 2006.

[11] A. Badolato, K. Hennessy, M. Atatüre, J. Dreiser, E. Hu, P.M. Petroff, and A. Imamoglu. Deterministic Coupling of Single Quantum Dots to Single Nanocavity Modes. *Science*, 308(5725):1158 – 1161, 2005.

[12] N. Bar-Gill, L. M. Pham, A. Jarmola, D. Budker, and R. L. Walsworth. Solid-state electronic spin coherence time approaching one second. *Nat. Commun.*, 4:1743–1746, 2013.

[13] A. Batalov, C. Zierl, T. Gaebel, P. Neumann, I. Y. Chan, G. Balasubramanian, P. R. Hemmer, F. Jelezko, and J. Wrachtrup. Temporal coherence of photons emitted by single nitrogen-vacancy defect centers in diamond using optical rabi-oscillations. *Phys. Rev. Lett.*, 100(7):077401, 2008.

[14] I. Bayn, S. Mouradian, L. Li, J. A. Goldstein, T. Schröder, J. Zheng, E. H. Chen, O. Gaathon, M. Lu, A. Stein, C. A. Ruggiero, J. Salzman, R. Kalish, and Dirk Englund. Fabrication of triangular nanobeam waveguide networks in bulk diamond using single-crystal silicon hard masks. *Applied Physics Letters*, 105(21):211101, 2014.

[15] Igal Bayn, Edward H. Chen, Matthew E. Trusheim, Luozhou Li, Tim Schröder, Ophir Gaathon, Ming Lu, Aaron Stein, Mingzhao Liu, Kim Kisslinger, Hannah Clevenson, and Dirk Englund. Generation of Ensembles of Individually Resolvable Nitrogen Vacancies Using Nanometer-Scale Apertures in Ultrahigh-Aspect Ratio Planar Implantation Masks. *Nano Letters*, 15(3):1751–1758, March 2015.

[16] Igal Bayn, Boris Meyler, Joseph Salzman, and Rafi Kalish. Triangular nanobeam photonic cavities in single-crystal diamond. *New Journal of Physics*, 13(2):025018, feb 2011.

[17] S. Becker, N. Raatz, St Jankuhn, R. John, and J. Meijer. Nitrogen implantation with a scanning electron microscope. *Scientific reports*, 8(1):32–32, Jan 2018. 29311583[pmid].

[18] Luiz F. F. Belussi and Nina S. T. Hirata. Fast component-based qr code detection in arbitrarily acquired images. *Journal of Mathematical Imaging and Vision*, 45(3):277–292, Mar 2013.

[19] S.c. Benjamin, B.w. Lovett, and J.m. Smith. Prospects for measurement-based quantum computing with solid state spins. *Laser & Photonics Reviews*, 3(6):556–574, November 2009.

[20] H Bernien, B Hensen, W Pfaff, G Koolstra, M S Blok, L Robledo, T H Taminiau, M Markham, D J Twitchen, L Childress, and R Hanson. Heralded entanglement between solid-state qubits separated by three metres. *Nature*, 497(7447):86–90, may 2013.

[21] Hannes Bernien, Lilian Childress, Lucio Robledo, Matthew Markham, Daniel Twitchen, and Ronald Hanson. Two-photon quantum interference from separate nitrogen vacancy centers in diamond. *Phys. Rev. Lett.*, 108:043604, Jan 2012.

[22] Hannes Bernien, Lilian Childress, Lucio Robledo, Matthew Markham, Daniel Twitchen, and Ronald Hanson. Two-photon quantum interference from separate nitrogen vacancy centers in diamond. *Phys. Rev. Lett.*, 108(4):043604, 2012.

[23] Eric Bersin, Michael Walsh, Sara L. Mouradian, Matthew E. Trusheim, Tim Schröder, and Dirk Englund. Individual control and readout of qubits in a sub-diffraction volume. *npj Quantum Information*, 5(1):38, May 2019.

[24] S. Birchfield and C. Tomasi. A pixel dissimilarity measure that is insensitive to image sampling. *IEEE Transactions on Pattern Analysis and Machine Intelligence*, 20(4):401–406, 1998.

[25] Simone Birindelli, Marco Felici, Johannes S. Wildmann, Antonio Polimeni, Mario Capizzi, Annamaria Gerardino, Silvia Rubini, Faustino Martelli, Armando Rastelli, and Rinaldo Trotta. Single Photons on Demand from Novel Site-Controlled GaAsN/GaAsN:H Quantum Dots. *Nano Letters*, 14(3):1275–1280, March 2014.

[26] James Bishop, Marco Fronzi, Christopher Elbadawi, Vikram Nikam, Joshua Pritchard, Johannes E. Fröch, Ngoc My Hanh Duong, Michael J. Ford, Igor Aharonovich, Charlene J. Lobo, and Milos Toth. Deterministic nanopatterning of diamond using electron beams. *ACS Nano*, 12(3):2873–2882, Mar 2018.

[27] M. S. Blok, C. Bonato, M. L. Markham, D. J. Twitchen, V. V. Dobrovitski, and R. Hanson. Manipulating a qubit through the backaction of sequential partial measurements and real-time?feedback. *Nature Physics*, 10(3):189–193, 2014.

[28] Stefan Bogdanović, Madelaine S. Z. Liddy, Suzanne B. van Dam, Lisanne C. Coenen, Thomas Fink, Marko Lončar, and Ronald Hanson. Robust nanofabrication of an integrated platform for spin control in a tunable microcavity. *APL Photonics*, 2(12):126101, 2017.

[29] Bryan T. Gard, Keith R. Motes, Jonathan P. Olson, Peter P. Rohde, and Jonathan P. Dowling. An Introduction to Boson-Sampling. In *From Atomic to Mesoscale*, pages 167–192. WORLD SCIENTIFIC, March 2015.

[30] Michael J. Burek, Yiwen Chu, Madelaine S. Z. Liddy, Parth Patel, Jake Rochman, Srujan Meesala, Wooyoung Hong, Qimin Quan, Mikhail D. Lukin, and Marko Loncar. High quality-factor optical nanocavities in bulk single-crystal diamond. *Nature Communications*, 5(1):5718, 2014.

[31] Edward H. Chen, Ophir Gaathon, Matthew E. Trusheim, and Dirk Englund. Wide-field multispectral super-resolution imaging using spin-dependent fluorescence in nanodiamonds. *Nano Letters*, 13(5):2073–2077, 2013.

[32] Y-C Chen, Benjamin Griffiths, Laiyi Weng, Shannon Nicley, Shazeaa N Ishmael, Y N D Lekhai, Sam Johnson, Colin J Stephen, Ben L Green, Gavin W Morley, Mark E Newton, Martin J Booth, Patrick S Salter, and Jason M Smith.

Laser writing of individual atomic defects in a crystal with near-unity yield. *arXiv:1807.04028*, 2018.

[33] Yu Chen Chen, Patrick S. Salter, Sebastian Knauer, Laiyi Weng, Angelo C. Frangeskou, Colin J. Stephen, Shazeaa N. Ishmael, Philip R. Dolan, Sam Johnson, Ben L. Green, Gavin W. Morley, Mark E. Newton, John G. Rarity, Martin J. Booth, and Jason M. Smith. Laser writing of coherent colour centres in diamond. *Nat. Photonics*, 11(2):77–80, 2017.

[34] Soonwon Choi, Joonhee Choi, Renate Landig, Georg Kucsko, Hengyun Zhou, Junichi Isoya, Fedor Jelezko, Shinobu Onoda, Hitoshi Sumiya, Vedika Khemani, Curt von Keyserlingk, Norman Y. Yao, Eugene Demler, and Mikhail D. Lukin. Observation of discrete time-crystalline order in a disordered dipolar many-body system. *Nature*, 543:221, 03 2017.

[35] Y Chu, N P de Leon, B J Shields, B Hausmann, R Evans, E Togan, M J Burek, M Markham, A Stacey, A S Zibrov, A Yacoby, D J Twitchen, M Lončar, H Park, P Maletinsky, and M D Lukin. Coherent optical transitions in implanted nitrogen vacancy centers. *Nano Lett.*, 14(4):1982–6, apr 2014.

[36] Y. Chu, N.P. de Leon, B.J. Shields, B. Hausmann, R. Evans, E. Togan, M. J. Burek, M. Markham, A. Stacey, A.S. Zibrov, A. Yacoby, D.J. Twitchen, M. Lončar, H. Park, P. Maletinsky, and M.D. Lukin. Coherent Optical Transitions in Implanted Nitrogen Vacancy Centers. *Nano Letters*, 14(4):1982–1986, April 2014.

[37] Tatsuya c/o Content Idea of Asia Co. Ltd. ONODA and Kazuhiro c/o Content Idea of Asia Co. Ltd. MIWA. Two-dimensional code, May 2011.

[38] Alan T. Collins, Lars Allers, Christopher J. H. Wort, and Geoffrey A. Scarsbrook. The annealing of radiation damage in De Beers colourless CVD diamond. *Diamond and Related Materials*, 3(4):932–935, April 1994.

[39] Intel Corporation, Willow Garage, and Itseez. OpenCV QR Code Detector (https://docs.opencv.org/3.4/de/dc3/classcv_1_1QRCodeDetector.html).

[40] J. Cramer, N. Kalb, M. A. Rol, B. Hensen, M. S. Blok, M. Markham, D. J. Twitchen, R. Hanson, and T. H. Taminiau. Repeated quantum error correction on a continuously encoded qubit by real-time feedback. *Nature Communications*, 7:11526, 05 2016.

[41] J. Cramer, N. Kalb, M. A. Rol, B. Hensen, M. S. Blok, M. Markham, D. J. Twitchen, R. Hanson, and T. H. Taminiau. Repeated quantum error correction on a continuously encoded qubit by real-time feedback. *Nature Communications*, 7(1):11526, 2016.

[42] Gordon Davies, Simon C. Lawson, Alan T. Collins, Alison Mainwood, and Sarah J. Sharp. Vacancy-related centers in diamond. *Physical Review B*, 46(20):13157–13170, November 1992.

[43] Gordon Davies, Simon C. Lawson, Alan T. Collins, Alison Mainwood, and Sarah J. Sharp. Vacancy-related centers in diamond. *Phys. Rev. B*, 46(20):13157–13170, 1992.

[44] Felipe Fávaro De Oliveira, Denis Antonov, Ya Wang, Philipp Neumann, Seyed Ali Momenzadeh, Timo Häußermann, Alberto Pasquarelli, Andrej Denisenko, and Jörg Wrachtrup. Tailoring spin defects in diamond by lattice charging. *Nat. Commun.*, 8(May):15409, 2017.

[45] Peter Deák, Bálint Aradi, Moloud Kaviani, Thomas Frauenheim, and Adam Gali. Formation of NV centers in diamond: A theoretical study based on calculated transitions and migration of nitrogen and vacancy related defects. *Phys. Rev. B*, 89(7):075203, 2014.

[46] C. L. Degen, F. Reinhard, and P. Cappellaro. Quantum sensing. *Rev. Mod. Phys.*, 89:035002, Jul 2017.

[47] U. F. S. D'Haenens-Johansson, A. M. Edmonds, B. L. Green, M. E. Newton, G. Davies, P. M. Martineau, R. U. A. Khan, and D. J. Twitchen. Optical properties of the neutral silicon split-vacancy center in diamond. *Physical Review B*, 84(24):245208, December 2011.

[48] A. M. Dibos, M. Raha, C. M. Phenicie, and J. D. Thompson. Atomic source of single photons in the telecom band. *Phys. Rev. Lett.*, 120:243601, Jun 2018.

[49] Andreas Dietrich, Kay D. Jahnke, Jan M. Binder, Tokuyuki Teraji, Junichi Isoya, Lachlan J. Rogers, and Fedor Jelezko. Isotopically varying spectral features of silicon-vacancy in diamond. *New J. Phys.*, 16:113019, 2014.

[50] M W Doherty, N B Manson, P Delaney, and L C L Hollenberg. The negatively charged nitrogen-vacancy centre in diamond: the electronic solution. *New Journal of Physics*, 13(2):025019, 2011.

[51] Marcus W. Doherty, Neil B. Manson, Paul Delaney, Fedor Jelezko, Jörg Wrachtrup, and Lloyd C.L. Hollenberg. The nitrogen-vacancy colour centre in diamond. *Phys. Rep.*, 528(1):1–45, jul 2013.

[52] Marcus W. Doherty, Neil B. Manson, Paul Delaney, Fedor Jelezko, Jörg Wrachtrup, and Lloyd C.L. Hollenberg. The nitrogen-vacancy colour centre in diamond. *Physics Reports*, 528(1):1 – 45, 2013.

[53] F. Dolde, I. Jakobi, B. Naydenov, N. Zhao, S. Pezzagna, C. Trautmann, J. Meijer, P. Neumann, F. Jelezko, and J. Wrachtrup. Room-temperature entanglement between single defect spins in diamond. *Nature Physics*, 9:139, 02 2013.

[54] F. Dolde, I. Jakobi, B. Naydenov, N. Zhao, S. Pezzagna, C. Trautmann, J. Meijer, P. Neumann, F. Jelezko, and J. Wrachtrup. Room-temperature entanglement between single defect spins in diamond. *Nat. Phys.*, 9(3):139–143, feb 2013.

[55] E. A. Ekimov, S. G. Lyapin, K. N. Boldyrev, M. V. Kondrin, R. Khmelnitskiy, V. A. Gavva, T. V. Kotereva, and M. N. Popova. Germanium–vacancy color center in isotopically enriched diamonds synthesized at high pressures. *JETP Lett.*, 102(11):701–706, 2015.

[56] Ruffin E. Evans, Alp Sipahigil, Denis D. Sukachev, Alexander S. Zibrov, and Mikhail D. Lukin. Narrow-Linewidth Homogeneous Optical Emitters in Diamond Nanostructures via Silicon Ion Implantation. *Physical Review Applied*, 5(4):044010, April 2016.

[57] Andrei Faraon, Paul E. Barclay, Charles Santori, Kai-Mei C. Fu, and Raymond G. Beausoleil. Resonant enhancement of the zero-phonon emission from a colour centre in a diamond cavity. *Nat. Photonics*, 5:301–305, 2011.

[58] Andrei Faraon, Charles Santori, Zhihong Huang, Victor M. Acosta, and Raymond G. Beausoleil. Coupling of nitrogen-vacancy centers to photonic crystal cavities in monocrystalline diamond. *Phys. Rev. Lett.*, 109(3):033604, 2012.

[59] Django Software Foundation. Django Python Framework (https://www.djangoproject.com/).

[60] K.-M. C. Fu, C. Santori, P. E. Barclay, and R. G. Beausoleil. Conversion of neutral nitrogen-vacancy centers to negatively charged nitrogen-vacancy centers through selective oxidation. *Appl. Phys. Lett.*, 96(12):121907, mar 2010.

[61] Kai-Mei C. Fu, Charles Santori, Paul E. Barclay, Lachlan J. Rogers, Neil B. Manson, and Raymond G. Beausoleil. Observation of the Dynamic Jahn-Teller Effect in the Excited States of Nitrogen-Vacancy Centers in Diamond. *Phys. Rev. Lett.*, 103(25):256404, dec 2009.

[62] Torsten Gaebel, Michael Domhan, Iulian Popa, Christoffer Wittmann, Philipp Neumann, Fedor Jelezko, James R. Rabeau, Nikolas Stavrias, Andrew D. Greentree, Steven Prawer, Jan Meijer, Jason Twamley, Philip R. Hemmer, and Jörg Wrachtrup. Room-temperature coherent coupling of single spins in diamond. *Nat. Phys.*, 2(6):408–413, 2006.

[63] W. B. Gao, A. Imamoglu, H. Bernien, and R. Hanson. Coherent manipulation, measurement and entanglement of individual solid-state spins using optical fields. *Nature Photonics*, 9:363, 05 2015.

[64] M. L. Goldman, M. W. Doherty, A. Sipahigil, N. Y. Yao, S. D. Bennett, N. B. Manson, A. Kubanek, and M. D. Lukin. State-selective intersystem crossing in nitrogen-vacancy centers. *Phys. Rev. B*, 91:165201, Apr 2015.

[65] Richard I. Hartley. Theory and practice of projective rectification. *International Journal of Computer Vision*, 35(2):115–127, 1999.

[66] B. J M Hausmann, B. J. Shields, Q. Quan, Y. Chu, N. P. De Leon, R. Evans, M. J. Burek, A. S. Zibrov, M. Markham, D. J. Twitchen, H. Park, M. D. Lukin, and M. Lončar. Coupling of NV centers to photonic crystal nanobeams in diamond. *Nano Lett.*, 13(12):5791–5796, 2013.

[67] B. Hensen, H. Bernien, A. E. Dréau, A. Reiserer, N. Kalb, M. S. Blok, J. Ruitenberg, R. F. L. Vermeulen, R. N. Schouten, C. Abellán, W. Amaya, V. Pruneri, M. W. Mitchell, M. Markham, D. J. Twitchen, D. Elkouss, S. Wehner, T. H. Taminiau, and R. Hanson. Loophole-free bell inequality violation using electron spins separated by 1.3 kilometres. *Nature*, 526:682, 10 2015.

[68] B. Hensen, H. Bernien, A. E. Dréau, A. Reiserer, N. Kalb, M. S. Blok, J. Ruitenberg, R. F. L. Vermeulen, R. N. Schouten, C. Abellán, W. Amaya, V. Pruneri, M. W. Mitchell, M. Markham, D. J. Twitchen, D. Elkouss, S. Wehner, T. H. Taminiau, and R. Hanson. Loophole-free bell inequality violation using electron spins separated by 1.3 kilometres. *Nature*, 526:682, Oct 2015.

[69] Christian Hepp, Tina Müller, Victor Waselowski, Jonas N. Becker, Benjamin Pingault, Hadwig Sternschulte, Doris Steinmüller-Nethl, Adam Gali, Jeronimo R. Maze, Mete Atatüre, and Christoph Becher. Electronic Structure of the Silicon Vacancy Color Center in Diamond. *Physical Review Letters*, 112(3):036405, January 2014.

[70] H. Hirschmuller. Stereo processing by semiglobal matching and mutual information. *IEEE Transactions on Pattern Analysis and Machine Intelligence*, 30(2):328–341, 2008.

[71] Peter C. Humphreys, Norbert Kalb, Jaco P. J. Morits, Raymond N. Schouten, Raymond F. L. Vermeulen, Daniel J. Twitchen, Matthew Markham, and Ronald Hanson. Deterministic delivery of remote entanglement on a quantum network. *Nature*, 558(7709):268–273, 2018.

[72] I. V. Inlek, C. Crocker, M. Lichtman, K. Sosnova, and C. Monroe. Multispecies trapped-ion node for quantum networking. *Phys. Rev. Lett.*, 118:250502, Jun 2017.

[73] Takayuki Iwasaki, Fumitaka Ishibashi, Yoshiyuki Miyamoto, Yuki Doi, Satoshi Kobayashi, Takehide Miyazaki, Kosuke Tahara, Kay D. Jahnke, Lachlan J. Rogers, Boris Naydenov, Fedor Jelezko, Satoshi Yamasaki, Shinji Nagamachi, Toshiro Inubushi, Norikazu Mizuochi, and Mutsuko Hatano. Germanium-Vacancy Single Color Centers in Diamond. *Scientific Reports*, 5:12882, August 2015.

[74] Kay D. Jahnke, Alp Sipahigil, Jan M. Binder, Marcus W. Doherty, Mathias Metsch, Lachlan J. Rogers, Neil B. Manson, Mikhail D. Lukin, and Fedor Jelezko. Electron–phonon processes of the silicon-vacancy centre in diamond. *New Journal of Physics*, 17(4):043011, 2015.

[75] I Jakobi, S A Momenzadeh, F Fávaro de Oliveira, J Michl, F Ziem, M Schreck, P Neumann, A Denisenko, and J Wrachtrup. Efficient creation of dipolar coupled nitrogen-vacancy spin qubits in diamond. *Journal of Physics: Conference Series*, 752(1):012001, 2016.

[76] A. Jarmola, A. Berzins, J. Smits, K. Smits, J. Prikulis, F. Gahbauer, R. Ferber, D. Erts, M. Auzinsh, and D. Budker. Longitudinal spin-relaxation in nitrogen-vacancy centers in electron irradiated diamond. *Applied Physics Letters*, December 2015.

[77] Jean-Christophe Jaskula, Erik Bauch, Silvia Arroyo-Camejo, Mikhail D. Lukin, Stefan W. Hell, Alexei S. Trifonov, and Ronald L. Walsworth. Superresolution optical magnetic imaging and spectroscopy using individual electronic spins in diamond. *Opt. Express*, 25(10):11048–11064, May 2017.

[78] Norbert Kalb, Andreas A. Reiserer, Peter C. Humphreys, Jacob J. W. Bakermans, Sten J. Kamerling, Naomi H. Nickerson, Simon C. Benjamin, Daniel J. Twitchen, Matthew Markham, and Ronald Hanson. Entanglement Distillation between Solid-State Quantum Network Nodes. *Science*, 356(June):928–932, 2017.

[79] Donggyu Kim, Mohamed I. Ibrahim, Christopher Foy, Matthew E. Trusheim, Ruonan Han, and Dirk R. Englund. A cmos-integrated quantum sensor based on nitrogen-vacancy centres. *Nature Electronics*, 2(7):284–289, 2019.

[80] J. Koike, D. M. Parkin, and T. E. Mitchell. Displacement threshold energy for type IIa diamond. *Applied Physics Letters*, 60(12):1450–1452, March 1992.

[81] Pieter Kok, W. J. Munro, Kae Nemoto, T. C. Ralph, Jonathan P. Dowling, and G. J. Milburn. Linear optical quantum computing with photonic qubits. *Reviews of Modern Physics*, 79(1):135–174, January 2007.

[82] Ryan LaRose. Overview and comparison of gate level quantum software platforms. *Quantum*, 3:130, Mar 2019.

[83] M. A. Lea-Wilson, Jenifer N. Lomer, and J. A. Van Wyk. Electron spin resonance of the R4/W6 defect in irradiated diamond. *Philos. Mag. B*, 72(1):81–89, 1995.

[84] Jonathan C. Lee, David O. Bracher, Shanying Cui, Kenichi Ohno, Claire A. McLellan, Xingyu Zhang, Paolo Andrich, Benjamin Alemán, Kasey J. Russell, Andrew P. Magyar, Igor Aharonovich, Ania Bleszynski Jayich, David Awschalom, and Evelyn L. Hu. Deterministic coupling of delta-doped nitrogen vacancy centers to a nanobeam photonic crystal cavity. *Appl. Phys. Lett.*, 105(26):261101, 2014.

[85] Margarita Lesik, Piernicola Spinicelli, Sébastien Pezzagna, Patrick Happel, Vincent Jacques, Olivier Salord, Bernard Rasser, Anne Delobbe, Pierre Sudraud,

Alexandre Tallaire, Jan Meijer, and Jean-François Roch. Maskless and targeted creation of arrays of colour centres in diamond using focused ion beam technology. *physica status solidi (a)*, 210(10):2055–2059, October 2013.

[86] L. Li, T. Schröder, E. H. Chen, M. Walsh, I. Bayn, J. Goldstein, O. Gaathon, M. E. Trusheim, M. Lu, J. Mower, M. Cotlet, M. L. Markham, D. J. Twitchen, and D. Englund. Coherent spin control of a nanocavity-enhanced qubit in diamond. *Nat. Comm.*, 6:6173, 2015.

[87] Luozhou Li, Igal Bayn, Ming Lu, Chang-Yong Nam, Tim Schröder, Aaron Stein, Nicholas C. Harris, and Dirk Englund. Nanofabrication on unconventional substrates using transferred hard masks. *Scientific Reports*, 5:7802, January 2015.

[88] Luozhou Li, Tim Schröder, Edward H. Chen, Michael Walsh, Igal Bayn, Jordan Goldstein, Ophir Gaathon, Matthew E. Trusheim, Ming Lu, Jacob Mower, Mircea Cotlet, Matthew L. Markham, Daniel J. Twitchen, and Dirk Englund. Coherent spin control of a nanocavity-enhanced qubit in diamond. *Nature Communications*, 6:6173, January 2015.

[89] Ying Li, Peter C. Humphreys, Gabriel J. Mendoza, and Simon C. Benjamin. Resource Costs for Fault-Tolerant Linear Optical Quantum Computing. *Physical Review X*, 5(4):041007, October 2015.

[90] Benjamin Lienhard, Tim Schröder, Sara Mouradian, Florian Dolde, Toan Trong Tran, Igor Aharonovich, and Dirk Englund. Bright and photostable single-photon emitter in silicon carbide. *Optica*, 3(7):768, July 2016.

[91] Peter Lodahl. Quantum-dot based photonic quantum networks. *Quantum Sci. Technol.*, 3(1):13001, 2018.

[92] I Lovchinsky, A O Sushkov, E Urbach, N P De Leon, S Choi, K De Greve, R Evans, R Gertner, C Müller, L Mcguinness, F Jelezko, R L Walsworth, H Park, and M D Lukin. Nuclear magnetic resonance detection and spectroscopy of single proteins using quantum logic. *Science*, 351(6275):836–841, 2016.

[93] N B. Manson, J P. Harrison, and M J. Sellars. Nitrogen-vacancy center in diamond: Model of the electronic structure and associated dynamics. *Phys. Rev. B*, 74(10):104303, 2006.

[94] J. Martin, R. Wannemacher, J. Teichert, L. Bischoff, and B. Köhler. Generation and detection of fluorescent color centers in diamond with submicron resolution. *Applied Physics Letters*, 75(20):3096–3098, November 1999.

[95] J R Maze, A Gali, E Togan, Y Chu, A Trifonov, E Kaxiras, and M D Lukin. Properties of nitrogen-vacancy centers in diamond: the group theoretic approach. *New Journal of Physics*, 13(2):025025, 2011.

[96] David C. McKay, Thomas Alexander, Luciano Bello, Michael J. Biercuk, Lev Bishop, Jiayin Chen, Jerry M. Chow, Antonio D. Córcoles, Daniel Egger, Stefan Filipp, Juan Gomez, Michael Hush, Ali Javadi-Abhari, Diego Moreda, Paul Nation, Brent Paulovicks, Erick Winston, Christopher J. Wood, James Wootton, and Jay M. Gambetta. Qiskit backend specifications for openqasm and openpulse experiments, 2018.

[97] Srujan Meesala, Young-Ik Sohn, Benjamin Pingault, Linbo Shao, Haig A. Atikian, Jeffrey Holzgrafe, Mustafa Gündoğan, Camille Stavrakas, Alp Sipahigil, Cleaven Chia, Ruffin Evans, Michael J. Burek, Mian Zhang, Lue Wu, Jose L. Pacheco, John Abraham, Edward Bielejec, Mikhail D. Lukin, Mete Atatüre, and Marko Lončar. Strain engineering of the silicon-vacancy center in diamond. *Phys. Rev. B*, 97:205444, May 2018.

[98] J. Meijer, B. Burchard, M. Domhan, C. Wittmann, T. Gaebel, I. Popa, F. Jelezko, and J. Wrachtrup. Generation of single color centers by focused nitrogen implantation. *Applied Physics Letters*, 87(26):261909, December 2005.

[99] M. Hamed Mohammady, Hyeongrak Choi, Matthew E. Trusheim, Abolfazl Bayat, Dirk Englund, and Yasser Omar. Low-control and robust quantum refrigerator and applications with electronic spins in diamond. *Phys. Rev. A*, 97:042124, Apr 2018.

[100] Sara Mouradian. *A Scalable Quantum Computation Platform: Solid State Quantum Memories Coupled to Photonic Integrated Circuits*. PhD thesis, Massachusetts Institute of Technology, 2018.

[101] Sara Mouradian, Noel H. Wan, Tim Schröder, and Dirk Englund. Rectangular photonic crystal nanobeam cavities in bulk diamond. *Applied Physics Letters*, 111(2):021103, 2017.

[102] Sara L Mouradian, Tim Schröder, Carl B Poitras, Luozhou Li, Jordan Goldstein, Edward H Chen, Michael Walsh, Jaime Cardenas, Matthew L Markham, Daniel J Twitchen, Michal Lipson, and Dirk Englund. Scalable integration of long-lived quantum memories into a photonic circuit. *Phys. Rev. X*, 5(3):1–5, 2015.

[103] Sara L. Mouradian, Tim Schröder, Carl B. Poitras, Luozhou Li, Jordan Goldstein, Edward H. Chen, Michael Walsh, Jaime Cardenas, Matthew L. Markham, Daniel J. Twitchen, Michal Lipson, and Dirk Englund. Scalable Integration of Long-Lived Quantum Memories into a Photonic Circuit. *Physical Review X*, 5(3):031009, July 2015.

[104] Tina Müller, Christian Hepp, Benjamin Pingault, Elke Neu, Stefan Gsell, Matthias Schreck, Hadwig Sternschulte, Doris Steinmüller-Nethl, Christoph Becher, and Mete Atatüre. Optical signatures of silicon-vacancy spins in diamond. *Nature Communications*, 5, February 2014.

[105] B. Naydenov, R. Kolesov, A. Batalov, J. Meijer, S. Pezzagna, D. Rogalla, F. Jelezko, and J. Wrachtrup. Engineering single photon emitters by ion implantation in diamond. *Applied Physics Letters*, 95(18):181109–181109–3, November 2009.

[106] Boris Naydenov, Friedemann Reinhard, Anke Lämmle, V. Richter, Rafi Kalish, Ulrika F. S. D'Haenens-Johansson, Mark Newton, Fedor Jelezko, and Jo?rg Wrachtrup. Increasing the coherence time of single electron spins in diamond by high temperature annealing. *Appl. Phys. Lett.*, 97(24):242511, 2010.

[107] Boris Naydenov, V. Richter, Johannes Beck, Matthias Steiner, Philipp Neumann, Gopalakrishnan Balasubramanian, Jocelyn Achard, Fedor Jelezko, Jo?rg Wrachtrup, and Rafi Kalish. Enhanced generation of single optically active spins in diamond by ion implantation. *Appl. Phys. Lett.*, 96(16):163108, 2010.

[108] V. Negnevitsky, M. Marinelli, K. K. Mehta, H.-Y. Lo, C. Flühmann, and J. P. Home. Repeated multi-qubit readout and feedback with a mixed-species trapped-ion register. *Nature*, 563(7732):527–531, Nov 2018.

[109] Kae Nemoto, Michael Trupke, Simon J. Devitt, Ashley M. Stephens, Burkhard Scharfenberger, Kathrin Buczak, Tobias Nöbauer, Mark S. Everitt, Jörg Schmiedmayer, and William J. Munro. Photonic Architecture for Scalable Quantum Information Processing in Diamond. *Physical Review X*, 4(3):031022, August 2014.

[110] E. Neu, F. Guldner, C. Arend, Y. Liang, S. Ghodbane, H. Sternschulte, D. Steinmüller-Nethl, A. Krueger, and C. Becher. Low temperature investigations and surface treatments of colloidal narrowband fluorescent nanodiamonds. *Journal of Applied Physics*, 113(20):203507, May 2013.

[111] Elke Neu, Mario Agio, and Christoph Becher. Photophysics of single silicon vacancy centers in diamond: implications for single photon emission. *Optics Express*, 20(18):19956, August 2012.

[112] Elke Neu, David Steinmetz, Janine Riedrich-Möller, Stefan Gsell, Martin Fischer, Matthias Schreck, and Christoph Becher. Single photon emission from silicon-vacancy colour centres in chemical vapour deposition nano-diamonds on iridium. *New Journal of Physics*, 13(2):025012, February 2011.

[113] Naomi H. Nickerson, Joseph F. Fitzsimons, and Simon C. Benjamin. Freely scalable quantum technologies using cells of 5-to-50 qubits with very lossy and noisy photonic links. *Phys. Rev. X*, 4:041041, Dec 2014.

[114] NumPy. NumpyDocs Documentation (https://numpydoc.readthedocs.io/).

[115] B. K. Ofori-Okai, S. Pezzagna, K. Chang, M. Loretz, R. Schirhagl, Y. Tao, B. A. Moores, K. Groot-Berning, J. Meijer, and C. L. Degen. Spin properties of very shallow nitrogen vacancy defects in diamond. *Phys. Rev. B*, 86(8):1–5, 2012.

[116] Kenichi Ohno, F Joseph Heremans, Charles F De Casas, Bryan A Myers, Benjamín J Alemán, C Ania, Bleszynski Jayich, and David D Awschalom. Three-dimensional localization of spins in diamond using 12 C implantation. *Appl. Phys. Lett.*, 105:052406, 2014.

[117] Kenichi Ohno, F Joseph Heremans, Lee C Bassett, Bryan A Myers, David M Toyli, Ania C Bleszynski Jayich, Christopher J Palmstrøm, and David D Awschalom. Engineering shallow spins in diamond with nitrogen delta-doping. *Appl. Phys. Lett.*, 101(8):82413, 2012.

[118] P. Olivero, S. Rubanov, P. Reichart, B. C. Gibson, S. T. Huntington, J. R. Rabeau, Andrew D. Greentree, J. Salzman, D. Moore, D. N. Jamieson, and S. Prawer. Characterization of three-dimensional microstructures in single-crystal diamond. *Diamond and Related Materials*, 15(10):1614–1621, 2006.

[119] J. O. Orwa, C. Santori, K. M C Fu, B. Gibson, D. Simpson, I. Aharonovich, A. Stacey, A. Cimmino, P. Balog, M. Markham, D. Twitchen, A. D. Greentree, R. G. Beausoleil, and S. Prawer. Engineering of nitrogen-vacancy color centers in high purity diamond by ion implantation and annealing. *J. Appl. Phys.*, 109(8):083530, 2011.

[120] Mihir Pant, Hyeongrak Choi, Saikat Guha, and Dirk Englund. Percolation based architecture for cluster state creation using photon-mediated entanglement between atomic memories, 2017.

[121] Mihir Pant, Hari Krovi, Dirk Englund, and Saikat Guha. Rate-distance trade-off and resource costs for all-optical quantum repeaters. *Physical Review A*, 95(1):012304, January 2017.

[122] S Pezzagna, B Naydenov, F Jelezko, J Wrachtrup, and J Meijer. Creation efficiency of nitrogen-vacancy centres in diamond. *New Journal of Physics*, 12(6):065017, jun 2010.

[123] Sébastien Pezzagna, Detlef Rogalla, Dominik Wildanger, Jan Meijer, and Alexander Zaitsev. Creation and nature of optical centres in diamond for single-photon emission-overview and critical remarks. *New J. Phys.*, 13:035024, 2011.

[124] Sébastien Pezzagna, Detlef Rogalla, Dominik Wildanger, Jan Meijer, and Alexander Zaitsev. Creation and nature of optical centres in diamond for single-photon emission—overview and critical remarks. *New Journal of Physics*, 13(3):035024, March 2011.

[125] Sébastien Pezzagna, Dominik Wildanger, Paul Mazarov, Andreas D. Wieck, Yanko Sarov, Ivo Rangelow, Boris Naydenov, Fedor Jelezko, Stefan W. Hell, and Jan Meijer. Nanoscale Engineering and Optical Addressing of Single Spins in Diamond. *Small*, 6(19):2117–2121, October 2010.

[126] Benjamin Pingault, Jonas N. Becker, Carsten H. H. Schulte, Carsten Arend, Christian Hepp, Tillmann Godde, Alexander I. Tartakovskii, Matthew Markham, Christoph Becher, and Mete Atatüre. All-Optical Formation of Coherent Dark States of Silicon-Vacancy Spins in Diamond. *Physical Review Letters*, 113(26):263601, December 2014.

[127] John Preskill. Quantum computing in the nisq era and beyond. 2018.

[128] David Press, Thaddeus D. Ladd, Bingyang Zhang, and Yoshihisa Yamamoto. Complete quantum control of a single quantum dot spin using ultrafast optical pulses. *Nature*, 456:218, 11 2008.

[129] J. R. Rabeau, P. Reichart, G. Tamanyan, D. N. Jamieson, S. Prawer, F. Jelezko, T. Gaebel, I. Popa, M. Domhan, and J. Wrachtrup. Implantation of labelled single nitrogen vacancy centers in diamond using N15. *Applied Physics Letters*, 88(2):023113, January 2006.

[130] J. R. Rabeau, P. Reichart, G. Tamanyan, D. N. Jamieson, S. Prawer, F. Jelezko, T. Gaebel, I. Popa, M. Domhan, and J. Wrachtrup. Implantation of labelled single nitrogen vacancy centers in diamond using15N. *Appl. Phys. Lett.*, 88(2):023113, 2006.

[131] Daniel Riedel, Immo Söllner, Brendan J. Shields, Sebastian Starosielec, Patrick Appel, Elke Neu, Patrick Maletinsky, and Richard J. Warburton. Deterministic enhancement of coherent photon generation from a nitrogen-vacancy center in ultrapure diamond. *Phys. Rev. X*, 7(3):031040, 2017.

[132] Janine Riedrich-Möller, Carsten Arend, Christoph Pauly, Frank Mücklich, Martin Fischer, Stefan Gsell, Matthias Schreck, and Christoph Becher. Deterministic coupling of a single silicon-vacancy color center to a photonic crystal cavity in diamond. *Nano Lett.*, 14(9):5281–5287, 2014.

[133] Janine Riedrich-Möller, Sébastien Pezzagna, Jan Meijer, Christoph Pauly, Frank Mücklich, Matthew Markham, Andrew M. Edmonds, and Christoph Becher. Nanoimplantation and Purcell enhancement of single nitrogen-vacancy centers in photonic crystal cavities in diamond. *Applied Physics Letters*, 106(22):221103, June 2015.

[134] Janine Riedrich-Möller, Sébastien Pezzagna, Jan Meijer, Christoph Pauly, Frank Mücklich, Matthew Markham, Andrew M. Edmonds, and Christoph Becher. Nanoimplantation and Purcell enhancement of single nitrogen-vacancy centers in photonic crystal cavities in diamond. *Appl. Phys. Lett.*, 106(22):221103, 2015.

[135] Lucio Robledo, Hannes Bernien, Ilse Van Weperen, and Ronald Hanson. Control and coherence of the optical transition of single nitrogen vacancy centers in diamond. *Phys. Rev. Lett.*, 105(17):177403, 2010.

[136] Lucio Robledo, Lilian Childress, Hannes Bernien, Bas Hensen, Paul F. A. Alkemade, and Ronald Hanson. High-fidelity projective read-out of a solid-state spin quantum register. *Nature*, 477:574, 09 2011.

[137] Lucio Robledo, Lilian Childress, Hannes Bernien, Bas Hensen, Paul F. A. Alkemade, and Ronald Hanson. High-fidelity projective read-out of a solid-state spin quantum register. *Nature*, 477(7366):574–578, 2011.

[138] L. J. Rogers, K. D. Jahnke, T. Teraji, L. Marseglia, C. Müller, B. Naydenov, H. Schauffert, C. Kranz, J. Isoya, L. P. McGuinness, and F. Jelezko. Multiple intrinsically identical single-photon emitters in the solid state. *Nature Communications*, 5:4739, August 2014.

[139] Lachlan J. Rogers, Kay D. Jahnke, Mathias H. Metsch, Alp Sipahigil, Jan M. Binder, Tokuyuki Teraji, Hitoshi Sumiya, Junichi Isoya, Mikhail D. Lukin, Philip Hemmer, and Fedor Jelezko. All-Optical Initialization, Readout, and Coherent Preparation of Single Silicon-Vacancy Spins in Diamond. *Physical Review Letters*, 113(26):263602, December 2014.

[140] E. L. Rosenfeld, L. M. Pham, M. D. Lukin, and R. L. Walsworth. Sensing coherent dynamics of electronic spin clusters in solids. *Phys. Rev. Lett.*, 120:243604, Jun 2018.

[141] Maximilian Ruf, Mark IJspeert, Suzanne van Dam, Nick de Jong, Hans van den Berg, Guus Evers, and Ronald Hanson. Optically coherent nitrogen-vacancy centers in micrometer-thin etched diamond membranes. *Nano letters*, 19(6):3987–3992, Jun 2019. 31136192[pmid].

[142] Sorawis Sangtawesin, Bo L. Dwyer, Srikanth Srinivasan, James J. Allred, Lila V. H. Rodgers, Kristiaan De Greve, Alastair Stacey, Nikolai Dontschuk, Kane M. O'Donnell, Di Hu, D. Andrew Evans, Cherno Jaye, Daniel A. Fischer, Matthew L. Markham, Daniel J. Twitchen, Hongkun Park, Mikhail D. Lukin, and Nathalie P. de Leon. Origins of diamond surface noise probed by correlating single-spin measurements with surface spectroscopy. *Phys. Rev. X*, 9:031052, Sep 2019.

[143] C Santori, P E Barclay, K-M C Fu, R G Beausoleil, S Spillane, and M Fisch. Nanophotonics for quantum optics using nitrogen-vacancy centers in diamond. *Nanotechnology*, 21(27):274008, 2010.

[144] Luca Sapienza, Marcelo Davanço, Antonio Badolato, and Kartik Srinivasan. Nanoscale optical positioning of single quantum dots for bright and pure single-photon emission. *Nature Communications*, 6:7833, July 2015.

[145] C. Schneider, T. Heindel, A. Huggenberger, T. A. Niederstrasser, S. Reitzenstein, A. Forchel, S. Höfling, and M. Kamp. Microcavity enhanced single photon emission from an electrically driven site-controlled quantum dot. *Applied Physics Letters*, 100(9):091108, February 2012.

[146] Tim Schröder, Edward Chen, Luozhou Li, Michael Walsh, Matthew E. Trusheim, Igal Bayn, and Dirk Englund. Targeted creation and Purcell enhancement of NV centers within photonic crystal cavities in single-crystal diamond. In *Conference on Lasers and Electro-Optics 2014*, OSA Technical Digest (online), page FW1B.6. OSA, June 2014.

[147] Tim Schröder, Sara Mouradian, Jiabao Zheng, Matthew E. Trusheim, Michael Walsh, Edward H. Chen, Luozhou Li, Igal Bayn, and Dirk Englund. Review Article: Quantum Nanophotonics in Diamond. *J. Opt. Soc. Am. B*, 33(4):65–83, 2016.

[148] Tim Schröder, Matthew E. Trusheim, Michael Walsh, Luozhou Li, Jiabao Zheng, Marco Schukraft, Alp Sipahigil, Ruffin E. Evans, Denis D. Sukachev, Christian T. Nguyen, Jose L. Pacheco, Ryan M. Camacho, Edward S. Bielejec, Mikhail D. Lukin, and Dirk Englund. Scalable focused ion beam creation of nearly lifetime-limited single quantum emitters in diamond nanostructures. *Nature Communications*, 8(1):15376, May 2017.

[149] M. Schukraft, J. Zheng, T. Schröder, S. L. Mouradian, M. Walsh, M. E. Trusheim, H. Bakhru, and D. R. Englund. Invited Article: Precision nanoimplantation of nitrogen vacancy centers into diamond photonic crystal cavities and waveguides. *APL Photonics*, 1(2):020801, May 2016.

[150] M. Schukraft, J. Zheng, T. Schröder, S. L. Mouradian, M. Walsh, M. E. Trusheim, H. Bakhru, and D. R. Englund. Invited article: Precision nanoimplantation of nitrogen vacancy centers into diamond photonic crystal cavities and waveguides. *APL Photonics*, 1(2):020801, 2016.

[151] J. Schwartz, P. Michaelides, C. D. Weis, and T. Schenkel. In situ optimization of co-implantation and substrate temperature conditions for nitrogen-vacancy center formation in single-crystal diamonds. *New Journal of Physics*, 13(3):035022, March 2011.

[152] Neil Sinclair, Erhan Saglamyurek, Hassan Mallahzadeh, Joshua A. Slater, Mathew George, Raimund Ricken, Morgan P. Hedges, Daniel Oblak, Christoph Simon, Wolfgang Sohler, and Wolfgang Tittel. Spectral multiplexing for scalable quantum photonics using an atomic frequency comb quantum memory and feed-forward control. *Phys. Rev. Lett.*, 113:053603, Jul 2014.

[153] A. Sipahigil, R. E. Evans, D. D. Sukachev, M. J. Burek, J. Borregaard, M. K. Bhaskar, C. T. Nguyen, J. L. Pacheco, H. A. Atikian, C. Meuwly, R. M. Camacho, F. Jelezko, E. Bielejec, H. Park, M. Lončar, and M. D. Lukin. An integrated diamond nanophotonics platform for quantum-optical networks. *Science*, 354(6314):847–850, November 2016.

[154] A. Sipahigil, K. D. Jahnke, L. J. Rogers, T. Teraji, J. Isoya, A. S. Zibrov, F. Jelezko, and M. D. Lukin. Indistinguishable Photons from Separated Silicon-

Vacancy Centers in Diamond. *Physical Review Letters*, 113(11):113602, September 2014.

[155] A. Sipahigil, K. D. Jahnke, L. J. Rogers, T. Teraji, J. Isoya, A. S. Zibrov, F. Jelezko, and M. D. Lukin. Indistinguishable photons from separated silicon-vacancy centers in diamond. *Phys. Rev. Lett.*, 113:113602, Sep 2014.

[156] Alp Sipahigil, Michael Lurie Goldman, Emre Togan, Yiwen Chu, Matthew Markham, Daniel J Twitchen, Alexander S Zibrov, Alexander Kubanek, and Mikhail D Lukin. Quantum Interference of Single Photons from Remote Nitrogen-Vacancy Centers in Diamond. *Phys. Rev. Lett.*, 108(14):143601, apr 2012.

[157] P. Siyushev, H. Pinto, M. Vörös, A. Gali, F. Jelezko, and J. Wrachtrup. Optically controlled switching of the charge state of a single nitrogen-vacancy center in diamond at cryogenic temperatures. *Phys. Rev. Lett.*, 110(16):167402, 2013.

[158] G. Speranza, S. Torrengo, A. Miotello, L. Minati, I. Bernagozzi, M. Ferrari, M. Dipalo, and E. Kohn. Xps and ups in situ study of oxygen thermal desorption from nanocrystalline diamond surface oxidized by different process. *Diamond and Related Materials*, 20(4):560 – 563, 2011.

[159] P. Spinicelli, A. Dréau, L. Rondin, F. Silva, J. Achard, S. Xavier, S. Bansropun, T. Debuisschert, S. Pezzagna, J Meijer, V. Jacques, and J.-F. Roch. Engineered arrays of nitrogen-vacancy color centers in diamond based on implantation of CN - molecules through nanoapertures. *New Journal of Physics*, 13(2):025014, 2011.

[160] P. L. Stanwix, L. M. Pham, J. R. Maze, D. Le Sage, T. K. Yeung, P. Cappellaro, P. R. Hemmer, A. Yacoby, M. D. Lukin, and R. L. Walsworth. Coherence of nitrogen-vacancy electronic spin ensembles in diamond. *Phys. Rev. B*, 82:201201, Nov 2010.

[161] A. M. Steane. Error correcting codes in quantum theory. *Phys. Rev. Lett.*, 77:793–797, Jul 1996.

[162] D. D. Sukachev, A. Sipahigil, C. T. Nguyen, M. K. Bhaskar, R. E. Evans, F. Jelezko, and M. D. Lukin. Silicon-vacancy spin qubit in diamond: A quantum memory exceeding 10 ms with single-shot state readout. *Phys. Rev. Lett.*, 119:223602, Nov 2017.

[163] Alessandro Surrente, Marco Felici, Pascal Gallo, Benjamin Dwir, Alok Rudra, Giorgio Biasiol, and Eli Kapon. Polarization properties and disorder effects in H3 photonic crystal cavities incorporating site-controlled, high-symmetry quantum dot arrays. *Applied Physics Letters*, 107(3):031106, July 2015.

[164] Ph Tamarat, T. Gaebel, J. R. Rabeau, M. Khan, A. D. Greentree, H. Wilson, L. C.L. Hollenberg, S. Prawer, P. Hemmer, F. Jelezko, and J. Wrachtrup. Stark

shift control of single optical centers in diamond. *Phys. Rev. Lett.*, 97(8):083002, 2006.

[165] Ph. Tamarat, N. B. Manson, J. P. Harrison, R. L. McMurtrie, A. Nizovtsev, C. Santori, R. G. Beausoleil, P. Neumann, T. Gaebel, F. Jelezko, P. Hemmer, and J. Wrachtrup. Spin-flip and spin-conserving optical transitions of the nitrogen-vacancy centre in diamond. *New J. Phys.*, 10:045004, 2008.

[166] Syuto Tamura, Godai Koike, Akira Komatsubara, Tokuyuki Teraji, Shinobu Onoda, Liam P. McGuinness, Lachlan Rogers, Boris Naydenov, E. Wu, Liu Yan, Fedor Jelezko, Takeshi Ohshima, Junichi Isoya, Takahiro Shinada, and Takashi Tanii. Array of bright silicon-vacancy centers in diamond fabricated by low-energy focused ion beam implantation. *Applied Physics Express*, 7(11):115201, November 2014.

[167] Tohru Tanaka, Paul Knott, Yuichiro Matsuzaki, Shane Dooley, Hiroshi Yamaguchi, William J. Munro, and Shiro Saito. Proposed robust entanglement-based magnetic field sensor beyond the standard quantum limit. *Phys. Rev. Lett.*, 115:170801, Oct 2015.

[168] Linus Torvalds. git GitHub (https://github.com/git/git).

[169] David M. Toyli, Christoph D. Weis, Gregory D. Fuchs, Thomas Schenkel, and David D. Awschalom. Chip-Scale Nanofabrication of Single Spins and Spin Arrays in Diamond. *Nano Letters*, 10(8):3168–3172, August 2010.

[170] David M Toyli, Christoph D Weis, Gregory D Fuchs, Thomas Schenkel, and David D Awschalom. Chip-scale nanofabrication of single spins and spin arrays in diamond. *Nano Lett.*, 10(8):3168–72, aug 2010.

[171] Matthew E Trusheim and Dirk Englund. Wide-field strain imaging with preferentially aligned nitrogen-vacancy centers in polycrystalline diamond. *New Journal of Physics*, 18(12):123023, 2016.

[172] S. B. van Dam, M. Walsh, M. J. Degen, E. Bersin, S. L. Mouradian, A. Galiullin, M. Ruf, M. IJspeert, T. H. Taminiau, R. Hanson, and D. R. Englund. Optical coherence of diamond nitrogen-vacancy centers formed by ion implantation and annealing. *Phys. Rev. B*, 99:161203, Apr 2019.

[173] S. B. van Dam, M. Walsh, M. J. Degen, E. Bersin, S. L. Mouradian, A. Galiullin, M. Ruf, M. IJspeert, T. H. Taminiau, R. Hanson, and D. R. Englund. Optical coherence of diamond nitrogen-vacancy centers formed by ion implantation and annealing. *Phys. Rev. B*, 99:161203, Apr 2019.

[174] Suzanne B van Dam, Peter C Humphreys, Filip Rozpędek, Stephanie Wehner, and Ronald Hanson. Multiplexed entanglement generation over quantum networks using multi-qubit nodes. *Quantum Science and Technology*, 2(3):034002, 2017.

[175] G. Waldherr, Y. Wang, S. Zaiser, M. Jamali, T. Schulte-Herbruggen, H. Abe, T. Ohshima, J. Isoya, J. F. Du, P. Neumann, and J. Wrachtrup. Quantum error correction in a solid-state hybrid spin register. *Nature*, 506(7487):204–207, 02 2014.

[176] G. Waldherr, Y. Wang, S. Zaiser, M. Jamali, T. Schulte-Herbrüggen, H. Abe, T. Ohshima, J. Isoya, J. F. Du, P. Neumann, and J. Wrachtrup. Quantum error correction in a solid-state hybrid spin register. *Nature*, 506:204 EP –, Feb 2014.

[177] Michael Walsh. Microwave and optical control of sub-diffraction spin qubits in diamond at cryogenic temperatures. Master's thesis, Massachusetts Institute of Technology, 2015.

[178] Michael P. Walsh. CommandCenter source code and documentation on GitHub (https://github.com/mwalsh161/CommandCenter).

[179] Michael P. Walsh. ModuleServer source code and documentation on GitHub (https://github.com/mwalsh161/ModuleServer).

[180] Michael P. Walsh, Hyeongrak Choi, and Dirk R. Englund. Combined microscope objective and microwave wire for optically detected magnetic resonance imaging, Dec 2019.

[181] Michael P. Walsh and Dirk R. Englund. Systems and methods for automated microscopy, Dec 2019.

[182] Noel H. Wan, Sara Mouradian, and Dirk Englund. Two-dimensional photonic crystal slab nanocavities on bulk single-crystal diamond. *Applied Physics Letters*, 112(14):141102, 2018.

[183] Noel H. Wan, Brendan J. Shields, Donggyu Kim, Sara Mouradian, Benjamin Lienhard, Michael Walsh, Hassaram Bakhru, Tim Schröder, and Dirk Englund. Efficient extraction of light from a nitrogen-vacancy center in a diamond parabolic reflector. *Nano Letters*, 18(5):2787–2793, May 2018.

[184] Chunlang Wang, Asli Ugur, Vladimir Chernyshev, Jan Meijer, and Harald Weinfurter. A Single Photon Source Based on SiV Centers in Diamond. In *Frontiers in Optics*, OSA Technical Digest (CD), page JWD106. Optical Society of America, October 2006.

[185] Stephanie Wehner, David Elkouss, and R Hanson. Quantum Internet: a vision for the road ahead. *Science*, 362(October):303, 2018.

[186] T Yamamoto, S Onoda, T Ohshima, T Teraji, K Watanabe, S Koizumi, T Umeda, L. P. McGuinness, C Müller, B Naydenov, F Dolde, H Fedder, J. Honert, M L Markham, D J Twitchen, J Wrachtrup, F Jelezko, and J Isoya. Isotopic identification of engineered nitrogen-vacancy spin qubits in ultrapure diamond. *Phys. Rev. B*, 90(8):081117, 2014.

[187] T. Yamamoto, T. Umeda, K. Watanabe, S. Onoda, M. L. Markham, D. J. Twitchen, B. Naydenov, L. P. McGuinness, T. Teraji, S. Koizumi, F. Dolde, H. Fedder, J. Honert, J. Wrachtrup, T. Ohshima, F. Jelezko, and J. Isoya. Extending spin coherence times of diamond qubits by high-temperature annealing. *Phys. Rev. B*, 88(7):075206, aug 2013.

[188] Takashi Yamamoto, Christoph Müller, Liam P. McGuinness, Tokuyuki Teraji, Boris Naydenov, Shinobu Onoda, Takeshi Ohshima, Jörg Wrachtrup, Fedor Jelezko, and Junichi Isoya. Strongly coupled diamond spin qubits by molecular nitrogen implantation. *Phys. Rev. B*, 88(20):201201, nov 2013.

[189] J. Zhang, P. W. Hess, A. Kyprianidis, P. Becker, A. Lee, J. Smith, G. Pagano, I. D. Potirniche, A. C. Potter, A. Vishwanath, N. Y. Yao, and C. Monroe. Observation of a discrete time crystal. *Nature*, 543:217, 03 2017.

[190] Z. Zhang. A flexible new technique for camera calibration. *IEEE Transactions on Pattern Analysis and Machine Intelligence*, 22(11):1330–1334, 2000.

[191] J F Ziegler, M Ziegler, and J Biersack. The Stopping and Range of Ions in Matter (SRIM-2013, http://www.srim.org/).